Very Old and Very Young Compact Objects — X-ray Studies of Galactic Globular Clusters and Recent Core-collapse Supernovae

by

David Aaron Pooley

Submitted to the Department of Physics
in partial fulfillment of the requirements for the degree of

Doctor of Philosophy in Physics

at the

MASSACHUSETTS INSTITUTE OF TECHNOLOGY

February 2003

Author ..... David A. Pooley .....
Department of Physics
December 18, 2002

Certified by ..... 12/20/02 .....
Walter H. G. Lewin
Professor
Thesis Supervisor

Accepted by ..... Thomas J. Greytak .....
Thomas J. Greytak
Chairman, Department Committee on Graduate Students

Very Old and Very Young Compact Objects — X-ray Studies of Galactic Globular Clusters and Recent Core-collapse Supernovae

by

David Aaron Pooley

Submitted to the Department of Physics
on December 18, 2002, in partial fulfillment of the
requirements for the degree of
Doctor of Philosophy in Physics

Abstract

This thesis comprises the results of two distinct areas of research, namely, X-ray studies of Galactic globular clusters and X-ray studies of recent core collapse supernovae.

My analyses of the *Chandra X-ray Observatory* observations of the globular clusters NGC 6752 and NGC 6440 revealed as many low-luminosity X-ray sources as was in the entire census of globular cluster sources with the previous best X-ray imaging instrument, *Röntgensatellit*. In the observation of NGC 6752, I detect 6 X-ray sources within the $10\farcs5$ core radius and 13 more within the $115''$ half-mass radius down to a limiting luminosity of $L_{\rm X} \approx 10^{30}$ ergs s^{-1} for cluster sources. Based on a reanalysis of archival data from the *Hubble Space Telescope* and the Australia Telescope Compact Array, I make 12 optical identifications and one radio identification. Based on X-ray and optical properties of the identifications, I find 10 likely cataclysmic variables (CVs), 1–3 likely RS CVn or BY Dra systems, and 1 or 2 possible background objects. Of the 7 sources for which no optical identifications were made, one was detected in the archival radio data, and another was found to be a millisecond pulsar. Of the remaining sources, I expect that $\sim$2–4 are background objects and that the rest are either CVs or millisecond pulsars whose radio emission has not been detected. These and other *Chandra* results on globular clusters indicate that the dozens of CVs per cluster expected by theoretical arguments are being found. The findings to date also suggest that the ratio of CVs to other types of X-ray sources is remarkably similar in clusters of very different structural parameters. In the observation of NGC 6440, I detect 24 sources to a limiting luminosity of $\sim 2 \times 10^{31}$ ergs s^{-1} (0.5–2.5 keV) inside the cluster's half-mass radius, all of which lie within $\sim$2 core radii of the cluster center. I also find excess emission in and around the core which could be due to unresolved point sources. Based upon X-ray luminosities and colors, I conclude that there are 4–5 likely quiescent low-mass X-ray binaries and that most of the other sources are cataclysmic variables. I compare these results to *Chandra* results from other globular clusters and find the X-ray luminosity functions differ among the clusters.

Observations of the Type II-P (plateau) Supernova (SN) 1999em and Type IIn (narrow emission line) SN 1998S have enabled estimation of the profile of the SN ejecta, the structure of the circumstellar medium (CSM) established by the pre-SN stellar wind, and the nature of the shock interaction. SN 1999em is the first Type II-P detected at both X-ray and radio wavelengths. It is the least radio luminous and one of the least X-ray luminous SNe ever detected (except for the unusual and very close SN 1987A). My analysis of the *Chandra* X-ray data indicate non-radiative interaction of SN ejecta with a power-law density profile ($\rho \propto r^{-n}$ with $n \sim 7$) for a pre-SN wind with a low mass-loss rate of $\sim 2 \times 10^{-6}$ $M_\odot$ yr^{-1} for a wind velocity of 10 km s^{-1}, in agreement with radio mass-loss rate estimates. The *Chandra* data show an unexpected, temporary rise in the 0.4–2.0 keV X-ray flux at ~100 days after explosion. My analysis of SN 1998S yielded the first X-ray spectrum of a supernova in which numerous heavy element emission features (Ne, Al, Si, S, Ar, Fe) were present. Spectral fits to the *Chandra* data show that these heavy elements are overabundant with respect to solar values. I compare the observed elemental abundances and abundance ratios to theoretical calculations and find that our data are consistent with a progenitor mass of approximately 15–20 $M_\odot$ if the heavy element ejecta are radially mixed out to a high velocity. If the X-ray emission is from the reverse shock wave region, the supernova density profile must be moderately flat at a velocity $\sim 10^4$ km s^{-1}, the shock front is non-radiative at the time of the observations, and the mass-loss rate is $1\text{–}2\times10^{-4}$ $M_\odot$ yr^{-1} for a pre-supernova wind velocity of 10 km s^{-1}. This result is also supported by modeling of the radio emission which implies that SN 1998S is surrounded by a clumpy or filamentary CSM established by a high mass-loss rate, $\sim 2 \times 10^{-4}$ $M_\odot$ yr^{-1}, from the pre-supernova star.

Thesis Supervisor: Walter H. G. Lewin
Title: Professor

Acknowledgments

I am indebted to a great many people for their support and friendship throughout my years at MIT, and the following is but a short list of thanks.

First, I would like to thank my advisor, Walter H. G. Lewin, for the many opportunities he has given me to work with exciting new data and to learn the entire scientific process, from proposal to publication. He has given me tremendous freedom not typical for graduate students. He has taught me the importance of a "killer instinct" in this field and has provided guidance and support in helping me to become an independent scientist. I look forward to continuing to work with him in the years to come. I also would like to thank Walter for giving me the opportunity and encouragement to be a recitation instructor for 8.01 in the fall of 1999 and again for 8.02 in the spring of 2002. Those experiences were epiphanies for me, as I realized how much I truly enjoyed teaching and was convinced that I wanted to continue to teach throughout my career. It was an added bonus to learn about teaching from a true maestro.

Within our research group at MIT, I owe special thanks to Jeffrey Kommers and Derek Fox, both of whom mentored me in my early years as a graduate student. Jon Miller has been a wonderful colleague and friend, and I can think of no one better to whom I could have lost a didgeridoo. I have enjoyed our many conversations about things scientific and not so scientific, and I hope that continued collaboration is in both of our futures. Let's hope we finally do write an article for the Annals of Improbable Research one day, Jon.

I would like to thank a number of other scientists for their support, mentoring, and education. Lee Homer and Scott Anderson have been wonderful collaborators and were kind enough to take me in for a week and show me the ropes of *HST* analysis. Simon Portegies Zwart introduced me to Amsterdam and to theory, both of which were strange and exciting. Frank Verbunt has provided me with enough scientific guidance to fill volumes. Kurt Weiler, Alex Filippenko, and Roger Chevalier have given me an unparalleled education in core-collapse SNe. Although I have not worked

with him in a scientific capacity, Ron Remillard has given me an extremely valuable insight into the community.

Many teachers in both high school and in my undergraduate career at MIT have been inspiring, challenging, and good friends. I would like to thank David Thorburn, Brian Lazare, James Flatley, Troy Vachetta, Michael Begg, Joe Dedalonis, and Dave Gonder for being wonderful teachers.

My friends back home have provided much needed relief from the stress of MIT life for the past eight years and have continued to serve as a reminder that there exists an entire world outside of Cambridge, MA. Big thanks to Jeremy Thompson, Keith Kliebert, Jen Kliebert, and Jon Belteau! I could never express how lucky I am to have friends like you.

I'd like to give a collective thanks to my friends and brothers at TEP. Living there was one of the best experiences of my life. My housemates over the past four years have given me countless happy memories and always made it much easier to leave the office. Thanks to Tori Low, Cyrus Dolph, Eric Traub, Andy Sparks, Dan Good, James Tanabe, Ariel Salomon, Kevin Simmons, Walter Holland, and Abby Spinak.

Dasha Lymar understands the good and important things in life. She has been supportive, loving, and caring. Her help in getting me through this final stretch at MIT is but a small part of the many ways in which she enriches my life. Thank you, Dasha.

Finally, I would like to thank my family, whose love, support, and sacrifice have made all of my accomplishments possible. My parents worked hard to give me this rare opportunity, and I am forever grateful. My brother has been a role model for me, and I continue to aspire to his kindness, intelligence, and good nature. Thank you, Mom, Dad, and Noel. I hope that I continue to do you proud.

Preface

This thesis is divided into two parts, each focusing on distinct areas of my research. Chapters 1–4 deal with my work on two Galactic globular clusters, and chapters 5–8 deal with my work on two recent core collapse supernovae.

Contents

List of Figures

List of Tables

Part I

X-ray Studies of Galactic Globular Clusters

Chapter 1

Introduction

1.1 What Are Globular Clusters?

Globular clusters are densely packed, gravitationally bound, roughly spherical conglomerations of between 10^4 and 10^6 stars. They are found around galaxies, and our own Milky Way harbors over 150 known clusters (Djorgovski & Meylan, 1993), with perhaps dozens more which have not been detected, primarily because of obscuration by the Galactic bulge.

Globular clusters have played a key role in a number of the revolutionary discoveries that have shaped modern astronomy. Their distribution in the sky — namely, their concentration in the direction of Sagittarius, which was first noted by John Herschel (1847) — provided the evidence that Harlow Shapely needed in 1918 to overturn the conventional wisdom of the day that the Solar System was the center of the Milky Way. They were integral to Walter Baade's pioneering work in the 1940s on stellar populations, and provided a testbed for the modern theory of stellar evolution based on the nuclear physics advances of the 1940s and 1950s. Perhaps the most consequential impact of globular clusters thus far has been to set a lower bound on the age of the universe (e.g., Krauss 1998). However, despite their influence in astronomy for over a century, their internal dynamics and evolution are poorly understood.

1.2 Internal Dynamics — The Role of Binary Systems

We know from observations that globular clusters are very efficient catalysts in forming unusual binary systems, such as low-mass X-ray binaries (LMXBs), cataclysmic variables (CVs), and millisecond pulsars (MSPs), with formation rates per unit mass exceeding those in the galactic disk by orders of magnitude (Clark, 1975). This binary population is, in turn, critical to the stabilization of globular clusters against gravitational collapse (Goodman & Hut, 1989); the long-term stability of a cluster is thought to depend crucially on tapping into the gravitational binding energy of such close binaries (Hut et al., 1992). The various dynamical interactions that can tap this energy (exchanges in encounters with binaries, direct collisions, destruction of binaries, and tidal capture) can change the state of the core dramatically and can kick stars and binaries out of the core or even out of the cluster altogether.

However, many details of these processes are not well understood, primarily because of the complex feedback between stellar evolution and cluster dynamics and the strong dependence on the cluster physical properties. As an example, consider LMXB and CV formation. The formation rate of a LMXB via "ordinary" evolution of a *primordial* binary is exceedingly small. In the core of a dense globular cluster, however, LMXBs can be formed dynamically. As the cluster evolves, the binaries evolve. In a dense globular cluster, two processes occur: (1) binaries are destroyed via encounters with other binaries or with single stars; and (2) new binaries are formed by tidal capture. Both the density of the core and the type of binary involved determine which process dominates. In the outermost regions of even the densest clusters, *primordial* binaries can evolve without being perturbed, and the currently observed binaries (such as CVs) will be mainly *primordial* ones, sparsely interspersed with binaries recoiled from the cluster core (e.g., the radio pulsar binary M15 C (Phinney & Sigurdsson, 1991)). The inner regions of the densest clusters should harbor hundreds of CVs formed via stellar encounters (di Stefano & Rappaport, 1994). The LMXBs, as well as the MSPs that evolve from them, are formed (almost) exclusively via stellar

encounters. For example, Davies & Hansen (Davies & Hansen, 1998) have shown that for an initial population of some 10^6 *primordial* binaries and $\sim 10^4$ neutron stars, one can plausibly account for the large number of *binary* radio pulsars that have been found in 47 Tuc (Camilo et al., 2000; Freire et al., 2001).

1.3 Previous Searches for Close Binaries

Early evidence for at least a small population of close binaries came from X-ray studies dating back to *Uhuru*, which revealed a dozen globular clusters each containing a highly luminous ($L_{\rm x} > 10^{36}$ ergs s^{-1}) X-ray source near their cores.[1] The X-ray spectra and luminosities indicate that these are LMXBs; orbital periods from 11 minutes to 17.1 hours have been determined for five sources. In 11 sources, Type I X-ray bursts have been detected (in 't Zand et al. 1999 and references therein), which are well explained as thermonuclear runaways on a neutron star surface (for a review see Lewin, van Paradijs, & Taam 1993). Optical counterparts have been found for six bright sources (Deutsch et al., 1998; Heinke, Edmonds, & Grindlay, 2001; Homer et al., 2001, and references therein).

With the *Einstein* satellite, seven faint ($L_{\rm x} \lesssim 10^{35}$ ergs s^{-1}) sources were detected in the cores of as many clusters (Hertz & Grindlay, 1983a,b). With the *Röntgensatellit*, or *ROSAT*, the number of faint core sources (within two core radii of the centers) expanded to 40, including multiple sources in 47 Tuc, ω Cen, NGC 6397, NGC 6752 and others; an additional 17 faint sources were found farther out in the clusters (more than two core radii from the centers). Whereas virtually all of the core sources are related to the globular clusters, some of the sources outside the cores may be in the background or foreground (Verbunt, 2001, and references therein). Due to crowding and the limited accuracy of even the *ROSAT* positions (varying from 2–5″, depending on whether a secure optical identification allows accurate determination of the bore sight correction), optical identifications of faint X-ray sources in globular

[1] *Chandra* has revealed that M15 actually contains two highly luminous X-ray sources in its core (White & Angelini, 2001).

cluster cores remained tentative before the *Chandra* era, and some suggestions have been disproved with more accurate X-ray positions, as in 47 Tuc (Verbunt & Hasinger, 1998) and M 92 (Geffert, 1998; Verbunt, 2001). The only secure optical identification was that of a dwarf nova with a faint X-ray source 12 core radii from the center of NGC 5904 (Hakala et al., 1997; Margon, Downes, & Gunn, 1981). The radio pulsar in M 28 is another securely identified faint X-ray source (Lyne et al., 1987; Saito et al., 1997). Some identifications, like those in M 13, remain in doubt (Verbunt, 2001).

Progress in identifying the nature of the various faint X-ray sources has been very slow during the past two decades. However, this is now rapidly changing. With *Chandra*'s high sensitivity and unprecedented spatial resolution (see section 1.4.1), a revolution is underway in our understanding of the low-luminosity globular cluster X-ray sources and their association with the binary populations of globular clusters. To date, some results have already been reported for a 74 ks observation of 47 Tuc (Grindlay et al., 2001a), a 70 ksec observation of ω Cen (Rutledge et al., 2002), a 49 ks observation of NGC 6397 (Grindlay et al., 2001b), and the observations of NGC 6752 and NGC 6440, which are discussed in chapters 2 and 3 of this thesis. The *Chandra* observations have confirmed previously suggested optical counterparts for faint X-ray sources in the cores of these clusters and made numerous additional identifications.

Searches have been made in the optical as well for binaries, and many binaries have been found via their radial velocity measurements or photometric variability (e.g., Hut et al. 1992 and references therein). However, the majority of those are long period binaries. In order to find close binaries, optically outbursting objects, which would most likely be CVs, were looked for, but deep photometric searches with *HST* into the cores of a number of clusters found surprisingly few such optically outbursting objects, which suggested a serious discrepancy with theoretical predictions for CVs (Shara & Drissen, 1995; Livio, 1996; Shara, Zurek, & Rich, 1996). This dilemna has only recently been rectified, due in large part to the results presented in this thesis and the papers of Grindlay et al. (2001a,b).

1.4 Instrumentation

The nature of this work involves the investigation of sources within the extremely dense cores (10^{3-4} stars pc^{-3}) of globular clusters. Such observations demand the highest angular resolution available and were facilitated by two of of the National Aeronautical and Space Administration's "Great Observatories," namely, the *Chandra X-ray Observatory* (*Chandra*) and the *Hubble Space Telescope* (*HST*).

1.4.1 The *Chandra X-ray Observatory*

Launched on 1999 July 23 and named after Subramanyan Chandrasekhar, *Chandra* (Weisskopf et al., 2002) features the highest angular resolution yet available in X-ray astronomy. The observatory has a single Wolter type-I X-ray telescope with 4 nested mirror shells which focuses the X-rays onto one of two science instruments in the focal plane (see Fig. 1-1). The High Resolution Mirror Assembly (HRMA) has a focal length of roughly 10 m, an effective area which varies (non-uniformly) between 800 cm^2 at 0.25 keV and 100 cm^2 at 8 keV, and can achieve a point spread function (PSF) of 0.″5 (full width at half maximum), although this varies as a function of off-axis angle and energy.

The science instrument used in this work was the Advanced CCD Imaging Spectrometer (ACIS; Fig. 1-2), which comprises ten separate CCDs, each with 1024×1024 pixels, and each offering moderate spectral resolution in the 0.3–10 keV band (ΔE between 0.1–0.2 keV). Each pixel is 0.″492 on a side. Four of the front-side-illuminated (FI) CCDs are arranged in a square and form the ACIS-I (Imaging) array, which was optimized for imaging surveys. Four other FI CCDs and two back-side-illuminated (BI) CCDs form the ACIS-S (Spectroscopy) array, which was designed to be used in conjunction with the transmissions gratings on the observatory (these are not discussed here). The BI chips offer improved sensitivity at low energies, and the S3 chip (at the aimpoint of the ACIS-S array) has become the instrument of choice for imaging observations due to damage that occured early in the mission and which affected the FI CCDs much more severely than the BI CCDs. Both *Chandra* observations

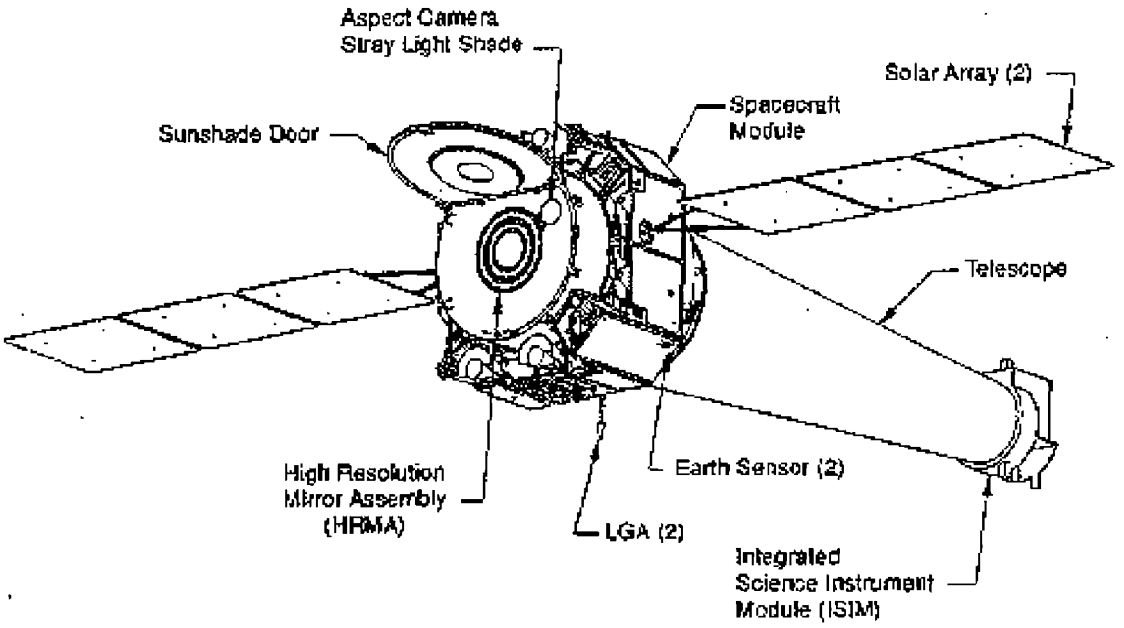

Figure 1-1: Schematic of the *Chandra X-ray Observatory* (NASA).

discussed in chapters 2 and 3 were taken with the telescope aimpoint on the S3 chip. The dependence of the point spread function as a function of angle away from this aimpoint is shown in Fig. 1-3. All sources discussed in chapters 2 and 3 fall within the dotted line, and therefore have PSFs of 1″ or better.

1.4.2 The *Hubble Space Telescope*

Deployed on into low-Earth orbit on 1990 Apr 25, *HST* features diffraction-limited optics and a host of various scientifc instruments. The 2.4 m reflecting telescope, with correcting optics, can deliver images with a resolution of better than 0.″1. The scientifc instrument used in this work is the Wide Field/Planetary Camera 2 (WF/PC2), which is a set of four CCDs that cover the range 1150Å–10500Å. Forty-eight broad- and narrow-band filters are available across this band. Three CCDs with a scale of 0.″1 per pixel and 800 × 800 pixels each are arranged in an "L" shape and form the Wide Field Camera. The Planetary Camera also has 800 × 800 pixels but with a scale of 0.″046 per pixel. The configuration is shown in Fig. 1-4.

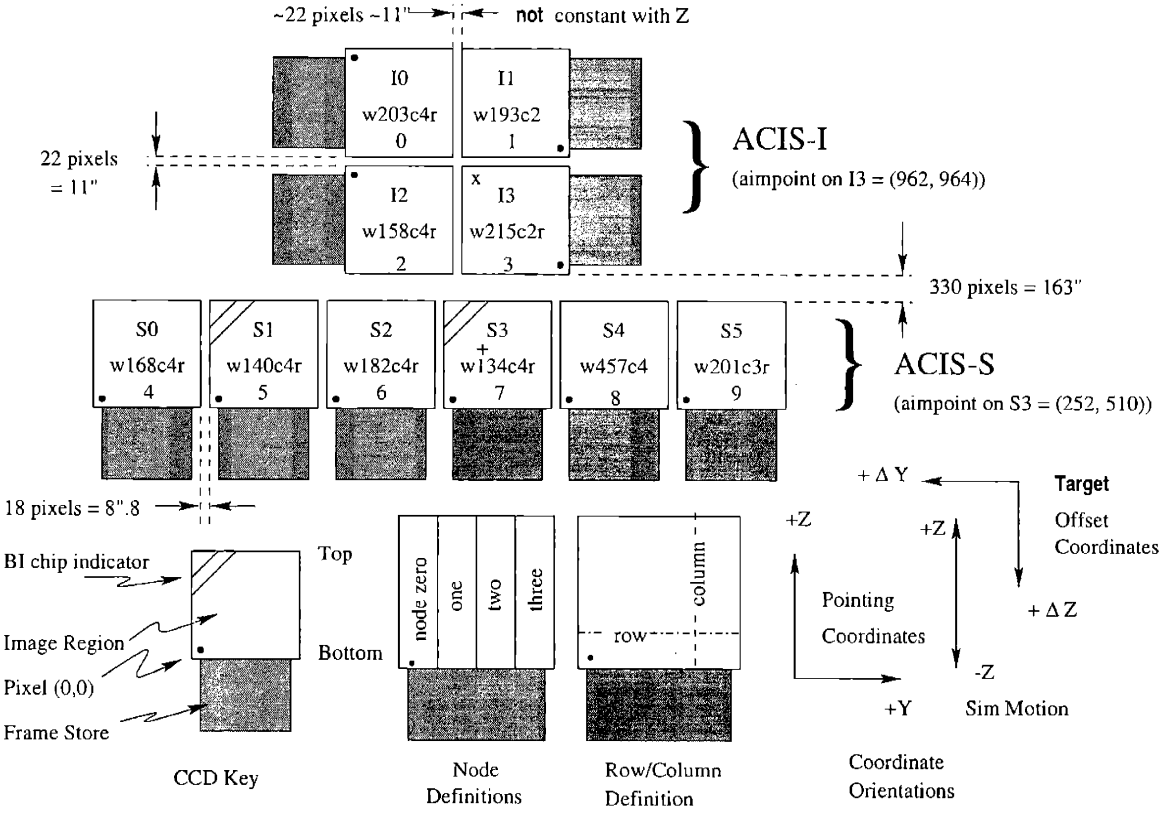

Figure 1-2: A schematic drawing of the ACIS focal plane; insight to the terminology is given in the lower left. Note the nominal aimpoints: on S3 (the '+') and on I3 (the 'x'). The view is along the optical axis, from the source towards the detectors, (-X). The numerous ways to refer to a particular CCD are indicated: chip letter+number, chip serial number, and ACIS chip number. (NASA).

1.5 Investigation

The original aim of this work was to identify the nature of the low-luminosity X-ray sources in globular clusters. For over almost 20 years, since the launch of the *Einstein* satellite, the existence of these sources has been known, and about sixty had been observed before the launch of *Chandra*. However, only two had been successfully identified in the optical or radio. There was much disagreement in the literature about the nature of the rest of these sources. Both quiescent low-mass X-ray binaries and cataclysmic variables were expected on theoretical grounds to be present in large numbers in globular clusters. In addition, millisecond pulsars and RS CVn systems

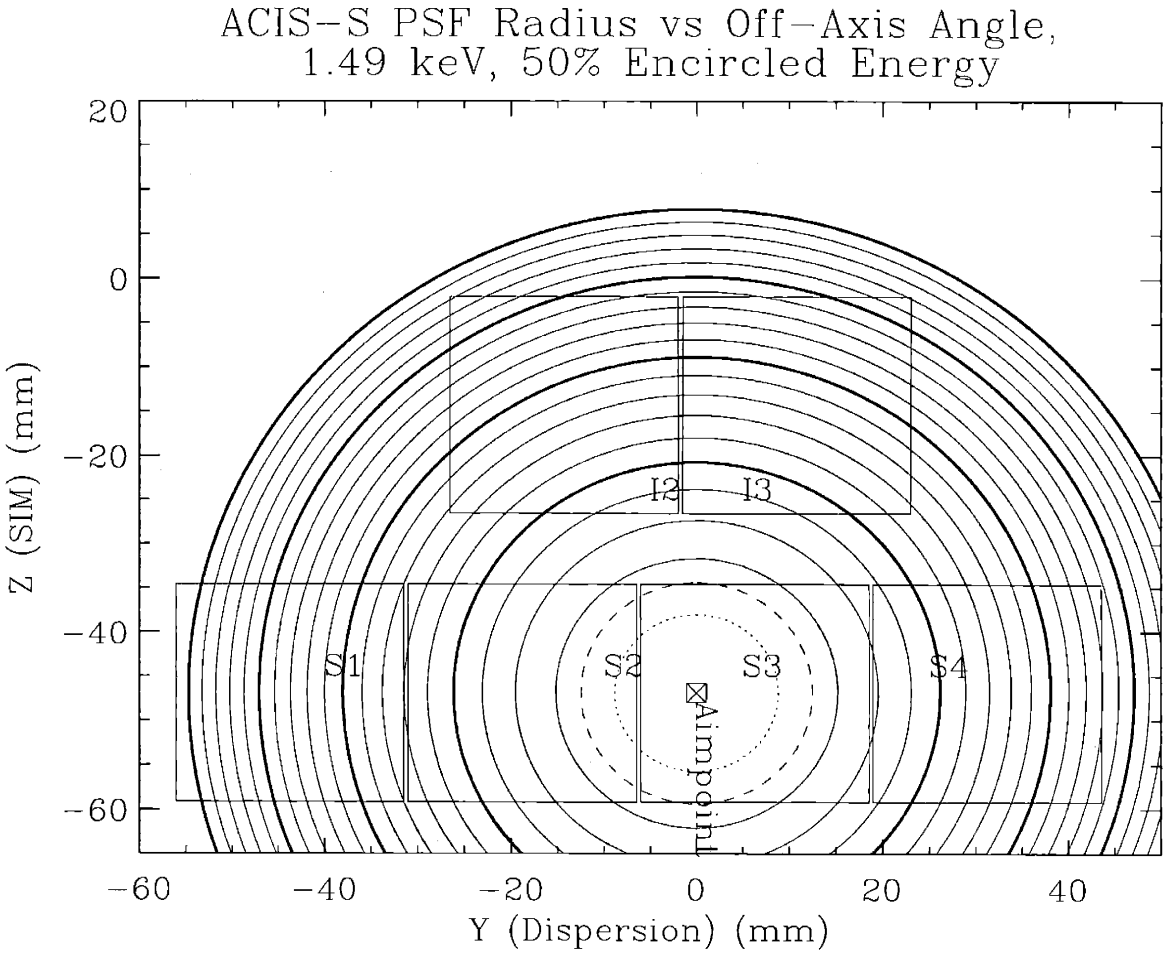

Figure 1-3: Contours of constant 50% encircled energy at 1.49 keV relative to the ACIS-S aimpoint on S3. The dotted line is 1″, the dashed line is 1.″5 . The remainder are 1″ intervals. The thicker solid lines highlight the 5″, 10″, 15″, and 20″ contours. (NASA).

were proposed to account for at least some portion of this population.

In the course of the analysis of NGC 6752, it was clear that the *Chandra* data alone were not enough to identify and classify the X-ray sources that we found. Although the sources were real to a high significance, they often had too few counts (sometimes only three or four) to do anything meaningful with their spectra. We therefore turned to *HST* data. Precision astrometry was performed to *independently* bring both the *Chandra* and *HST* data into the International Celestial Reference System. We were then able to identify with certainty the optical and radio counterparts to the X-ray sources. As expected, all of the suspected sources — low-mass X-ray binaries,

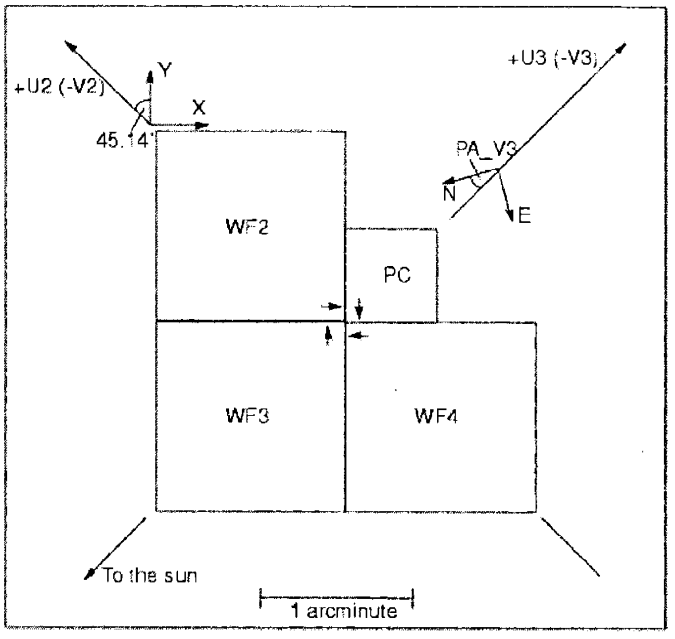

Figure 1-4: WFPC2 Field-of-View Projected on the Sky. The readout direction is marked with arrows near the start of the first row in each CCD. The position angle of V3 varies with pointing direction and observation epoch. (NASA).

cataclysmic variables, millisecond pulsars, and RS CVn systems — were detected.

It would certainly have been nice to have a wealth of *HST* observations of NGC 6440 available, as was the case for NGC 6752, but the moderate reddening ($E_{B-V} = 1.07$) and distance (8.5 kpc) to the cluster would require an unjustifiable amount of *HST* observing time to accomplish the kind of multicolor and narrowband imaging that was done for NGC 6752. With NGC 6440, our focus was necessarily limited to the X-ray data. In this work, we found the first evidence that the X-ray luminosity functions differ among globular clusters.

Bibliography

Camilo, F., Lorimer, D. R., Freire, P., Lyne, A. G., & Manchester, R. N. 2000, ApJ, 535, 975

Clark, G. W., 1975, ApJ, 199, L143

Davies, M. B. & Hansen, B. M. S. 1998, MNRAS, 301, 15

Deutsch, E. W., Anderson, S. F., Margon, B., & Downes, R. A. 1998, ApJ, 493, 775

di Stefano, R. & Rappaport, S., 1994, ApJ, 423, 274

Djorgovski, S. G. & Meylan, G. 1993, in Structure and Dynamics of Globular Clusters, ASP Conf. Ser. 50, eds. Djorgovski S. G. & Meylan, G., (San Francisco: ASP), p. 325

Freire, P. C., Camilo, F., Lorimer, D. R., Lyne, A. G., Manchester, R. N., & D'Amico, N. 2001, MNRAS, 326, 901

Geffert, M. 1998, A&A, 340, 305

Goodman, J. & Hut, P., 1998, Nature, 339, 40

Grindlay, J. E., Heinke, C., Edmonds, P. D., & Murray, S. S. 2001a, Science, 292, 2290

Grindlay, J. E., Heinke, C. O., Edmonds, P. D., Murray, S. S., & Cool, A. M. 2001b, ApJ, 563, L53

Hakala, P. J., Charles, P. A., Johnston, H. M., & Verbunt, F. 1997, MNRAS, 285, 693

Heinke, C. O., Edmonds, P. D., & Grindlay, J. E. 2001, ApJ, 562, 363

Herschel, J. 1847, in Results of Astronomical Observations made at the Cape of Good Hope (London: Smith, Elder, & Co.)

Hertz, P. & Grindlay, J. E. 1983a, ApJ, 267, L83

Hertz, P. & Grindlay, J. E. 1983b, ApJ, 275, 105

Homer, L., Anderson, S. F., Margon, B., Deutsch, E. W., & Downes, R. A. 2001, ApJ, 550, L155

Hut, P., McMillan, S., Goodman, J., Mateo, M., Phinney, E. S., Pryor, C., Richer, H. B., Verbunt, F., & Weinberg, M. 1992, PASP, 104, 981

in 't Zand, J. J. M., Verbunt, F., Strohmayer, T. E., Bazzano, A., Cocchi, M., Heise, J., van Kerkwijk, M. H., Muller, J. M., Natalucci, L., Smith, M. J. S., & Ubertini, P. 1999, A&A, 345, 100

Kraus, L. M. 1998, ApJ, 501, 461

Lewin, W. H. G., van Paradijs, J., & Taam, R. E. 1993, Space Science Reviews, 62, 223

Livio, M. 1996, ASP Conf. Ser. 90, 125

Lyne, A. G., Brinklow, A., Middleditch, J., Kulkarni, S. R., & Backer, D. C. 1987, Nature, 328, 399

Margon, B., Downes, R. A., & Gunn, J. E. 1981, ApJ, 247, L89

Phinney, E. S. & Sigurdsson, S. 1991, Nature, 349, 220

Rutledge, R. E., Bildsten, L., Brown, E. F., Pavlov, G. G., & Zavlin, V. E. 2002, ApJ, 578, 405

Saito, Y., Kawai, N., Kamae, T., Shibata, S., Dotani, T., & Kulkarni, S. R. 1997, ApJ, 477, L37.

Shara, M. M. & Drissen, L. 1995, ApJ, 448, 203

Shara, M. M., Zurek, D. R., & Rich, R. M. 1996, ApJ, 473, L35

Verbunt, F. 2001, A&A, 368, 137

Verbunt, F. & Hasinger, G. 1998, A&A, 336, 895

Weisskopf, M. C., Brinkman, B., Canizares, C., Garmire, G., Murray, S., & van Speybroeck, L. P. 2002, PASP, 114, 1

White, N. E. & Angelini, L. 2001, ApJ, 561, L101

Chapter 2

Faint X-ray Sources in NGC 6752

This chapter is based on the original paper:

> "Optical Identification of Multiple Faint X-ray Sources in the Globular Cluster NGC 6752: Evidence for Numerous Cataclysmic Variables," Pooley, D., Lewin, W. H. G., Homer, L., Verbunt, F., Anderson, S. F., Gaensler, B. M., Margon, B., Miller, J. M., Fox, D. W., Kaspi, V. M., & van der Klis, M., 2002, *The Astrophysical Journal*, Vol. 569, p. 405,

with the permission of the publisher, *The Astrophysical Journal.*

2.1 Abstract

We report on the *Chandra X-ray Observatory* ACIS-S3 imaging observation of the globular cluster NGC 6752. We detect 6 X-ray sources within the 10.″5 core radius and 13 more within the 115″ half-mass radius down to a limiting luminosity of $L_x \approx 10^{30}$ ergs s^{-1} for cluster sources. We reanalyze archival data from the *Hubble Space Telescope* and the Australia Telescope Compact Array and make 12 optical identifications and one radio identification. Based on X-ray and optical properties of the identifications, we find 10 likely cataclysmic variables (CVs), 1–3 likely RS CVn or BY Dra systems, and 1 or 2 possible background objects. Of the 7 sources for which no optical identifications were made, there was one which was detected in the

archival radio data we reanalyzed and another which was found to be a millisecond pulsar. Of the remaining sources, we expect that ~2–4 are background objects and that the rest are either CVs or millisecond pulsars whose radio emission has not been detected. These and other *Chandra* results on globular clusters indicate that the dozens of CVs per cluster expected by theoretical arguments are being found. The findings to date also suggest that the ratio of CVs to other types of X-ray sources is remarkably similar in clusters of very different structural parameters.

2.2 Introduction

NGC 6752 is at a distance of 4.1 ± 0.2 kpc (Renzini et al., 1996). The published optically derived center is at (J2000) $19^{\rm h}10^{\rm m}51\overset{\rm s}{.}8, -59°58'55''$ (Harris, 1996), but see §2.7. Its moderate optical reddening $E_{B-V} = 0.04$ may be converted to a nominal X-ray absorption column characterized by $N_{\rm H} = 2.2 \times 10^{20}$ cm^{-2} using the relation found by Predehl & Schmitt (1995). Its core radius $r_{\rm c}$ is $10\overset{''}{.}5$, and its half-mass radius $r_{\rm h}$ is $115''$ (Trager, Djorgovski, & King, 1993). We use these values throughout the paper.

Faint X-ray sources in NGC 6752 were first found by Grindlay (1993) on the basis of a 31.3 ks *ROSAT* HRI exposure, which revealed a double source in the core and two sources outside the core but within the half-mass radius. These sources were also detected with the *ROSAT* PSPC (Johnston, Verbunt, & Hasinger, 1994). Verbunt & Johnston (2000) co-added three *ROSAT* HRI observations for a total exposure of 72 ks and identified an X-ray source with the non-cluster member star TYC 9071 228 1, allowing an accurate solution of the bore sight correction and therewith an accurate ($\sigma \simeq 2''$) absolute positioning of the X-ray frame. They also resolved the central source into four sources and argued on the basis of the source density in the whole *ROSAT* image that the other sources within the half-mass radius were possibly related to the cluster. The best position for the northernmost *ROSAT* source in the core is marginally compatible with the previously published position of the southern of two H α emission objects and photometric variables with periods of 5.1 hr and 3.7 hr

discovered with *Hubble Space Telescope* (*HST*) observations by Bailyn et al. (1996).

Our *Chandra* X-ray observations are described and analysed in §2.3, our radio observations in §2.4, and our analysis of the *HST* observations in §2.5. The results are described in §2.6 and discussed in §2.7.

2.3 X-ray Observations

NGC 6752 was observed with the *Chandra X-ray Observatory* (Weisskopf, O'Dell, & van Speybroeck, 1996) for ∼30 ks on 2000 May 15. The observation was made with the Advanced CCD Imaging Spectrometer (ACIS) with the telescope aimpoint on the back-side illuminated S3 chip, which offers increased sensitivity to low-energy X-rays compared to the front-side illuminated chips. The entire region inside the cluster's half-mass radius fit on the 8.′3 square S3 chip. The data were taken in timed-exposure mode with the standard integration time of 3.24 sec per frame and telemetered to the ground in faint mode, in which a 3×3 pixel island is recorded for each event.

2.3.1 X-ray Data Reduction

Data reduction was performed using the CIAO 2.1 software provided by the *Chandra* X-ray Center[1]. We used the CALDB v2.6 calibration files (gain maps, quantum efficiency, quantum efficiency uniformity, effective area). Bad pixels were excluded, as were intervals of background flaring (∼1 ks). The effective exposure time for the observation after filtering for flares and correcting for dead time was 28.7 ks.

Starting with the raw (level 1) event list, we processed the data (using the tool *acis_process_events*) without including the pixel randomization that is added during standard processing.[2] This method slightly improves the point spread function (PSF). We then applied good-time intervals (both the ones supplied with the standard data

[1]See http://asc.harvard.edu.

[2]This randomization has the effect of removing the artificial substructure (Moiré pattern) that results as a byproduct of spacecraft dither. Since all of our observations contained a substantial number of dither cycles (one dither cycle has a period of ∼1000 sec), this substructure is effectively washed out, and there is no need to blur the image with pixel randomization.

products and our custom ones which excluded the period of background flaring) and filtered the data to include only events with *ASCA* grades of 0, 2, 3, 4, or 6 (this is the "standard" choice that generally optimizes the signal-to-background ratio; see the *Chandra* Proposer's Observatory Guide available from the website for more information). We also excluded software-flagged cosmic ray events. We used this filtered event list (level 2) for the subsequent analysis.

2.3.2 X-ray Source Detection

The wavelet-based *wavdetect* tool was employed for source detection. We found that the detection of sources was insensitive to whether we used a medium-band (0.5–4.5 keV) or full-band (0.3–8.0 keV) image. We detected 19 point sources within the cluster half-mass radius (Table 2.1) and another 21 on the rest of the S3 chip. We have numbered the sources in order of most counts to least in the 0.5–6.0 keV band. Our detection threshold was $\geq$5 counts in the 0.3–8.0 keV image. The absorbed flux of the faintest detected source was $\sim 6 \times 10^{-16}$ ergs cm^{-2} s^{-1}. Using the density of sources outside the half-mass radius, we estimate that about four sources within the half-mass radius are not associated with the cluster, which is in approximate agreement with the $\log N - \log S$ relationships of Giacconi et al. (2001). All 19 possible cluster sources are consistent with being point sources, with the possible exception of CX12. Comparing the observed radial surface brightness profile of this source to one predicted for a source of its intensity and at its location on the chip, we find that it is inconsistent with being a single point source at 94% confidence ($\chi^2 = 12.2$ for 6 degrees of freedom). It is most likely a blend of multiple sources.

The central 1′.6 portion of NGC 6752 is shown in Fig. 2-1. Overlaid on this image are the source extraction regions determined by *wavdetect*, a dashed circle indicating the core radius, a + indicating the published optical center of the cluster, and a × indicating the true center (Bailyn, 2002).

Table 2.1: NGC 6752 X-ray Sources.

Src[a]	RA (J2000)[b]	Dec (J2000)[b]	Detected Counts/Corrected Counts[c]			L_x (ergs s^{-1})[d]	Cntrpt[e]	ID[f]
			X_{soft}	X_{med}	X_{hard}	[0.5–2.5 keV]		
CX1	19:10:51.098	−59:59:11.83	536/588.0	936/1014.0	444/457.0	2.1×10^{32}	Opt./X7b	CV
CX2	19:10:55.972	−59:59:37.33	196/215.3	315/343.5	130/135.3	6.0×10^{31}	Opt./X14	CV
CX3	19:10:40.318	−59:58:41.29	177/195.4	274/297.6	104/107.0	5.3×10^{31}	Opt./X6	CV
CX4	19:10:51.546	−59:59:01.71	132/146.0	219/238.7	94/97.1	4.0×10^{31}	Opt./B1	CV
CX5	19:10:51.374	−59:59:05.11	94/103.7	175/190.3	86/88.7	3.6×10^{31}	Opt.	CV/BY Dra
CX6	19:10:51.462	−59:59:26.99	83/90.9	121/130.9	41/42.1	2.2×10^{31}	Opt./X22	CV
CX7	19:10:51.467	−59:58:56.72	58/64.3	95/103.6	44/45.4	1.9×10^{31}	Opt./B2	CV
CX8	19:11:02.944	−59:59:41.89	83/90.8	87/94.5	4/3.9	2.1×10^{31}	—	
CX9	19:10:51.720	−59:58:59.16	47/52.0	65/70.8	19/19.5	1.3×10^{31}	—	
CX10	19:10:54.706	−59:59:13.87	13/14.2	25/27.0	12/12.3	6.0×10^{30}	Opt.	CV
CX11	19:10:52.376	−59:59:05.56	22/24.1	26/28.0	5/5.0	6.2×10^{30}	Rad.	PSR D
CX12	19:10:52.694	−59:59:03.27	19/20.8	23/24.7	4/3.9	5.6×10^{30}	—	
CX13	19:10:40.565	−60:00:06.07	13/13.8	18/18.6	7/6.8	4.6×10^{30}	Opt.	CV
CX14	19:10:52.039	−59:59:09.12	15/16.4	15/16.0	0/–	4.2×10^{30}	—	
CX15	19:10:55.798	−59:57:45.53	8/8.5	10/10.4	2/1.9	3.2×10^{30}	Opt.	CV/Gal.
CX16	19:10:42.474	−59:58:42.83	8/8.7	9/9.5	1/0.9	3.0×10^{30}	Opt.	BY Dra
CX17	19:11:05.279	−59:59:04.03	3/3.2	7/7.4	4/4.0	2.7×10^{30}	Rad.	Gal.
CX18	19:10:52.006	−59:59:03.69	7/7.7	7/7.5	0/–	2.7×10^{30}	—	
CX19	19:10:55.577	−59:59:17.54	4/4.3	4/4.2	0/–	2.2×10^{30}	—	

[a]Sources are numbered according to their total counts.

[b]The *Chandra* positions have been corrected by $-0^s.044$ ($= -0''.33$) in RA and $-0''.17$ in Dec (see §2.4). We estimate the uncertainties in the final astrometric solution at about $0''.3$ in both RA and Dec. These uncertainties are much larger than the *wavdetect* centroiding uncertainties.

[c]Corrections are described in §2.3.3. X-ray bands are 0.5–1.5 keV (X_{soft}), 0.5–4.5 keV (X_{med}), and 1.5–6.0 keV (X_{hard}).

[d]For sources CX1–CX9, L_x comes from an average of the unabsorbed luminosities of the best-fit models for each source (see Tables 2.2 and 2.3). A linear relation between L_x and X_{med} counts for these sources was derived and used to estimate L_x for sources CX10–CX19 based upon their X_{med} counts. Typical uncertainties in L_x are ∼20%.

[e]Type of counterpart (optical or radio) found and associations (if any) with previously reported sources. "X" numbers refer to the *ROSAT* sources of Verbunt & Johnston (2000). "B" numbers refer to the *HST* sources of Bailyn et al. (1996). Note that our *HST* positions for these variables are very different from those given by Bailyn et al. (see §2.5.1).

[f]See §2.6 for details. "Gal." indicates the source may be a galaxy.

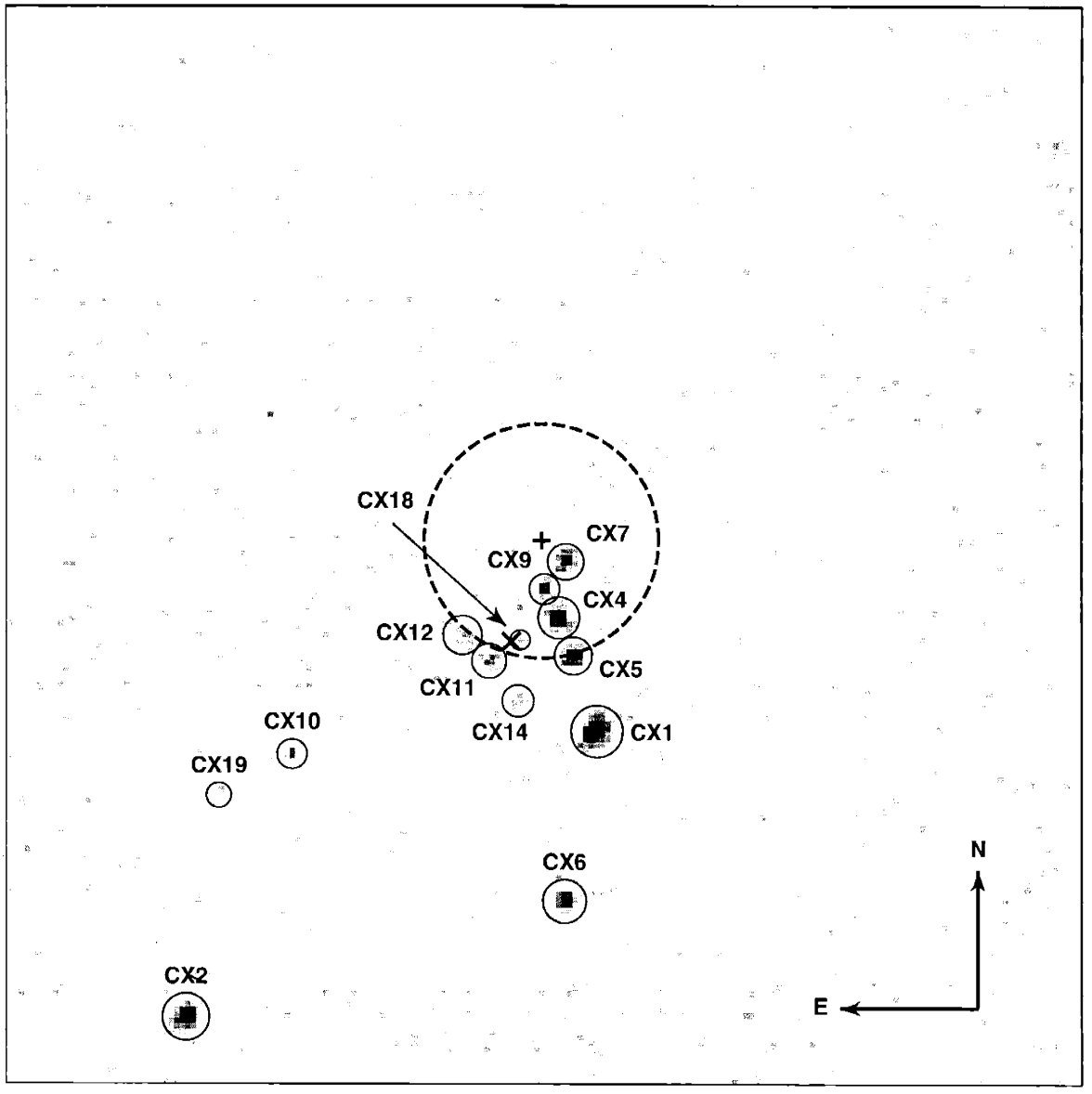

Figure 2-1: X-ray image of the central 1.′6 × 1.′6 region of NGC 6752. The solid circles indicate the source extraction regions as determined by *wavdetect*. The published optical cluster center is indicated with a +, and the true optical center with a × (Bailyn, 2002). The dashed circle is the 10.″5 core radius of the cluster. Each pixel is a 0.″492 square.

2.3.3 X-ray Count Rates

Source counts were extracted in a variety of energy bands. We found that the most useful data were between 0.5 and 6.0 keV, as this range preserved almost all of the source counts while limiting the background contribution. We focus on the following bands for hardness ratios and the X-ray color-magnitude diagram (CMD): 0.5–1.5 keV

(X_{soft}), 0.5–4.5 keV (X_{med}), and 1.5–6.0 keV (X_{hard}). While somewhat arbitrary, this choice allows a direct comparison with the results of Grindlay et al. (2001a) on 47 Tuc, which has a similar distance and column density.

The detected count rate was corrected for background, exposure variations, and foreground photoelectric absorption. The background count rate in each band was estimated from an annulus around the innermost sources. The inner radius was 29″, and the outer radius was 70″. No sources were present within the annulus. Because of the spacecraft's dither, some sources passed in and out of bad columns on the CCD. To account for the ∼4% variations in exposure that resulted, we applied multiplicative corrections based on the ratio of a source's average effective area in each of the three bands to the average effective area in the same band of CX15, which had the highest average exposure. The individual effective area curves for the sources were made using the CIAO tool *mkarf*. The average effective area of CX15 in each of the bands was 591 cm^{-2} (X_{soft}), 465 cm^{-2} (X_{med}), and 377 cm^{-2} (X_{hard}).

To correct for the column density to NGC 6752, we used XSPEC (Arnaud, 1996) to examine the effects of absorption on three spectra characteristic of what one might expect to find in a globular cluster: a 3 keV thermal bremsstrahlung (for CVs; Richman 1996; van Teeseling, Beuermann, & Verbunt 1996), a 0.3 keV blackbody (for quiescent LMXBs; Verbunt et al. 1994; Asai et al. 1996, 1998; as substitute for the more correct neutron-star atmosphere models, see Rutledge et al. 2001 and references therein), and a power law with a photon index of $\Gamma = 2$ (for MSPs; Becker & Trümper 1999). In each of our three bands, we took the ratio of the unabsorbed count rate to one absorbed by a column density of $N_H = 2.2 \times 10^{20}$ cm^{-2}. Because this is a fairly low column density, the effects were small on each of the three model spectra. We used a simple average of the ratios to derive the following correction factors for the observed count rate in each band: 1.084 (X_{soft}), 1.067 (X_{med}), and 1.010 (X_{hard}). Table 2.1 lists both the observed and fully corrected counts in each band for all 19 sources. The X-ray color-magnitude diagram based on the corrected counts is shown in Fig. 2-2. Note that the effect on the X-ray color-magnitude diagram of the correction for absorption is a uniform shift of all points 0.03 units up and 0.02 units to the

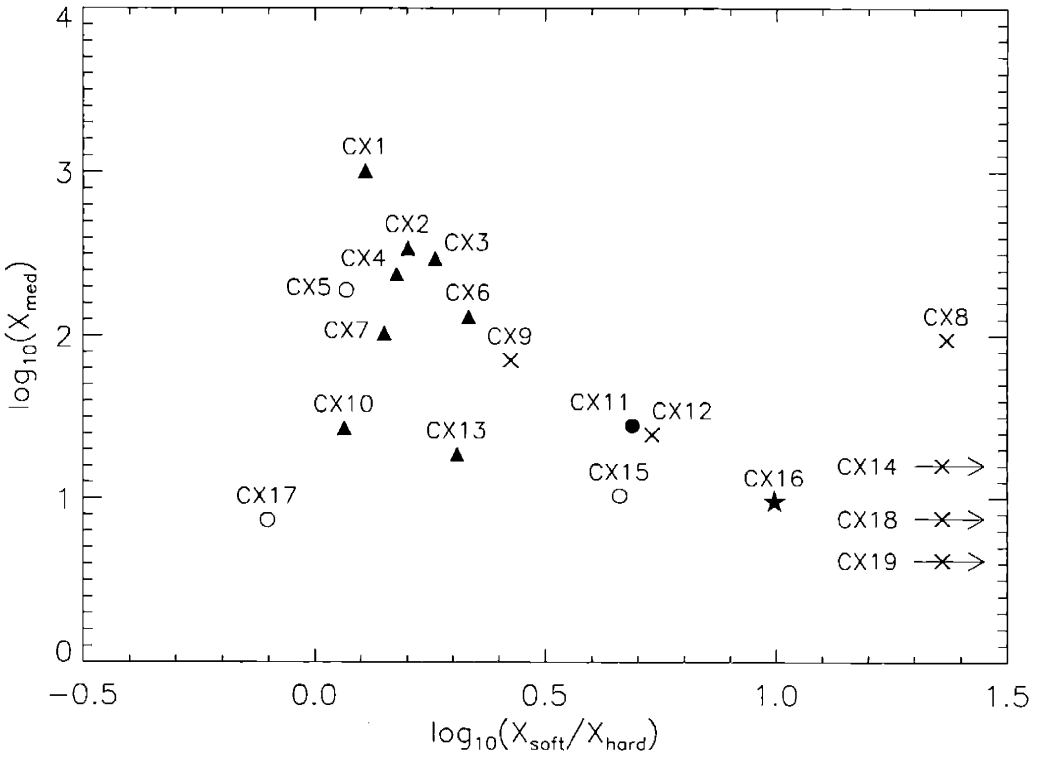

Figure 2-2: X-ray color-magnitude diagram for NGC 6752. The X-ray color is defined as the logarithm of the ratio of X_{soft} (0.5–1.5 keV) corrected counts to X_{hard} (1.5–6.0 keV) corrected counts, and the magnitude is the logarithm of X_{med} (0.5–4.5 keV) corrected counts. Probable source natures are indicated by symbols (▲ for CVs, ★ for BY Dra, ● for MSPs, ○ for ambiguous sources with optical or radio counterparts, and × for sources with no radio or optical counterparts). The arrows indicate the magnitudes of the three sources (CX14, CX18, and CX19) for which there were no detected counts in X_{hard}.

right.

2.3.4 X-ray Spectral Fitting

We used the CIAO tool *dmextract* to extract spectra of the brighter sources (CX1-CX9) and *dmgroup* to group the spectra to a selected number of counts per bin. CX1 was grouped to contain $\geq$35 counts per bin, CX2–CX4 were grouped at $\geq$15 counts per bin, and CX5–CX9 at $\geq$10 counts per bin. Background-subtracted spectral modeling was performed with XSPEC using data in the 0.3–8.0 keV range.

We fit three different models to each of the nine brightest sources (CX1–CX9): thermal bremsstrahlung (TB), blackbody (BB), and power law (PL). For CX1, the column density was allowed to vary and compared to a fixed value of $N_{\rm H} = 2.2 \times 10^{20}$ cm^{-2} for the cluster. For the other sources, however, we found that the data could not constrain $N_{\rm H}$ well and that all best-fit values were consistent with the column density from optical reddening. We therefore fixed $N_{\rm H}$ at the optical reddening value for the rest of the sources. The results are listed in Tables 2.2 and 2.3.

From the best-fit models, we calculated the unabsorbed source luminosities for CX1–CX9. Averaging the results from the best fits of each of the three models, we arrived at our estimate for the source luminosities listed in Table 2.1. The major sources of uncertainty in these luminosities arise from the scatter in the luminosities from the three different models and the uncertainties in each individual fit. The combined effect is typically around 20%. The uncertainties in distance (2.4%) and column density (1.7%) are negligible in comparison.

Fitting a linear relation to the CX1–CX9 luminosities vs. the corrected counts in $X_{\rm med}$, we have estimated the unabsorbed luminosities for sources CX10–CX19 based on their $X_{\rm med}$ counts. These are also listed in Table 2.1.

2.4 Radio Observations

We have analyzed archival radio observations of NGC 6752, carried out on 1995 February 02 using the Australia Telescope Compact Array (ATCA; Frater, Brooks, & Whiteoak 1992). Observations were made simultaneously at 1.4 and 2.4 GHz, and cover the entire *Chandra* field-of-view. At 1.4 and 2.4 GHz, the resulting spatial resolutions are $5\farcs7 \times 4\farcs9$ and $3\farcs2 \times 2\farcs7$ with sensitivities of 70 μJy beam^{-1} and 90 μJy beam^{-1}, respectively (where 1 Jy $= 10^{-26}$ W m^{-2} Hz^{-1}).

We find three source coincidences between the X-ray and 1.4-GHz radio images: one point source within NGC 6752's half-mass radius (CX17), one point source $\sim 6'$ from the cluster center (the corresponding X-ray source falls on chip S4), and some diffuse X-ray emission centered on a bright extended radio source (possibly a head-tail

Table 2.2: Spectral fits to the *Chandra* data of the brighter sources for fixed $N_{\rm H} = 2.2 \times 10^{20}$ cm^{-2}.

Src	Model[a]	kT (keV) or Γ	$L_{\rm x}$ (ergs s^{-1})[b] [0.5–2.5 keV]	$\chi^2_{\rm red.}$ (dof)
CX1	TB	$99.8^{+\infty}_{-66.4}$	1.8×10^{32}	1.04 (25)
	BB	$0.66^{+0.05}_{-0.04}$	2.0×10^{32}	4.05 (25)
	PL	$1.19^{+0.07}_{-0.09}$	1.7×10^{32}	1.17 (25)
CX2	TB	$20.8^{+146}_{-72.4}$	6.0×10^{31}	1.02 (19)
	BB	$0.45^{+0.08}_{-0.07}$	6.0×10^{31}	3.48 (19)
	PL	$1.32^{+0.15}_{-0.13}$	5.9×10^{31}	1.03 (19)
CX3	TB	$5.20^{+4.6}_{-1.9}$	5.3×10^{31}	1.20 (16)
	BB	$0.50^{+0.08}_{-0.11}$	5.5×10^{31}	3.53 (16)
	PL	$1.62^{+0.17}_{-0.17}$	5.2×10^{31}	1.23 (16)
CX4	TB	$17.1^{+117}_{-10.2}$	4.2×10^{31}	1.05 (12)
	BB	$0.61^{+0.10}_{-0.10}$	3.6×10^{31}	2.90 (12)
	PL	$1.35^{+0.18}_{-0.17}$	4.1×10^{31}	1.14 (12)
CX5	TB	>29	3.5×10^{31}	0.84 (14)
	BB	$0.65^{+0.12}_{-0.11}$	3.6×10^{31}	1.07 (14)
	PL	$0.93^{+0.25}_{-0.25}$	3.5×10^{31}	0.66 (14)
CX6	TB	$11.7^{+126}_{-7.2}$	2.2×10^{31}	1.02 (10)
	BB	$0.38^{+0.11}_{-0.07}$	2.2×10^{31}	2.41 (10)
	PL	$1.41^{+0.24}_{-0.22}$	2.2×10^{31}	1.06 (10)
CX7	TB	$34.2^{+\infty}_{-29.1}$	2.0×10^{31}	0.78 (8)
	BB	$0.45^{+0.31}_{-0.13}$	1.8×10^{31}	3.12 (8)
	PL	$1.33^{+0.35}_{-0.35}$	1.9×10^{31}	0.71 (8)
CX8	TB	$6.32^{+\infty}_{-5.0}$	2.2×10^{31}	2.07 (6)
	BB	$0.26^{+0.05}_{-0.04}$	1.7×10^{31}	1.35 (6)
	PL	$1.31^{+0.48}_{-0.49}$	2.3×10^{31}	2.11 (6)
CX9	TB	$3.34^{+115}_{-2.0}$	1.3×10^{31}	0.14 (4)
	BB	$0.34^{+0.10}_{-0.07}$	1.3×10^{31}	0.49 (4)
	PL	$1.64^{+0.48}_{-0.47}$	1.3×10^{31}	0.21 (4)

[a] TB = Thermal Bremsstrahlung, BB = Blackbody, PL = Power Law

[b] Unabsorbed luminosity for $d = 4.1$ kpc.

radio galaxy) outside the cluster. At 1.4 GHz the radio counterpart to CX17 has a flux density of 0.5 ± 0.1 mJy; no circular or linear polarization is detected from this source, with a 3σ upper limit on the fractional polarization of 35%. At 2.4 GHz this source is marginally detected at the 3σ level, with a flux density ~ 0.3 mJy.

Table 2.3: Spectral fits to the *Chandra* data of CX1 with $N_{\rm H}$ allowed to vary.

Model[a]	$N_{\rm H}$ (10^{20} cm^{-2})	kT (keV) or Γ	$L_{\rm x}$ (ergs s^{-1})[b] [0.5–2.5 keV]	$\chi^2_{\rm red.}$ (dof)
TB	$8.36^{+1.61}_{-3.21}$	$15.9^{+21.0}_{-6.3}$	2.1×10^{32}	0.66 (24)
BB	< 0.48	$0.67^{+0.04}_{-0.04}$	1.9×10^{32}	3.70 (24)
PL	$10.4^{+4.0}_{-3.7}$	$1.44^{+0.14}_{-0.13}$	2.2×10^{32}	0.73 (24)
BB+PL	$1.99^{+10.9}_{-1.99}$	$kT = 0.67^{+0.32}_{-0.17}$ $\Gamma = 1.23^{+0.36}_{-0.15}$	1.9×10^{32}	0.54 (22)

[a] TB = Thermal Bremsstrahlung, BB = Blackbody, PL = Power Law
[b] Unabsorbed luminosity for $d = 4.1$ kpc.

The absolute astrometry of the ATCA data in the International Celestial Reference System (ICRS) is accurate to $\lesssim 0\farcs1$. Based on the two point-source coincidences, we corrected the *Chandra* astrometry to align these sources. The correction was $-0\fs044$ ($= -0\farcs33$) in RA and $-0\farcs17$ in Dec.

Recently, a deep search of NGC 6752 with the Parkes radio telescope found 5 MSPs in the cluster (Possenti et al., 2001). D'Amico et al. (2002) report that their PSR D is consistent with CX11.

2.5 Optical Observations

The *HST* archive contains a substantial amount (~400 exposures) of WFPC2 imaging data covering the central regions of NGC 6752. Of particular utility are the data obtained by Bailyn and collaborators to suggest optical identification for two *ROSAT* sources in the core, the very ones we have now resolved into multiple *Chandra* sources. These consist of deep $H\alpha_{656}$ (F656N filter; i.e., 6560Å), R_{675} (F675W) and B_{439} (F439W) image sets, plus long time-series in V_{555} (F555W) and I_{814} (F814W) covering the core alone (for details see Bailyn et al. 1996), ideal for the identification of Hα emission and/or variable stars. Furthermore, additional U_{336} (F336W), nUV_{255} (F255W) are now available allowing for additional UV-excess selection. Unfortunately, not all of our *Chandra* sources have such complete optical coverage, owing to the nature of this archival data obtained for other unrelated projects. However,

only one X-ray source (CX8) lacks any *HST* color information at all.

In this section, we will first outline the optical astrometry undertaken to tie the *HST* images to the ICRS and thereby facilitate the alignment of our *Chandra* detections. We will then proceed to describe our optical data preparation and reductions, and end with our results.

2.5.1 Optical Astrometry

We aim to tie each *HST* pointing to the ICRS by finding matches between stars appearing on *HST* images and stars with accurate positions in either the Tycho-2 (Høg et al., 2000) or USNO A-2 (Monet, 1998) catalogs. Unfortunately, owing to the brightness and stellar density of the cluster core neither catalog extends to within 5′ of the center. However, the *HST* archive also contains numerous (largely V-band) images extending from the cluster center out to a $\sim$10′ radius, and these outermost images do overlap with the USNO A-2 coverage. On the basis of the *HST* pointing information (contained in each image header), we used the IRAF/STSDAS routine *metric* (which includes corrections for geometrical distortions towards the edge of each chip) to over-plot the nominal USNO star positions. To aid in the matching we also then degraded the *HST* images by convolving with a Gaussian to approximate the typical ground-based seeing of the plates used in deriving the catalog. It was then possible to make 58 reliable matches, on two separate *HST* datasets (i.e., from different satellite pointings), deriving offsets of 1.″1 and 0.″1 in RA and Dec., respectively. We found no evidence for a significant discrepancy in the nominal roll-angle, and hence we made no correction to this parameter. Taking the scatter to the astrometric fit and, in particular, the uncertainty in the roll-angle, we estimate residual uncertainties of a few tenths of an arcsecond.

Having aligned these outermost *HST* images, we then had to step in via intermediate overlapping *HST* images to find corrections for all the useful images of the cluster center. The procedure was essentially the same for each step. We measured the centroids of all bright (but not saturated) stars appearing in the overlap regions of two *HST* datasets and then applied *invmetric* to derive their nominal RA and

Dec according to the headers. Pairs were then matched and average offsets in sky coordinates calculated. Again, in no case did there appear to be any significant roll-angle discrepancies present. For these steps, we more typically found a few hundred matches, and hence the uncertainty in the measured offsets was negligible relative to that of the initial tie to the USNO A-2 (ICRS) frame.

The final stage made use of the prior identifications of two Hα bright stars by Bailyn et al. (1996). Over-plotting our *Chandra* sources for the core revealed that the two optical stars flagged in the Bailyn et al. finding chart (their Fig. 2) are indeed excellent matches to two of our X-ray sources. Specifically, our analyses of the relative positions and position angles in both the X-ray and the optical for these two flagged stars were fully in agreement. (Note that our astrometric solution for the position of these two objects differs in RA and Dec by $0^{s}.33$ (= $2''.6$) and $8''.4$, respectively, from the positions given by Bailyn et al. 1996. We attribute this to the error in the published optical center.) In our analysis, only a small $\sim 0''.5$ X-ray vs. optical offset remained. However, this is consistent with the expected uncertainty in our astrometric solution for these *HST* images relative to the ICRS frame. Hence, we decided to apply this small offset (assuming that these two stars are exactly at their *Chandra* positions) to the astrometry for all of our *HST* datasets. In order to be thorough, we opted to examine all optical/UV stars within $\sim 0''.5$ of each *Chandra* source position. Indeed, as we describe in detail below, we then uncovered at least 3 more strong candidate optical counterparts, none of which was more than $0''.1$ from the expected position based upon this offset. Such results are indeed consistent with uncertainties expected in the relative astrometry of the X-ray positions, combined with their transfer to a variety of *HST* datasets.

2.5.2 Optical Data Reductions and Analysis

The data from the *HST* archive are already well-calibrated (aside from astrometry), and only two steps remained. For each pointing and filter, at least two images were available, which were then used to remove the numerous cosmic ray events detected in each exposure. We used the *combine* task to calculate an average image and applied

one-sided sigma clipping (based on the median value of each pixel and a noise model for the detector) to exclude cosmic ray events. The images from each of the four chips were then trimmed to remove the partially masked edge regions.

We employed *daofind* in the IRAF implementation of DAOPHOT II (Stetson, 1992) to find all stars detected at approximately 3σ above background, and we then determined their centroids. Unfortunately, this method is not fool-proof, and we also had to add a number of faint stars by hand to our list and delete others affected by the ~20 saturated stars appearing on each frame. We excluded all stars with centers within ~10–15 pixels of any saturated pixels and also any stars lying on the cross-shaped diffraction patterns of the very brightest stars. Having thus created a master star list for each image, aperture photometry yielded magnitudes for a range of annuli close to the measured FWHM of the PSF. We note that, for the undersampled stellar PSFs of the PC and especially the WF chips, aperture photometry produced better results than our attempts at PSF fitting. The apertures we used are, however, far smaller than the standard 0.″5 aperture of the STMAG system (Holtzmann et al., 1995), and we therefore estimated the corresponding magnitude offsets needed relative to this large aperture for a number of bright (but non-saturated) and isolated stars on both the PC and WF chips. Applying both these offsets and the appropriate zeropoints based upon the sensitivity information in each header, we finally arrived at the STMAGs in a given filter for each star. We note that accurate estimation of the background contribution (especially critical for the faintest stars), is very difficult in such a crowded field. We adopted the mode value for an annulus surrounding each star. Tests, using either a fixed value as determined by averaging the results for the least crowded stars (farther from the core) or using the centroid of a Gaussian fit to the "sky" histogram instead of the mode, showed that we can expect systematic errors of ~0.1–0.2 mags in our final STMAG values. We have also applied approximate corrections to the magnitudes derived from aperture photometry to compensate for the time-dependent charge-transfer-efficiency effect and the so-called "long versus short anomaly," according to the formulae presented on the WFPC2 instrument web-

pages[3].

We constructed a variety of color-magnitude diagrams (CMDs) with all available data. The most informative of these are shown in Fig. 2-3, on which *all* stars located within the 0.″5 *Chandra* error circles are indicated by grey boxes. Numbers have been assigned to all candidate counterparts corresponding to the "CX" designation (i.e., our Star 1 is the counterpart to CX1). In this scheme, Stars 1 and 2 of Bailyn et al. (1996) are CX4 and CX7, respectively. In some cases, candidates are only abnormal in certain colors, but they are all labelled in each diagram. The results on each star are summarized in Table 2.4 and §2.6, and finding charts are shown in Fig. 2-4.

2.6 Results

The X-ray luminosities for the *Chandra* sources as listed in Tables 2.1 and 2.2 are in a range covered in the galactic disk by CVs, RS CVn binaries, and MSPs (e.g., see Fig. 8 in Verbunt et al. 1997). The soft X-ray transients with neutron stars in the galactic disk tend to have higher luminosities (the lowest luminosity known to us is that of Cen X-4 measured in August 1995 with the *ROSAT* HRI at 7×10^{31} ergs s^{-1} between 0.5 and 2.5 keV; Rutledge et al. 2001). Transients with a black hole have quiescent luminosities down to $\sim 10^{30}$ ergs s^{-1}; these luminosities may be due to chromospheric emission from the companion to the black hole, however (Rutledge et al., 2000). None of the X-ray spectra in our sample is as soft as would be expected for a low-mass X-ray transient in quiescence; all systems with enough signal (CX1–9), except CX8, can be fit with relatively hard thermal bremsstrahlung spectra, as expected for CVs.

A further clue to the nature of the *Chandra* sources may be obtained from the X-ray to optical flux ratio. For the *Chandra* sources whose optical counterparts have not been measured in V, we estimate $V \simeq 0.5(B+R)$. To allow comparison with the large database of *ROSAT*, we estimate that one X_{soft} *Chandra* count for our 29 ks NGC 6752 observation corresponds to a rate of 0.9×10^{-5} counts s^{-1} in channels 52–201 of the *ROSAT* PSPC. As shown in Fig. 2-5, the ratio of optical to X-ray flux

[3]See http://www.stsci.edu/instruments/wfpc2/.

Table 2.4: Summary of color selection for optical/UV counterparts

Optical star ID #	Offset from CXO posn.[a] in α ($''$)	in δ ($''$)	R_{675}	$H\alpha_{656} - R_{675}$	$B_{439} - R_{675}$	U_{336}	$U_{336} - V_{555}$	$nUV_{255} - U_{336}$
1	0.05	0.05	19.36 ± 0.02	-0.24 ± 0.03	-0.96 ± 0.02	19.78 ± 0.06	0.24 ± 0.08	0.05 ± 0.15
							0.96 ± 0.06	
2	–0.09	0.07	19.55 ± 0.01	-0.86 ± 0.07	-0.23 ± 0.02	19.83 ± 0.06	0.40 ± 0.06	0.36 ± 0.17
3	0.06	–0.11	21.48 ± 0.03	-0.07 ± 0.08	-0.19 ± 0.05	21.8 ± 0.2[b]	0.2 ± 0.2[b]	–
4	–0.01	0.06	20.83 ± 0.05	-0.76 ± 0.07	0.25 ± 0.13	20.14 ± 0.08	-0.33 ± 0.13	-0.05 ± 0.19
							-0.75 ± 0.09	
5	–0.02	0.00	19.13 ± 0.01	-0.12 ± 0.03	0.03 ± 0.02	19.72 ± 0.06	0.73 ± 0.13	1.82 ± 0.19
							0.68 ± 0.24	
6	–0.09	0.00	23.63 ± 0.27	-0.34 ± 0.49	-0.96 ± 0.32	–	–	–
7	0.01	–0.06	21.44 ± 0.06	-1.40 ± 0.08	-0.10 ± 0.10	21.78 ± 0.21	0.08 ± 0.26	–
							0.48 ± 0.21	
10	0.06	–0.05	–	–	–	19.67 ± 0.06		0.97 ± 0.19
							-0.27 ± 0.08	
11	–0.05	0.05	21.60 ± 0.28	-0.41 ± 0.35	0.07 ± 0.39	–	–	–
13	0.13	0.16	24.26 ± 0.15	-0.06 ± 0.47	-0.70 ± 0.20	–	–	–
15	0.21	–0.18	–	–	–	22.16 ± 0.24	0.16 ± 0.25	-0.62 ± 0.54
16	0.06	–0.18	19.05 ± 0.01	-0.17 ± 0.02	-0.05 ± 0.01	–	–	–

[a]The optical position is then given by *Chandra* X-ray value + offset in each coordinate. Note, the results are in true seconds of arc for both RA and Dec.

[b]These magnitudes are estimates based on the wide U (F300W) and wide V (F606W) data available ($U_{300} = 21.85 \pm 0.06$, $U_{300} - V_{606} = 0.36 \pm 0.06$) and transformations given in Holtzmann et al. (1995).

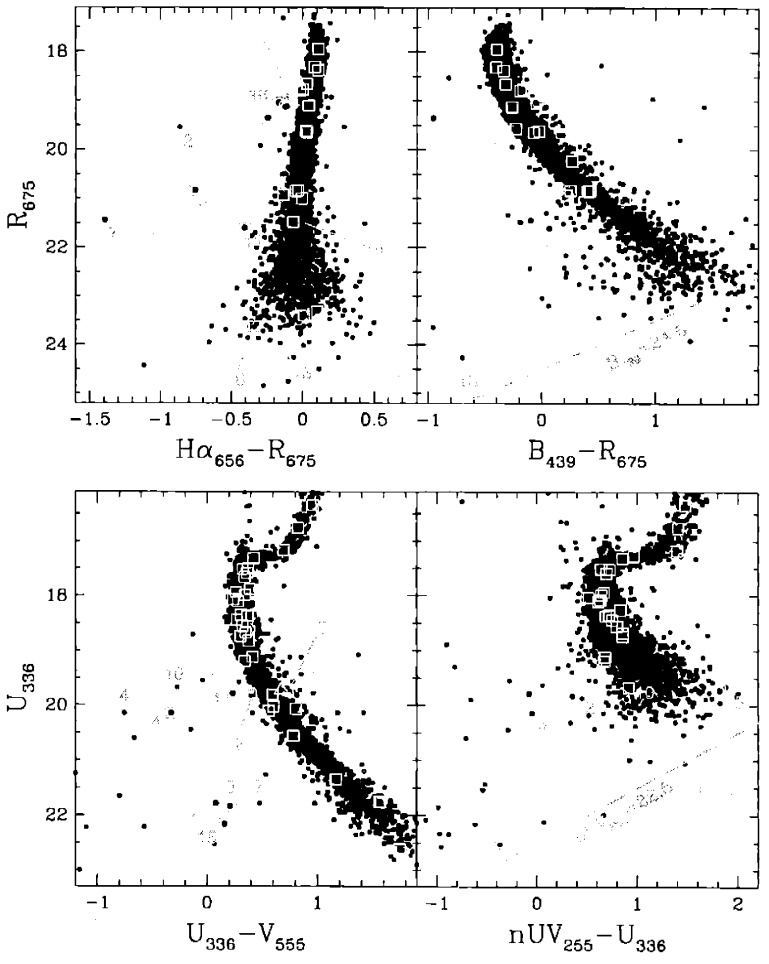

Figure 2-3: Color-magnitude diagrams for the central regions of NGC 6752. All the stars from both the PC field and one of the WF chip fields are plotted, along with all stars within 0.″5 of the *Chandra* source positions (indicated by grey boxes). Numbers refer to the candidate optical counterparts to the X-ray sources. All the R_{675}, $H\alpha_{656}$, and B_{439} band data shown in the upper panels are taken from *HST* observations in 1994 August, whereas the U_{336}, V_{555} and nUV_{255} data in the lower panels were obtained in 2001 March. Note that in the bottom left panel: (i) four candidates are plotted twice, according to their colors calculated from V_{555} band data taken either contemporaneously (i.e., that of 2001 March, squares) or older data from 1994 August (triangles), which clearly shows that three of them are variable; (ii) the data for Star 3 (marked as a hexagon) were obtained in the wide U (F300W) and wide V (F606W) filters and have been transformed before plotting.

of most Chandra sources in NGC 6752 suggests that they are cataclysmic variables. We discuss these first and the possible exceptions of CX12, CX16, and CX18 later.

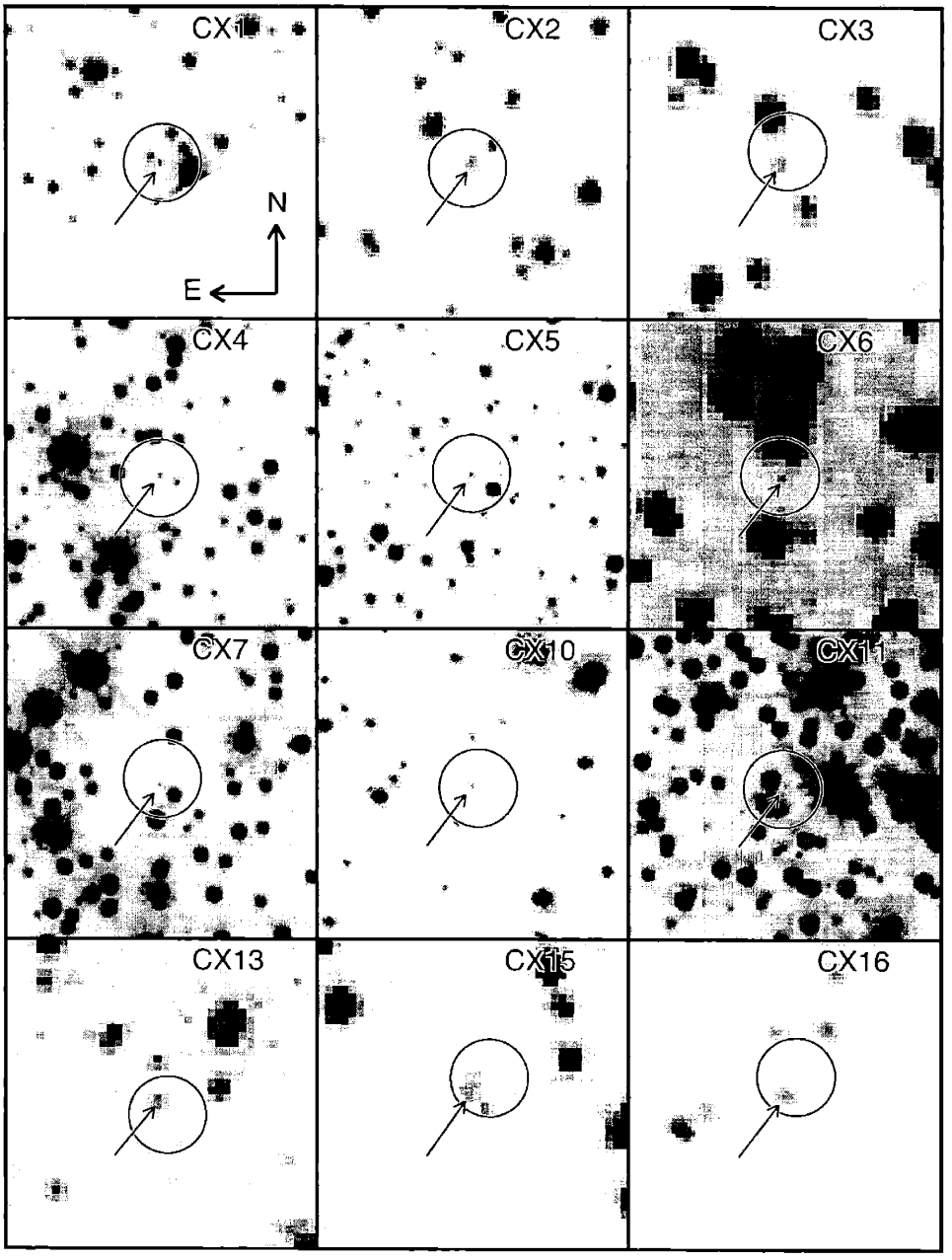

Figure 2-4: $4'' \times 4''$ finding charts for each optical counterpart candidate, obtained from *HST* archival data. These images were taken in V_{555}, apart from the charts for Stars 1 (U_{336}), 3, 6, and 13 (B_{439}), and 14 (U_{336}), for which V_{555} was either unavailable or the counterpart too blue or crowded to be visible. We have overlaid the $0\farcs5$ radius error circles for the *Chandra* source positions (in which we searched), and the candidate stars themselves are indicated by arrows. We also note that both the depth, greyscaling and pixel scales for the images are varied; as we have chosen the deepest, most well-sampled images (using dithered images where available) and then adjusted the greyscale to enhance visibility of the candidates.

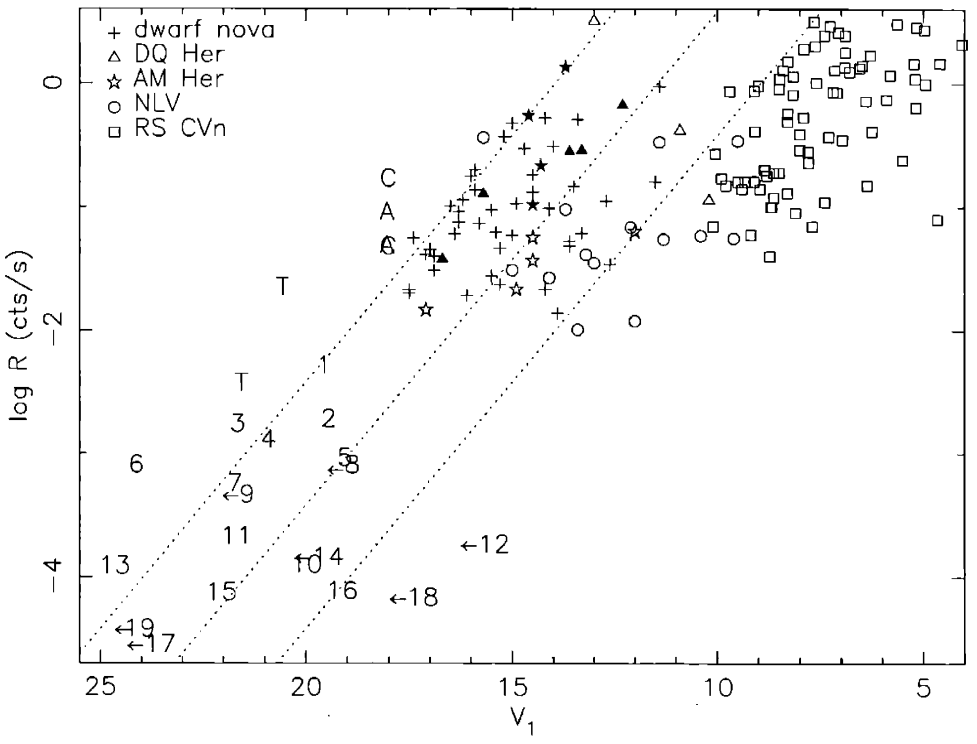

Figure 2-5: Comparison of the X-ray and optical fluxes of *Chandra* sources (numbers) in NGC 6752 to those of field sources (symbols and letters — "C" for Cen X-4, "A" for Aql X-1, and "T" for X9/V1 and X19/V2 in 47 Tuc; see Verbunt & Hasinger 1998 for more details). R is the equivalent *ROSAT* countrate in channels 52–201. V_1 is the visual magnitude and for CVs is the magnitude at which the system is most commonly found. *Chandra* sources with only optical upper limits are indicated by arrows. The top dotted line roughly separates soft X-ray transients (above) from CVs (below). The bottom dotted line roughly separates CVs from RS CVn systems (below).

Fig. 2-3 shows that the optical counterparts to CX1, CX2, CX3, CX4, CX7, CX10 and CX15 all have ultraviolet excesses (at U_{336} and/or nUV_{255}) with respect to the main sequence, as expected for cataclysmic variables. In $B_{439} - R_{675}$, the optical counterparts to CX1, CX3 and CX7 are still blue with respect to the main sequence, CX2 and CX4 are not distinguishable from the main sequence, and no information is available on CX10 and CX15. CX6, CX11 and CX13, for which no ultraviolet fluxes are available, are bluer than the main sequence in B_{439}. CX1, CX2, CX4, and

CX7 also show clear H α emission, and CX3, CX6 and CX13 do not. CX11 shows marginal H α excess, and no information is available for CX10 and CX15. On the whole, the optical properties for all these objects are compatible with those expected for cataclysmic variables, although CX11 and CX15 show evidence for having spatially extended emission and could be background galaxies. These and other early *Chandra* observations are finding the long-sought but, until recently, rarely observed population of CVs in globular clusters (Grindlay et al., 2001a,b).

CX12, CX18, and CX16 have (limits to) X-ray to optical flux ratios in the range of RS CVn systems. The limited information that may be obtained from the X-ray hardness of these three sources indicates that they may be as soft as expected for RS CVns. Interestingly, the $B_{439} - R_{675}$ color of CX16 places it on or slightly above the main sequence (see Fig. 2-3); its weak H α emission is not unprecedented in RS CVn type systems either. The optical counterparts for CX12 and CX18 would have visual fluxes more than about 3 mag fainter than our limits if they were dwarf novae in quiescence. They can be as bright as our limits if they are dwarf novae in outburst or nova-like variables of the UX UMa type (i.e., non-magnetic, permanently bright cataclysmic variables).

The location of CX5 in the optical color-magnitude diagrams is similar to that of CX16, as is its moderate H α emission. This suggests that it is an RS CVn system (more precisely, a BY Dra system). Its high X-ray to optical flux ratio and spectral hardness are more suggestive of a cataclysmic variable, however.

As remarked above, our *Chandra* sources have X-ray luminosities in the range also observed for MSPs in the galactic disk, and CX11 has been confirmed as an MSP (D'Amico et al., 2002). In this respect, the X-ray sources for which we have no optical counterparts could be MSPs for which the radio emission has not been detected. Because it was not found to be a pulsar by D'Amico et al. (2002), CX17 is most likely a background galaxy. As stated in §2.3.2, we expect $\sim$4 serendipitous background sources within the half-mass radius. The optically unidentified faint X-ray sources may well be such background sources. All of our likely source identifications are indicated in the X-ray color-magnitude diagram (Fig. 2-2).

2.7 Discussion

Our *Chandra* observation provides a dramatic improvement over the *ROSAT* HRI observations. The central X-ray emission of NGC 6752, resolved into 4 sources by the *ROSAT* HRI, is now found to be due to ten sources. The very accurate positions of these and other newly discovered sources allow secure identifications with *HST* sources and with one radio source.

Outside the core, the two sources CX2 and CX3 correspond to the *ROSAT* sources X14 and X6, respectively. From these two we determine an offset of (1.″9, −2.″1) that has to be applied to the *ROSAT* positions (as given by Verbunt & Johnston 2000) to align them with the *Chandra* frame.

In Fig. 2-6 we show the positions of the central sources that we have detected with *Chandra* superposed on a contour of the *ROSAT* HRI observation to which this offset has been applied. We then find that CX6 and CX1 correspond to X22 and X7b, respectively, whereas *ROSAT* source X7a has been resolved into CX11, CX12, and CX14, and X21 into CX4, CX5, CX7, and CX9.

From our spectral fits to the *Chandra* sources, we can estimate the *ROSAT* HRI and PSPC countrates for the luminosities at which *Chandra* detected them: 1 X_{soft} *Chandra* count in our observation corresponds to about 0.0045 cts/ks in the *ROSAT* HRI observations and to 0.009 cts/ks (channels 52–201) in the *ROSAT* PSPC observation. With this conversion we find that the luminosities of X14/CX2, X6/CX3, X22/CX6, X7a/(CX4, 5, 7, 9) and X21/(CX11, 12, 14) are constant within the errors between the *ROSAT* HRI and *Chandra* observation. Source X7b/CX1, however, was about 30% brighter in the *ROSAT* HRI than in the *Chandra* observation. The central conglomerate of sources was about 40% brighter during the *ROSAT* PSPC observation than during the *Chandra* observation; due to the lack of spatial resolution in the PSPC we cannot assign this to a specific *Chandra* source. We thus have evidence that the X-ray luminosity of at least one central source, CX1, is variable. Both X-ray and optical variability will be discussed in detail in Homer et al. (2003).

Chandra observations have been published for three other globular clusters that

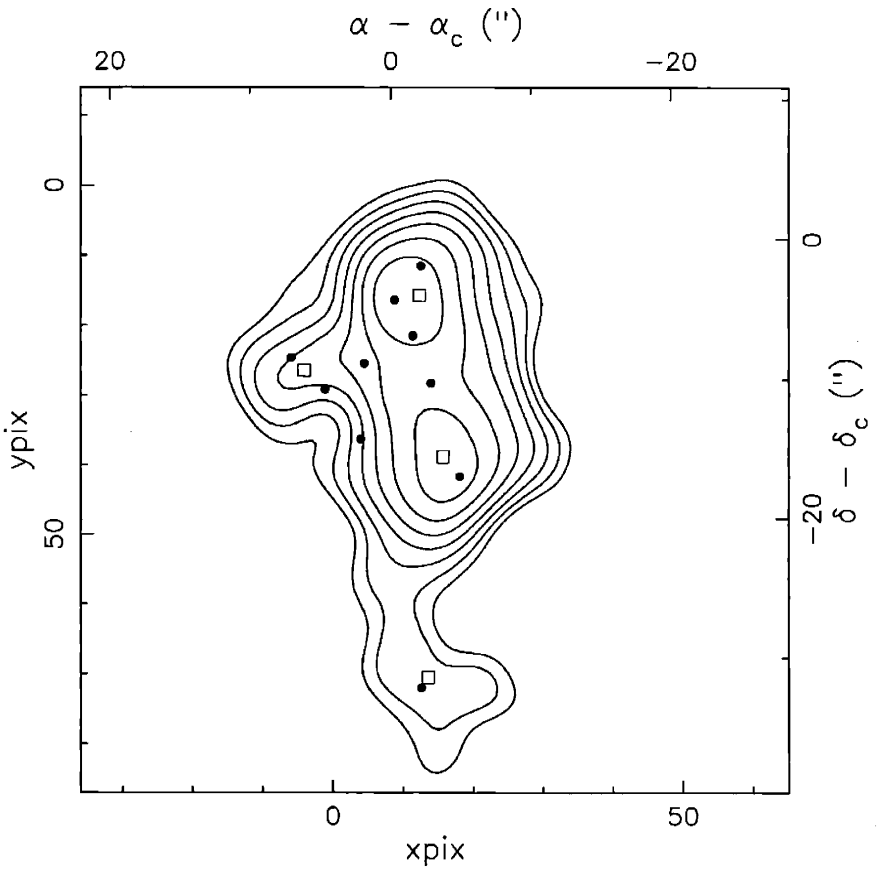

Figure 2-6: *ROSAT* HRI contours of NGC 6752 with positions of the central *Chandra* sources superposed (solid circles). *ROSAT* centroids are also indicated (boxes). The *ROSAT* contours were shifted (based on the correspondance of CX2 and CX3 with X14 and X6, respectively, from Verbunt & Johnston 2000) to align them with the *Chandra* frame.

do not contain a bright ($L_x > 10^{36}$ ergs s^{-1}) central X-ray source. The numbers of *identified* sources of various types are summarized in Table 2.5. Of these clusters, 47 Tuc has a larger core and slightly smaller central density than NGC 6752, causing the frequency of close encounters in 47 Tuc to be a factor ~10 larger than that in NGC 6752. NGC 6397 has a higher core density and much smaller core radius than NGC 6752, leading to a frequency of close encounters a factor ~10 smaller than in NGC 6752. Finally, ω Cen has a smaller central density and larger core than any of these clusters, and an encounter frequency similar to that in NGC 6752.

The X-ray luminosity of currently known quiescent soft X-ray transients with neutron stars in the Galactic disk does not drop below $\sim 10^{32}$ erg s^{-1}. If a similar lower

Table 2.5: The Nature of the Faint Globular Cluster X-ray Sources.

Cluster	Coll. Freq.[a]	qLMXB	CV	Bin.[b]	MSP[c]	Unc.[d]	Ref.[e]
47 Tuc	≡100	2	13	5	16	~ 60	1
ω Cen	16	1	2	0	0	~ 35	2
NGC 6752	9	0	11-14	1-3	1	6	3
NGC 6397	1	1	9	2	1	10	4

[a]Collision frequency scaled on the frequency in 47 Tuc. It is computed based on the central density ρ_o and core radius r_c given in the 1999 June 22 version of the catalogue described in Harris (1996), as $\propto \rho_o^2 r_c^3$.
[b]X-ray-active main-sequence binaries.
[c]X-ray detected MSPs.
[d]Unclassified.
[e]1. Grindlay et al. (2001a); 2. Rutledge et al. (2002); 3. this work;
4. Grindlay et al. (2001b)

limit holds for such transients in globular clusters, the *Chandra* observations provide a complete census of the quiescent transients in the observed four clusters, since none of the unclassified sources has an X-ray luminosity in excess of this threshold. If the number of quiescent soft X-ray transients scales with the collision frequency, we estimate that one such system is formed per ~30 of our normalized encounter frequencies, in which case the numbers of two, one, and zero in 47 Tuc, ω Cen, and NGC 6752 are well within expectation with Poisson statistics. The possible presence of such a source in NGC 6397, however, is somewhat surprising. A similar statement may be made for the X-ray detected MSPs: for an expected number of one per ten normalized encounter frequencies, only NGC 6397 is surprising in containing one. The presence of both a soft X-ray transient and an X-ray detected MSP in NGC 6397 suggests that clusters with the highest densities contain more such systems than indicated by the (average) collision number. This may be the consequence of more pronounced mass segregation in these clusters, which enhances the encounter rate of neutron stars with respect to the average encounter rate by concentrating them to the core.

The relative numbers of cataclysmic variables and binaries with a neutron star (i.e., permanently bright low-mass X-ray binaries or soft X-ray transients) according to theory depends on a number of factors including the retention fraction of neutron

stars (many neutron stars may be born with velocities that throw them out of the cluster, whereas all white dwarfs remain), the mass segregation in the cluster (which will concentrate the remaining neutron stars to the core where the close encounters occur, more so than the less massive white dwarfs), and the importance of primordial binaries evolving into cataclysmic binaries (important in clusters with small encounter frequencies). It is therefore interesting to see that the number ratio of (hitherto classified) cataclysmic variables to soft X-ray transients is not significantly different in 47 Tuc and NGC 6397, even though their encounter frequencies differ by two orders of magnitude. If many of the unclassified sources in 47 Tuc turn out to be cataclysmic variables, as is expected, the number ratio of cataclysmic variables to soft X-ray transients in it will even be higher. This again suggests that the average collision number of NGC 6397 underestimates the neutron star encounter rate. It should be noted that the census of cataclysmic variables through X-rays is certainly not complete, as many cataclysmic variables observed in the Galactic disk have X-ray luminosities below our threshold of 2×10^{30} ergs s^{-1} (see e.g. Fig. 8 in Verbunt et al. 1997). If we accept that X9/V1 and X19/V2 in 47 Tuc and CX6 in NGC 6752 are indeed cataclysmic variables, we see from Fig. 2-5 that their X-ray to optical flux ratio is higher than that of any cataclysmic variable in the galactic disk studied by Verbunt et al. (1996). The high X-ray luminosity of X9 has been confirmed with Chandra observations; the relative hardness of its X-ray spectrum suggests a cataclysmic variable, rather than a quiescent soft X-ray transient (Grindlay et al., 2001a)

Equally remarkable is the fact that the number ratios of cataclysmic variables to X-ray active binaries is ~ 2 in all four clusters under discussion, notwithstanding the large range of encounter frequencies. In dense clusters like 47 Tuc, most cataclysmic variables should be formed via close encounters, whereas a less concentrated cluster like ω Cen may have a significant contribution of primordial binaries evolved into cataclysmic variables (Verbunt & Meylan, 1988; di Stefano & Rappaport, 1994; Davies, 1997). As more sources are identified in 47 Tuc and ω Cen, and other clusters are studied as well, the numbers may become big enough to allow more definite

conclusions.

Finally, we were struck by the fact that all X-ray sources in Fig. 2-1 lie in a quadrant south of the published cluster center. In fact, we have recently learned that the published center is in error, and a recent determination of the optical center places it in the middle of the X-ray sources (Bailyn, 2002).

Bibliography

Arnaud, K. A. 1996, in ASP Conf. Ser. 101, Astronomical Data Analysis Software and Systems V, ed. G. Jacoby & J. Barnes, 17

Asai, K., Dotani, T., Mitsuda, K., Hoshi, R., Vaughn, B., Tanaka, Y., & Inoue, H. 1996, PASJ, 48, 257

Asai, K., Dotani, T., Hoshi, R., Tanaka, Y., Robinson, C. R., & Terada, K. 1998, PASJ, 50, 611

Bailyn, C. D., Rubenstein, E. P., Slavin, S. D., Cohn, H., Lugger, P., Cool, A. M., & Grindlay, J. E. 1996, ApJ, 473, L31

Bailyn, C. D. 2002, priv. communication

Becker, W. & Trümper, J. 1999, A&A, 341, 803

D'Amico, N., Possenti, A., Fici, L., Manchester, R. N., Lyne, A. G., Camilo, F., & Sarkissian, J. 2002, ApJ, 570, L89

Davies, M. B. 1997, MNRAS, 288, 117

di Stefano, R. & Rappaport, S. 1994, ApJ, 423, 274

Frater, R. H., Brooks, J. W., & Whiteoak, J. B. 1992, Journal of Electrical and Electronics Engineering Australia, 12, 103

Giacconi, R., Rosati, P., Tozzi, P., Nonino, M., Hasinger, G., Norman, C., Bergeron, J., Borgani, S., Gilli, R., Gilmozzi, R., Zheng, W. 2001, ApJ, 551, 624

Grindlay, J. E. 1993, in ASP Conf. Ser. 50, Structure and Dynamics of Globuler Clusters, ed. S. Djorgovski & G. Meylan, 258

Grindlay, J. E., Heinke, C., Edmonds, P. D., & Murray, S. S. 2001a, Science, 292, 2290

Grindlay, J. E., Heinke, C. O., Edmonds, P. D., Murray, S. S., & Cool, A. M. 2001b, ApJ, 563, L53

Harris, W. E. 1996, AJ, 112, 1487

Høg, E., Fabricius, C., Makarov, V. V., Urban, S., Corbin, T., Wycoff, G., Bastian, U., Schwekendiek, P., & Wicenec, A. 2000, A&A, 355, L27

Holtzmann, J. A., Burrows, C. J., Casertano, S., Hester, J. J., Trauger, J. T., Watson, A. M., & Worthey, G. 1995, PASP, 107, 1065

Homer, L., et al. 2003, in preparation

in 't Zand, J. J. M., Verbunt, F., Strohmayer, T. E., Bazzano, A., Cocchi, M., Heise, J., van Kerkwijk, M. H., Muller, J. M., Natalucci, L., Smith, M. J. S., & Ubertini, P. 1999, A&A, 345, 100

Johnston, H. M., Verbunt, F., & Hasinger, G. 1994, A&A, 289, 763

Lewin, W. H. G., van Paradijs, J., & Taam, R. E. 1993, Sp. Sci. Rev., 62, 223

Monet, D. G. 1998, BAAS, 193, 120.03

Possenti, A., D'Amico, N., Manchester, R. N., Sarkissian, J., Lyne, A. G., & Camilo, F. 2001, astro-ph/0108343

Possenti, A., Cerutti, R., Colpi, M., & Mereghetti, S. 2002, A&A, 387, 993

Predehl, P., & Schmitt, J. H. M. M. 1995, A&A, 293, 889

Renzini, A., Bragaglia, A., Ferraro, F. R., Gilmozzi, R., Ortolani, S., Holberg, J. B., Liebert, J., Wesemael, F., & Bohlin, R. C. 1996, ApJ, 465, L23

Richman, H. R. 1996, ApJ, 462, 404

Rutledge, R. E., Bildsten, L., Brown, E. F., Pavlov, G. G., & Zavlin, V. E. 2001, ApJ, 578, 405

Rutledge, R. E., Bildsten, L., Brown, E. F., Pavlov, G. G., & Zavlin, V. E. 2001, ApJ, 551, 921

Rutledge, R. E., Bildsten, L., Brown, E. F., Pavlov, G. G., Zavlin, V. E. 2000, ApJ, 529, 985

Stetson, P. B. 1992, in ASP Conf. Ser. 25, Astronomical Data Analysis Software and Systems I, ed. D. W. Worrall, C. Biemesderfer, & J. Barnes, 297

Trager, S. C., Djorgovski, S., & King, I. R. 1993, in ASP Conf. Ser. 50, Structure and Dynamics of Globuler Clusters, ed. S. Djorgovski & G. Meylan, 347

Verbunt, F. & Meylan, G. 1988, A&A, 203, 297

van Teeseling, A., Beuermann, K., & Verbunt, F. 1996, A&A, 315, 467

Verbunt, F. & Johnston, H. M. 2000, A&A, 358, 910

Verbunt, F., Belloni, T., Johnston, H. M., van der Klis, M., & Lewin, W. H. G. 1994, A&A, 285, 903

Verbunt, F., Kuiper, L., Belloni, T., Johnston, H. M., de Bruyn, A. G., Hermsen, W., & van der Klis, M. 1996, A&A, 311, L9

Verbunt, F., Bunk, W. H., Ritter, H., & Pfeffermann, E. 1997, A&A, 327, 602

Weisskopf, M. C., O'Dell, S. L., & van Speybroeck, L. F. 1996, Proc. SPIE, 2805, 142

Chapter 3

Faint X-ray Sources in NGC 6440

This chapter is based on the original paper:

> "Observation of the Globular Cluster NGC 6440 and the Nature of Cluster X-ray Luminosity Functions," Pooley, D., Lewin, W. H. G., Verbunt, F., Homer, L., Margon, B., Gaensler, B. M., Kaspi, V. M., Miller, J. M., Fox, D. W., & van der Klis, M., 2002, *The Astrophysical Journal*, Vol. 573, p. 184,

with the permission of the publisher, *The Astrophysical Journal.*

3.1 Abstract

As part of our campaign to determine the nature of the various source populations of the low-luminosity globular cluster X-ray sources, we have obtained a *Chandra X-ray Observatory* ACIS-S3 image of the globular cluster NGC 6440. We detect 24 sources to a limiting luminosity of $\sim 2 \times 10^{31}$ ergs s^{-1} (0.5–2.5 keV) inside the cluster's half-mass radius, all of which lie within $\sim$2 core radii of the cluster center. We also find excess emission in and around the core which could be due to unresolved point sources. Based upon X-ray luminosities and colors, we conclude that there are 4–5 likely quiescent low-mass X-ray binaries and that most of the other sources are cataclysmic variables. We compare these results to *Chandra* results from other

globular clusters and find the X-ray luminosity functions differ among the clusters.

3.2 Introduction

NGC 6440 is a globular cluster near the center of our Galaxy, at a distance of 8.5 ± 0.4 kpc and reddened by $E_{B-V} = 1.07$ (Ortolani, Barbuy, & Bica, 1994). It is one of the twelve globular clusters in which a bright ($L_{\rm x} > 10^{36}$ ergs s^{-1}) X-ray source has been detected so far. The source in NGC 6440 is a transient, first detected during an outburst which lasted more than a month, in December 1971 and January 1972 (Markert et al., 1975; Forman, Jones, & Tananbaum, 1976). During the outburst, the 2–11 keV luminosity was more or less constant, at 3×10^{37} ergs s^{-1}. A second outburst was detected in August 1998. The observed luminosity was $< 10^{37}$ ergs s^{-1} (in 't Zand et al., 1999) at peak and dropped by a factor of 400 in less than 17 days (Verbunt et al., 2000). A third outburst was recently detected in August 2001 with the All Sky Monitor (ASM) on the *Rossi X-ray Timing Explorer* and announced by the ASM team[1]. A *Chandra* observation showed the luminosity to be 9×10^{35} ergs s^{-1} (in 't Zand et al., 2001). The difference in the properties of the outbursts raises the question whether they were indeed from the same source or different sources, and, if the former, how outbursts of the same source can be so different.

Comparison of optical images of NGC 6440 taken before and during the 1998 outburst show one star that was brighter in B, but not in R, during the outburst. This star, estimated at $B = 22.7$ and $(B - R)_0 < 0$ near the end of the outburst, is a viable optical counterpart to the X-ray transient (Verbunt et al., 2000).

Between outbursts, the core of NGC 6440 was detected by the *Einstein* and *ROSAT* satellites (Hertz & Grindlay, 1983; Johnston, Verbunt, & Hasinger, 1995). A longer *ROSAT* observation showed that the core contains (at least) two X-ray sources (Verbunt et al., 2000).

The high incidence of bright X-ray sources in globular clusters is likely explained by the formation of binaries containing a neutron star via tidal capture and/or exchange

[1]See http://xte.mit.edu.

Table 3.1: Globular Cluster Physical Parameters.

Cluster	ρ_0 ($L_\odot$ pc^{-3})	r_c	M_V
47 Tuc	4.77	23″	-9.42
NGC 6397	5.68	3″	-6.63
NGC 6440	5.28	7.″6	-8.75
NGC 6752	4.91	10.″5	-7.73

Central density, core radius, and integrated visual magnitude for four globular clusters. Values are from the catalog of Harris (1996) except for the core radii of 47 Tuc (Howell, Guhathakurta, & Gilliland, 2000), NGC 6440 (Trager, Djorgovski, & King, 1993), and NGC 6752 (Trager, Djorgovski, & King, 1993).

encounters. In a tidal capture, a neutron star passing close to another star transfers enough of its kinetic energy to the tidal bulge of the other star to keep it bound. In an exchange encounter, a neutron star takes the place of a binary member by expelling it (for a review of these processes, see Hut et al. 1992). To first order, both processes scale with the number of collisions in a cluster, i.e., with the product of the volume of the core (where most close encounters occur) and the square of the number density of stars in the core. NGC 6440 has one of the highest collision numbers, exceeding that of 47 Tuc, according to the best current values of cluster parameters (Table 3.1). In dense clusters like NGC 6440 and 47 Tuc, the formation of cataclysmic variables is also dominated by close encounters.

In this paper, we describe our observation of NGC 6440 with *Chandra*, aimed at discovering how many and what type of X-ray sources it contains and at finding out whether any of these corresponds to the star that is a possible counterpart for the 1998 transient. Similar results from *Chandra* have been reported for the other clusters 47 Tuc (Grindlay et al., 2001a), ω Cen (Rutledge et al., 2002), NGC 6397 (Grindlay et al., 2001b), and NGC 6752 (Pooley et al., 2002).

3.3 X-ray Observations and Analysis

NGC 6440 was observed for 23 ks on 2000 July 4 with the Advanced CCD Imaging Spectrometer (ACIS) on the *Chandra X-ray Observatory* with the telescope aimpoint

on the back-side illuminated S3 chip. The data were taken in timed-exposure mode with the standard integration time of 3.24 s per frame and telemetered to the ground in faint mode.

Data reduction was performed using the CIAO 2.1 software provided by the *Chandra* X-ray Center[2]. We used the CALDB 2.8 set of calibration files (gain maps, quantum efficiency, quantum efficiency uniformity, effective area). Bad pixels were excluded. Intervals of background flaring were searched for, but none were found.

Starting with the raw (level 1) event list, we processed the data (using the tool *acis_process_events*) without including the pixel randomization that is added during standard processing. This method slightly improves the point spread function (PSF). We then applied the good-time intervals supplied with the standard data products and filtered the data to include only events with *ASCA* grades of 0, 2, 3, 4, or 6 (this is the "standard" choice that generally optimizes the signal-to-background ratio; see the *Chandra* Proposer's Observatory Guide available from the website for more information). We also excluded software-flagged cosmic ray events. We used this filtered event list (level 2) for the subsequent analysis.

3.3.1 Source Detection

The wavelet-based *PWDetect* tool (Damiani et al., 1997) was employed for source detection in the 0.5–6.0 keV band. We found 24 point sources within the $28\farcs2$ cluster half-mass radius (Trager, Djorgovski, & King, 1993) and another 64 on the rest of the S3 chip. Table 3.2 lists the cluster sources. We have numbered the sources in order of detected counts in the 0.5–6.0 keV band. Our detection threshold was $\geq$3 counts ($\sim 10^{-15}$ ergs cm^{-2} s^{-1}). The density of sources outside the half-mass radius implies that 0.5 sources within the half-mass radius are not associated with the cluster. This is in agreement with the expected number of background sources from the $\log N - \log S$ relationships of Giacconi et al. (2001). All 24 possible cluster sources are consistent with being point sources, with the exception of CX9, which is inconsistent at $> 5\sigma$. It is likely a blend of multiple sources.

[2]See http://asc.harvard.edu.

Table 3.2: NGC 6440 X-ray Sources.

Src[a]	RA (J2000)[b]	Dec (J2000)[b]	Detected/Corrected Counts[c]			L_x (ergs s^{-1})[d]
			X_{soft}	X_{med}	X_{hard}	[0.5–2.5 keV]
CX1	17 48 52.163	−20 21 32.40	147/800	242/740	100/120	9.9×10^{32} (±13%)
CX2	17 48 53.181	−20 21 38.78	120/660	172/530	52/65	8.4×10^{32} (±19%)
CX3	17 48 52.419	−20 21 32.00	82/450	115/350	34/42	5.3×10^{32} (±14%)
CX4	17 48 53.320	−20 21 41.70	22/120	97/300	88/110	2.3×10^{32} (±14%)
CX5	17 48 52.874	−20 21 42.61	69/380	89/270	21/26	5.0×10^{32} (±15%)
CX6	17 48 52.852	−20 21 33.64	21/110	68/210	59/73	2.4×10^{32} (±30%)
CX7	17 48 52.625	−20 21 40.50	29/160	43/130	14/17	2.0×10^{32} (±21%)
CX8	17 48 51.987	−20 21 46.57	18/98	39/120	23/29	1.3×10^{32} (±20%)
CX9	17 48 52.939	−20 21 39.56	14/76	33/100	25/31	1.0×10^{32} (±20%)
CX10	17 48 52.874	−20 21 31.31	15/81	17/52	2/2	1.7×10^{32} (±25%)
CX11	17 48 52.888	−20 21 35.53	10/54	17/52	7/9	1.3×10^{32} (±27%)
CX12	17 48 53.123	−20 21 27.03	10/54	12/36	2/2	5.5×10^{31} (±39%)
CX13	17 48 51.870	−20 21 33.85	8/43	11/33	3/4	5.1×10^{31} (±40%)
CX14	17 48 52.537	−20 21 34.73	2/11	9/27	7/9	4.3×10^{31} (±45%)
CX15	17 48 52.310	−20 21 34.33	2/11	8/24	6/7	3.9×10^{31} (±47%)
CX16	17 48 52.734	−20 21 41.56	5/27	8/24	3/4	3.9×10^{31} (±47%)
CX17	17 48 52.676	−20 21 36.70	2/11	6/18	5/6	3.0×10^{31} (±54%)
CX18	17 48 52.581	−20 21 32.62	3/16	5/15	3/4	2.6×10^{31} (±60%)
CX19	17 48 52.712	−20 21 38.24	1/5	5/15	4/5	2.6×10^{31} (±60%)
CX20	17 48 52.896	−20 21 49.85	2/11	5/15	3/4	2.6×10^{31} (±60%)
CX21	17 48 53.210	−20 21 33.39	2/11	4/12	3/4	2.1×10^{31} (±67%)
CX22	17 48 53.225	−20 21 44.01	0/–	4/12	5/6	2.1×10^{31} (±67%)
CX23	17 48 52.083	−20 21 23.63	1/5	4/12	3/4	2.1×10^{31} (±67%)
CX24	17 48 52.427	−20 21 38.46	1/5	3/9	2/2	1.8×10^{31} (±78%)

[a] Sources are numbered according to their detected counts in the 0.5–6 keV band.
[b] Nominal *Chandra* positions from *PWDetect*. The pointing uncertainty is ∼0.6″.
[c] Corrections are described in §3.3.3. X-ray bands are 0.5–1.5 keV (X_{soft}), 0.5–4.5 keV (X_{med}), and 1.5–6.0 keV (X_{hard}).
[d] For sources CX1–CX11, L_x comes from an average of the unabsorbed luminosities of the best-fit models for each source. A linear relation between L_x and X_{med} counts for these sources was derived and used to estimate L_x for sources CX12–CX24 based upon their X_{med} counts. Uncertainties for CX1–CX11 come mainly from the spread in L_x from the three best-fit models; the distance and reddening uncertainties are negligible in comparison. For CX12–CX24, the uncertainties are a combination of the L_x-X_{med} fit uncertainty and the Poisson uncertainty for each source.

A $1\farcm4 \times 1\farcm4$ region centered on the core is shown in Fig. 3-1. The extraction regions for each source are shown, as are circles indicating the core radius (7″.58; Trager et al. 1993) and half-mass radius. We note that there is excess emission in and around the

Table 3.3: Radio Sources in and around NGC 6440.

Src[a]	VLA Position		*Chandra* Position		Offset
	RA (J2000)[b]	Dec (J2000)[c]	RA (J2000)[b]	Dec (J2000)[c]	After Shift[d]
A	46.345 ± 0.002	$21\ 36.12 \pm 0.02$	46.333 ± 0.021	$21\ 36.33 \pm 0.32$	$(-0\farcs11 \pm 0\farcs30,\ 0\farcs11 \pm 0\farcs32)$
B	47.985 ± 0.001	$19\ 59.28 \pm 0.01$	47.915 ± 0.053	$19\ 58.34 \pm 0.80$	$(0\farcs70 \pm 0\farcs74,\ 0\farcs84 \pm 0\farcs80)$
C	52.70 ± 0.02	$21\ 39.29 \pm 0.15$	52.625 ± 0.014	$21\ 40.50 \pm 0.22$	$(0\farcs70 \pm 0\farcs34,\ 1\farcs12 \pm 0\farcs27)$
			52.712 ± 0.019	$21\ 38.24 \pm 0.29$	$(-0\farcs07 \pm 0\farcs39,\ -1\farcs22 \pm 0\farcs33)$

[a] Src A corresponds to source 2 from Knapp et al. (1996) and src B to their source 3. Src C is PSR B1745−20; the first *Chandra* position listed for src C is CX7, and the second is CX19, neither of which is consistent with the pulsar's position (i.e., the offset is inconsistent with zero within errors).
[b] Seconds of time added to $17^{\rm h}48^{\rm m}$.
[c] Arcminutes and arcseconds subtracted from $-20°$.
[d] The shift is described in §3.3.2.

core. The residual count rate (i.e., the total rate minus the rate due to all *PWDetect* sources) in the 0.5–6 keV band inside a 15″ radius region in the center of the cluster is $(5.3 \pm 0.4) \times 10^{-4}$ cts pixel^{-1} ks^{-1}, which is a factor of 5.1 ± 0.6 higher than the rate from source-free regions outside the cluster. This emission is probably due to many unresolved point sources.

3.3.2 Astrometry

We have reanalyzed 1.5 GHz data from the Very Large Array (VLA; Napier, Thompson, & Ekers 1983) taken on 1990 April 20 at in A configuration and 1990 July 8 in BnA configuration. We detect three point sources in the region covered by the ACIS-S3 chip (Table 3.3); their positions are in agreement with the sources found by Knapp et al. (1996) and Fruchter & Goss (2000). The two sources outside the cluster both lie near *PWDetect* sources. The third source, PSR B1745−20, falls in between two X-ray sources (CX7 and CX19) in the core of NGC 6440.

Using the two sources outside the cluster to align the frames, we find that a small shift of $(0\farcs3,\ -0\farcs1)$ brings the X-ray and radio positions into agreement for both sources. However, PSR B1745−20 is still inconsistent with either X-ray source and is thus undetected in this *Chandra* observation. This is not surprising as its spin-down luminosity is 6.6×10^{32} ergs s^{-1} (Taylor, Manchester, & Lyne, 1993). This implies an X-ray luminosity $L_{\rm x} \approx 7 \times 10^{29}$ ergs s^{-1} (Verbunt et al., 1996), which is well below

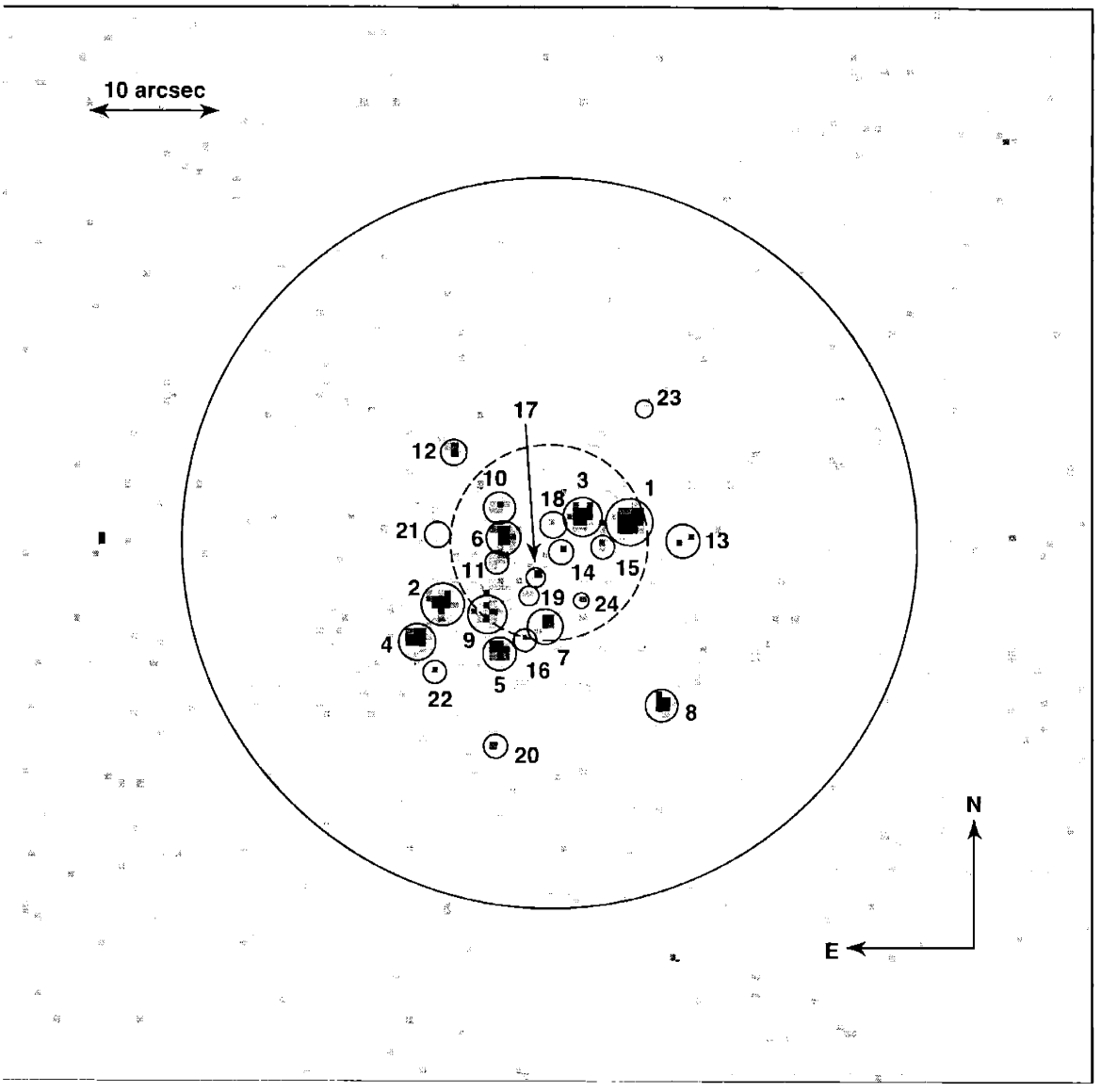

Figure 3-1: X-ray image of the central 1′.4 × 1′.4 region of NGC 6440. The numbered solid circles indicate the source extraction regions. The dashed circle represents the 7″.58 core radius, and the solid circle is the 28″.2 half-mass radius. Each pixel is a 0″.492 square.

our detection threshold of $\sim 2 \times 10^{31}$ ergs s^{-1}.

3.3.3 Count Rates

We extracted source counts in the following bands: 0.5–1.5 keV (X_{soft}), 0.5–4.5 keV (X_{med}), and 1.5–6.0 keV (X_{hard}). The detected count rate was corrected for background, exposure variations, and foreground photoelectric absorption. We make these

corrections in order to produce an X-ray color-magnitude diagram (CMD) that can be meaningfully compared to the X-ray CMDs that have resulted from *Chandra* observations of other globular clusters. In addition, however, attention must be given to differences in detector responses and, of course, exposure times.

The background count rate in each band was estimated from an annulus around the core sources. The inner radius was 31 pixels, and the outer radius was 64 pixels. No detected sources were present within the annulus. The density of background counts in each band (for 23 ksec) was found to be 0.006 counts per pixel (X_{soft}), 0.011 counts per pixel (X_{med}), and 0.007 counts per pixel (X_{hard}). The background count rate in the core may be somewhat higher, but even factors of a few greater than this estimate have negligible effects on our analysis.

To account for the $\sim$1% variations in exposure among the sources, we applied multiplicative corrections based on the ratio of a source's average effective area in each of the three bands to the average effective area in the same band of CX12, which had the highest average exposure. The individual effective area curves for the sources were made using the CIAO tool *mkarf*. The average effective area of CX12 in each of the bands was 580 cm^{-2} (X_{soft}), 455 cm^{-2} (X_{med}), and 368 cm^{-2} (X_{hard}).

While the previous corrections were relatively minor (at the few percent level or less), the correction for photoelectric absorption is rather large for NGC 6440. The conversion of optical reddening to column density (Predehl & Schmitt, 1995) gives a value of $N_H = 5.9 \times 10^{21}$ cm^{-2}. We investigated the effects of such an absorption on three characteristic spectra: a 3 keV thermal bremsstrahlung, a 0.3 keV blackbody plus power law with photon index of $\Gamma = 2$, and a power law with a photon index of $\Gamma = 2$. The effects were most dramatically seen in the X_{soft} band, where the absorbed count rate was a factor of 4.8–6.1 lower than the unabsorbed one (depending on the spectrum). Averaging the results of each spectrum in each band, we use the following correction factors: 5.43 (X_{soft}), 3.06 (X_{med}), and 1.24 (X_{hard}). Table 3.2 lists both the observed and fully corrected counts in each band. The effect of the absorption correction on the X-ray color-magnitude diagram (Fig. 3-2) is a uniform shift of all points 0.48 units on the left axis and 0.64 units on the bottom axis. The top and

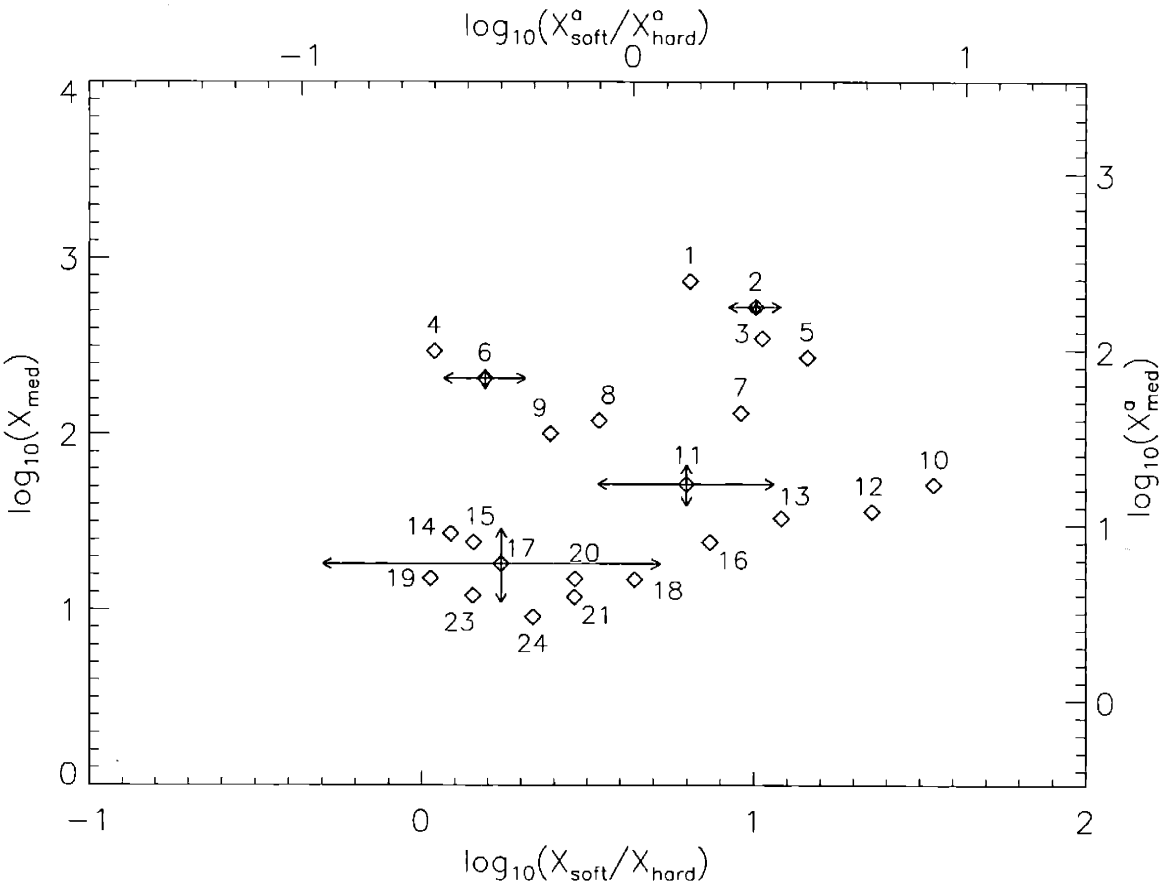

Figure 3-2: X-ray color-magnitude diagram. The X-ray color is defined as the logarithm of the ratio of X_{soft} (0.5–1.5 keV) corrected counts to X_{hard} (1.5–6.0 keV) corrected counts, and the magnitude is the logarithm of X_{med} (0.5–4.5 keV) corrected counts. For the sake of clarity, only a few error bars are shown; they represent the 1σ error estimates given by Gehrels (1986). Our correction for photoelectric absorption has the effect of uniformly shifting the data +0.48 units on the left axis and +0.64 units on the bottom axis. The top and right axes provide the absorbed color and magnitude scales (^{a}), i.e., the observed colors and magnitudes uncorrected for absorption. CX22 is not shown since it has 0 counts in X_{soft}.

right axes give the X-ray color and magnitude without this shift (they do, however, include the small corrections for background subtraction and exposure variations).

3.3.4 Spectral Fitting

We used the CIAO tool *dmextract* to extract spectra of sources CX1–CX11 in the 0.3–8 keV range. Because even the brightest source (CX1) had relatively few counts, we chose to fit the unbinned spectra using the C-statistic in XSPEC (Arnaud, 1996).

This statistic is insensitive to the number of counts per bin and is thus a good choice when fitting low-count data. It should be noted, however, that the C-statistic is only applicable when the background is negligible, which is the case with these data. To determine the goodness of the fits, we ran Monte Carlo simulations of each best-fit spectrum for each source and compared with the observed spectra. For a good fit, the simulations should give lower values of the fit statistic than the data give about 50% of the time.

Three different models were fit: thermal bremsstrahlung (TB), blackbody plus power-law (BB+PL), and power law (PL). We fixed $N_{\rm H}$ to the value from optical reddening. As expected for such low-count spectra, very few fits could be formally ruled out. We estimated the unabsorbed source luminosities for CX1–CX11 by averaging the results from the three best-fit models for each source. The spread in $L_{\rm x}$ of the three models was $\sim$20% for each source. Fitting a linear relation to these luminosities versus detected $\rm X_{med}$ counts, we have estimated the unabsorbed luminosities for sources CX12–CX24 based on their $\rm X_{med}$ counts. These are listed in Table 3.2.

Fitting a hydrogen atmosphere spectral model to the securely identified quiescent neutron star CX1, in 't Zand et al. (2001) find an X-ray luminosity of 1.7×10^{33} ergs s^{-1} in the 0.5–7 keV range. In the 0.5–2.5 keV band, the hydrogen atmosphere model gives $L_{\rm x} = 1.5 \times 10^{33}$ ergs s^{-1}, which is $\sim$50% more than our estimate. However, the results are consistent with each other within errors.

3.4 Results and Discussion

As shown in Fig. 3-1, the sources detected by *Chandra* are concentrated towards the center of NGC 6440, and all lie well within the half-mass radius of the cluster. This and the estimate that we expect only $\sim$0.5 background sources in this region suggests that all sources are cluster members. Because of the large distance and high reddening to NGC 6440, there is little suitably deep optical imaging available. In the absence of optical identifications – with one notable exception discussed below – we try to classify the sources on the basis of their X-ray properties.

In the Galactic disk, cataclysmic variables are known to have X-ray luminosities up to $\sim 10^{32}$ ergs s^{-1} in the 0.5–2.5 keV range (see e.g. Fig. 8 in Verbunt et al. 1997; the single outlier in that figure is the DQ Her type system V1223 Sgr at $L_{\rm x} \simeq 4\times10^{32}$ ergs s^{-1}). Low mass X-ray binaries (LMXBs) in the Galactic disk reach higher luminosities, even in quiescence, and have X-ray spectra that are soft (blackbody color temperatures of $\sim$0.3 keV). The faintest known quiescent LMXB (qLMXB) with a neutron star has $L_{\rm x} \simeq 7 \times 10^{31}$ ergs s^{-1} (Cen X-4; Campana et al. 1997), but binaries with a black hole may reach lower X-ray luminosities (e.g., A0620−00 dropped to $\sim 10^{30}$ ergs s^{-1}, McClintock, Horne, & Remillard 1995). RS CVn systems in the Galactic disk reach luminosities in the range of the sources detected with *Chandra* in NGC 6440. However, the brightest *Chandra* sources optically identified with RS CVn systems (in the wide definition which includes BY Dra binaries) in globular clusters have $L_{\rm x} \simeq 3, 2, 0.3 \times 10^{31}$ ergs s^{-1} in 47 Tuc, NGC 6397, and NGC 6752, respectively (Grindlay et al., 2001a,b; Pooley et al., 2002).

Bringing this information to bear on the sources in NGC 6440, we conclude that CX1, CX2, CX3, and CX5 are qLMXBs, that CX4, CX6, and CX7 could be either qLMXBs or cataclysmic variables, and that most other sources that we have detected are cataclysmic variables. This is further clarified by comparing Fig. 3-2 to the X-ray CMDs of 47 Tuc, NGC 6397, and NGC 6752 (Grindlay et al., 2001a,b; Pooley et al., 2002). The X-ray colors of CX1, CX2, CX3, CX5, and CX7 are all $\sim$1, as is the X-ray color of the probable qLMXB in NGC 6397 (its listed X-ray color of $\sim$2.6 includes multiplication by a factor of 2.5 which Grindlay et al. use to define their X-ray colors and magnitudes). The two probable qLMXBs in 47 Tuc have X-ray colors of $\sim$0.6 (again, without the factor of 2.5). In contrast, the brightest CVs in 47 Tuc, NGC 6397, and NGC 6752 all have X-ray colors of $\sim$0, and the vast majority of identified CVs in these three clusters have X-ray colors in the range -0.5 to 0.5, suggesting that CX7 is a qLMXB and that CX4 and CX6 are CVs. Because of their relatively soft X-ray colors, CX10, CX12, and CX13 might be quiescent transients with a black hole, but they are more likely cataclysmic variables.

Some of the faintest sources that we detected may be RS CVn systems or mil-

lisecond pulsars, which have X-ray luminosities in this range (see Fig. 8 in Verbunt et al. 1997).

CX1 coincides within the positional error with the optical variable V2, the suggested counterpart for the transient in NGC 6440 that went into a short faint outburst in August 1998 (Verbunt et al., 2000). Since CX1 shows the X-ray characteristics of a transient in quiescence, and V2 the optical characteristics (magnitude and color) of such a source in outburst, we consider the identification secure. The transient showed X-ray bursts (in 't Zand et al., 1999, 2001), indicating that the accretor in CX1 is a neutron star. This association of CX1 and V2 confirms the suggested optical identification (Verbunt et al., 2000) of this first qLMXB to be identified in outburst.

Based on the secure CX1/V2 identification, we shift the optical frame of Verbunt et al. (2000) into the *Chandra* frame of this observation. After this small ($\sim$0.″37) shift, we find that CX24 is coincident to $\sim$0.″1 with star V0 of Verbunt et al. (2000), a suggested Mira type variable. Since Mira's are cool giants, they are not expected to be X-ray sources. Remarkably, Belloni, Verbunt, & Mathieu (1998) tentatively identify an X-ray source in the old open cluster M67 with an X-ray luminosity very similar to that of CX24 with a star near the tip of the giant branch (X19/S364 in their Table 3). We therefore do not discard offhand the possible identification of CX24 with V0.

The number of close encounters in a globular cluster scales with ${\rho_o}^2 {r_c}^3$, where ρ_o is the central density of the cluster and r_c its core radius. The number of low-mass X-ray binaries, and the number of cataclysmic variables are both thought to scale with the number of close encounters in clusters with dense cores like 47 Tuc and NGC 6440. This implies that the numbers of these sources in NGC 6440 should be $\sim$1.7 times that in 47 Tuc. Two of the 20 X-ray sources in 47 Tuc with $L_x > 10^{31}$ erg s^{-1} are probably qLMXBs, 17 of the other sources are cataclysmic variables, and one is a BY Dra system. The number of 4 or 5 qLMXBs in NGC 6440 is compatible with this prediction, but the number of 19 or 18 cataclysmic variables in the same luminosity range is somewhat lower than predicted. However, the excess flux above background (see §3.3.1) in and around the core corresponds to a luminosity of $\sim 5 \times 10^{32}$ ergs s^{-1},

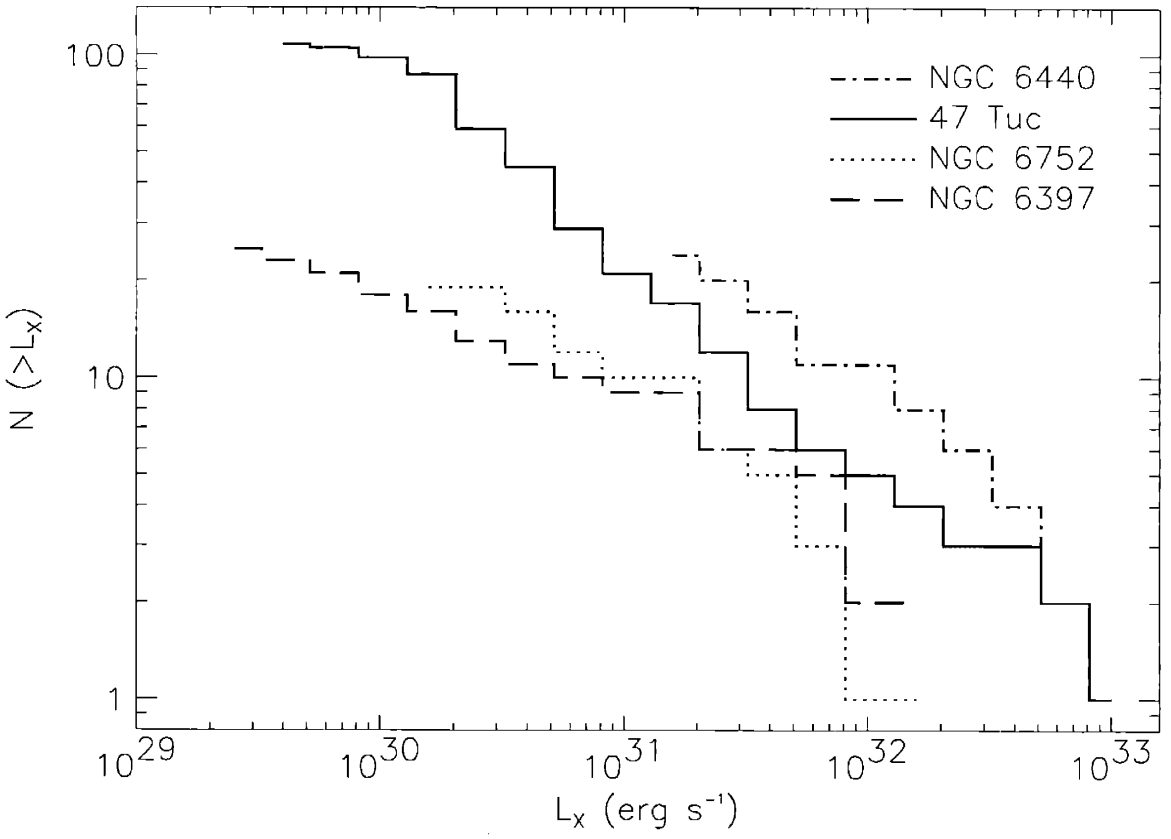

Figure 3-3: Histogram of the number of *Chandra* sources detected above a certain L_x ($N(>L_x)$) versus L_x [0.5–2.5 keV] for four globular clusters.

and has a corrected X-ray color of 0.5. This emission could be due to unresolved point sources.

At the same time, destruction of close binaries by multiple close encounters depresses the numbers of X-ray sources in the densest clusters, according to theory. From a study of the *ROSAT* data, Johnston & Verbunt (1996) found that the number of faint sources actually scales with $\rho_o{}^{1.5} r_c{}^3$, not $\rho_o{}^2 r_c{}^3$, which appears to confirm this prediction. As *Chandra* data of more clusters become available, it will be interesting to verify this in more detail; the possible relatively low number of X-ray sources in NGC 6440 may be a first hint. However, given the uncertainty in the collision numbers and the possibility of many unresolved sources, we refrain from drawing premature conclusions.

From the *ROSAT* data, Johnston & Verbunt (1996) also derive a power-law luminosity function $dN \propto L_x^{-\gamma} d\ln L_x$ with $\gamma = 0.5$. The *Chandra* observations have

Table 3.4: X-ray Luminosity Functions for Four Clusters Observed with *Chandra*.

Cluster	r_s	L_{max}	A	B	C	ρ_0	γ	K-S Prob.	Ref.
47 Tuc	86″	33.0	5	15	74	4.77	$0.78^{+0.16}_{-0.17}$	99.8%	1
NGC 6397	119″	32.3	5	8	12	5.68	$0.29^{+0.11}_{-0.08}$	99.3%	2
NGC 6440	16″	33.0	9	14		5.28	$0.51^{+0.19}_{-0.14}$	96.7%	3
NGC 6752	109″	32.3	7	12		4.91	$0.50^{+0.21}_{-0.15}$	98.8%	4

The source with the largest distance to the cluster center provides a measure of the surveyed area. For each cluster, we give this distance r_s, the (logarithm of the) X-ray luminosity L_{max} (in ergs s^{-1}) of the brightest source detected, and the numbers of sources with (A) $0.1 < L_x/L_{max} \leq 1.0$, with (B) $0.01 < L_x/L_{max} \leq 0.1$, and (where possible) with (C) $0.001 < L_x/L_{max} \leq 0.01$. We list the logarithm of the central luminosity density ρ_0 (in $L_\odot$ pc^{-3}) as given by Harris (1996). We also give the index of the best-fit luminosity function ($dN/dL_x \propto {L_x}^{-(\gamma+1)}$) and the Kolmogorov-Smirnov probability of the fit for the data in Fig. 3-3.

References — 1. Grindlay et al. (2001a), 2. Grindlay et al. (2001b), 3. (this work), 4. Pooley et al. (2002)

resolved several *ROSAT* sources into multiple sources and have also detected sources with lower luminosities. As a result, the number of faint sources is already larger in the few clusters observed with *Chandra* than in the complete *ROSAT* data set described by Verbunt (2001). We plot the cumulative luminosity functions of four clusters observed with *Chandra* in Fig. 3-3. Following the statistical method of Johnston & Verbunt (1996), we derive the best-fit luminosity function by forming the quantities $z^j = (L_i^j/L_i)^{-\gamma}$ and finding the γ that most uniformly distributes the z^j along the segment [0,1]. Here, L_i is the limiting L_x to which cluster i has been searched, and L_i^j is the L_x of source j in cluster i. In order to reduce errors in the analysis due to incompleteness of the sample at the low end of the luminosity range, we have taken each L_i to be $\sim$3 times the L_x of the faintest observed source in each cluster and have restricted the data accordingly. We examined the uniformity of the z^j distribution for a range of γ through Kolmogorov-Smirnov tests. The results of these tests are shown in Fig. 3-4. The best-fit γ and the corresponding probabilities of the fits are given in Table 3.4.

To further investigate the luminosity functions, we collect in Table 3.4 the numbers of faint sources detected with Chandra in four clusters, as a function of their

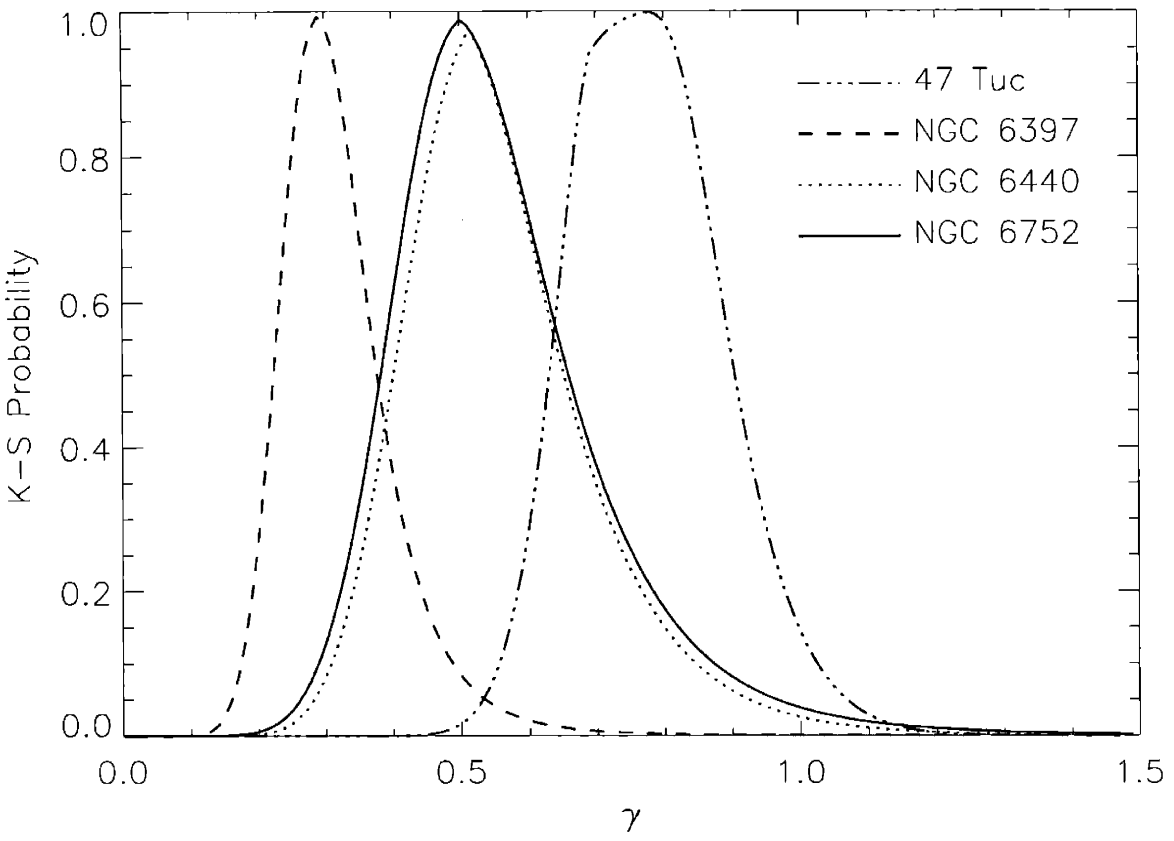

Figure 3-4: The Kolmogorov-Smirnov probability, as a function of γ, that the $z^j = (L_i^j/L_i)^{-\gamma}$ are uniformly distributed. L_i is the limiting L_x to which cluster i has been observed, L_i^j is the L_x of source j in cluster i, and γ is the index of the luminosity function $dN \propto L_x^{-\gamma}\, d\log L_x$.

luminosity. The surveyed area in each cluster is well within the half-mass radius, and most sources are expected to be associated with the clusters. According to the Johnston-Verbunt result, the number of sources in a logarithmic bin, corresponding to one decade of luminosities, increases by a factor $\sqrt{10}$ between adjacent bins. Table 3.4 shows that the current data tend to a somewhat slower increase towards lower luminosities in three of the four clusters. This trend is especially significant in NGC 6397, in marked contrast to the cluster 47 Tuc in which the increase towards lower luminosities is slightly faster than a factor 10 over two bins. In Table 3.4 we note an anticorrelation between the slope of the luminosity function and the central cluster density. We investigate two possible explanations. First, in the densest clusters, mass segregation may enhance the neutron-star capture rate (e.g., Verbunt & Meylan 1988) and thus enhance the more luminous population of qLMXBs. The

numbers of such sources, however, are too small in the clusters observed to strongly affect the luminosity function. Indeed, the numbers in Table 3.4 show that the difference between NGC 6397 and 47 Tuc, the most and least dense clusters, lies mainly in the low-luminosity sources, i.e., presumably the RS CVn and CV systems. This difference may be due to the destruction of RS CVns and CVs (or CV progenitors) in the densest clusters by encounters with neutron stars. Observations of a larger number of clusters may help in confirming the variation in luminosity function among globular clusters and in explaining it as a function of the initial cluster properties. *Chandra* observations combined with simulations with the GRAPE-6 (Makino, 2001) could be instrumental in understanding the dynamical evolution of globular clusters.

Bibliography

Arnaud, K. A. 1996, in ASP Conf. Ser. 101, Astronomical Data Analysis Software and Systems V, ed. G. Jacoby & J. Barnes, 17

Belloni, T., Verbunt, F., & Mathieu, R. D. 1998, A&A, 339, 431

Campana, S., Mereghetti, S., Stella, L., & Colpi, M. 1997, A&A, 324, 941

Damiani, F., Maggio, A., Micela, G., & Sciortino, S. 1997, ApJ, 483, 350

Forman, W., Jones, C., & Tananbaum, H. 1976, ApJ, 207, L25

Fruchter, A. S., & Goss, W. M. 2000, ApJ, 536, 865

Gehrels, N. 1986, ApJ, 303, 336

Giacconi, R., Rosati, P., Tozzi, P., Nonino, M., Hasinger, G., Norman, C., Bergeron, J., Borgani, S., Gilli, R., Gilmozzi, R., Zheng, W. 2001, ApJ, 551, 624

Grindlay, J. E., Heinke, C., Edmonds, P. D., & Murray, S. S. 2001, Science, 292, 2290

Grindlay, J. E., Heinke, C. O., Edmonds, P. D., Murray, S. S., & Cool, A. M. 2001, ApJ, 563, L53

Harris, W. E. 1996, AJ, 112, 1487

Hertz, P. & Grindlay, J. E. 1983a, ApJ, 267, L83

Howell, J. N., Guhathakurta, P., & Gilliand, R. L. 2000, PASP, 112, 1200

Hut, P., McMillan, S., Goodman, J., Mateo, M., Phinney, E. S., Pryor, C., Richer, H. B., Verbunt, F., & Weinberg, M. 1992, PASP, 104, 981

in 't Zand, J. J. M., Verbunt, F., Strohmayer, T. E., Bazzano, A., Cocchi, M., Heise,

J., van Kerkwijk, M. H., Muller, J. M., Natalucci, L., Smith, M. J. S., & Ubertini, P. 1999, A&A, 345, 100

in 't Zand, J. J. M., van Kerkwijk, M. H., Pooley, D., Verbunt, F., Lewin, W. H. G., & Wijnands, R. 2001, ApJ, in press

Johnston, H. M., Verbunt, F., & Hasinger, G. 1995, A&A, 298, L21

Johnston, H. M. & Verbunt, F. 1996, A&A, 312, 80

Knapp, G. R., Gunn, J. E., Bowers, P. F., & Vasquez Porítz, J. F. 1996, ApJ, 462, 231

Makino, J. 2001, in ASP Conf. Ser. 228, Dynamics of Star Clusters and the Milky Way, ed. S. Deiters, B. Fuches, A. Just, R. Spurzem, & R. Wielen

Manchester, R. N., Lyne, Johnston, S., D'Amico, N., Lim, J., Kniffen, D. A., Fruchter, A. S., & Goss W. M. 1989, IAU Circ., 4905, 2

Markert, T. H., Backman, D. E., Canizares, C. R., Clark, G. W., Levine, A. M. 1975, Nature, 257, 32

McClintock, J. E., Horne, K., & Remillard, R. A. 1995, ApJ, 442, 358

Napier, P. J., Thompson, A. R., & Ekers, R. D. 1983, IEEE, 71, 1295

Ortolani, S., Barbuy, B., & Bica, E. 1994, A&A Supp., 108, 653

Pooley, D., Lewin, W. H. G., Homer, L., Verbunt, F., Anderson, S. F., Gaensler, B. M., Margon, B., Miller, J. M., Fox, D. W., Kaspi, V. M., & van der Klis, M. 2002, ApJ, 569, 405

Predehl, P., & Schmitt, J. H. M. M. 1995, A&A, 293, 889

Rutledge, R. E., Bildsten, L., Brown, E. F., Pavlov, G. G., & Zavlin, V. E. 2002, ApJ, 578, 405

Taylor, J. H., Manchester, R. N., & Lyne, A. G. 1993, ApJS, 88, 529

Trager, S. C., Djorgovski, S., & King, I. R. 1993, in ASP Conf. Ser. 50, Structure and Dynamics of Globuler Clusters, ed. S. Djorgovski & G. Meylan, 347

Verbunt, F., & Meylan, G. 1988, A&A, 203, 297

Verbunt, F., Kuiper, L., Belloni, T., Johnston, H. M., de Bruyn, A. G., Hermsen, W., & van der Klis, M. 1996, A&A, 311, L9

Verbunt, F., Bunk, W. H., Ritter, H., & Pfeffermann, E. 1997, A&A, 327, 602

Verbunt, F., van Kerkwijk, M. H., in 't Zand, J. J. M., & Heise, J. 2000, A&A, 359, 960

Verbunt, F. 2001, A&A, 368, 137

Chapter 4

Conclusions

4.1 The Impact of This Work

The observations and analyses presented in this part of the thesis have shown the tremendous gains made by *Chandra* observations of globular clusters. This work has demonstrated the efficiency and effectiveness of finding close binaries in globular clusters by using high spatial resolution X-ray imaging. These data can then be compared to high spatial resolution optical and radio images to identify the natures of the sources found. This technique has so far found hundreds of close binaries in about a dozen clusters, with roughly 70 sources classified so far (Table 4.1) and much work still in progress. This is a significant advancement over previous X-ray imaging satellites; *ROSAT* discovered 57 sources (Verbunt, 2001), but, because the spatial resolution was not as high as *Chandra*'s, only two of those sources had been securely classified (Hakala et al., 1997; Margon, Downes, & Gunn, 1981; Lyne et al., 1987; Saito et al., 1997). Furthermore, the combination of *Chandra* and *HST* is substantially better than what *HST* has been able to do on its own, as discussed in §1.3.

In addition to discovery of sources, this thesis has reported much analysis based on those discoveries. A number of satisfying results have been found, and some new and interesting questions have been raised. The large numbers of CVs expected to reside in globular clusters are finally being found, although the ratios of the numbers

of CVs to other X-ray sources has raised some questions. In 47 Tuc and NGC 6397, the ratio of CVs to qLMXBs is remarkably similar despite a difference of two orders of magnitude in their collision frequencies. This is rather curious considering that this ratio depends on a number of factors that should vary greatly from cluster to cluster, such as the retention rate of neutron stars, the mass segregation of the cluster, the central density, and the size of the core. In addition, the ratio of the number of CVs to the number of X-ray active main sequence binaries is similar in 47 Tuc, ω Cen, NGC 6397, and NGC 6752. This is also rather odd since these two types of objects should have very different formation channels. Another main result of this work is that the X-ray luminosity functions are shown to vary from cluster to cluster in a way that is plausibly understood from the current picture of cluster internal dynamics. Globular clusters with denser cores have flatter luminosity functions than clusters with less dense cores. In other words, there are more bright sources and fewer dim sources in clusters with denser cores, which can be explained by two separate effects. At the bright end of the luminosity function, mass segregation in dense clusters may enhance the neutron star capture rate and thus enhance the more luminous population of quiescent LMXBs, while, at the dim end, the RS CVns and CVs may be destroyed by encounters with neutron stars.

4.2 Progressing Further

The X-ray study of globular clusters seems to be entering a "golden age." The unprecedented angular resolution of *Chandra* has ushered in a revolution in our ability to scrutinize the inner workings of globular clusters. It is important to realize, however, that this will be as good as it will get for the next two decades to come. None of the near-future X-ray missions currently in planning will improve on *Chandra*'s angular resolution. *Constellation X* (expected launch around 2010) has a goal of 15″, and the *X-ray Evolving UniverSe mission* (expected launch around 2015) is hoping for 2″. Not until the possible launch of *Generation X* in 2020 will there be an X-ray satellite with better angular resolution (*Generation X* is aiming for 0.″1). Clearly,

there is need to maximize the available time with *Chandra*, and I will now outline a few ways to go about this.

4.2.1 Differences in Globular Cluster Central Concentration, Size, and Mass

To confirm and begin to understand the results presented in this work concerning the luminosity functions and number ratios of the various constituents of the low-luminosity globular cluster X-ray population, more globular clusters which span a range of physical parameters need to be studied. My advisor Walter Lewin and I have developed a coherent plan for a uniform study of globular clusters. We devised a campaign to observe globular clusters with *Chandra* and *Hubble* (using archival data when available) which differ greatly in their physical properties such as central concentration, cluster size, and mass. Ultimately, we plan to methodically build up a large knowledge base of observational data with which we can make statistically meaningful statements about the relationships between a globular cluster's physical properties and its confirmed close binary population. Our proposals based on this plan have been extremely successful (Table 4.1), and there is now a wealth of data to carry our plan forward.

We will gain further insight into globular cluster evolution by comparing our observational results with the results of detailed N-body (with N up to 10^6) calculations being done by members of our collaboration on GRAPE-6 supercomputers, the fastest computers in the world (Portegies Zwart et al., 2001). These simulations will include a full stellar evolution treatment of all stars and recipes for binary stellar evolution. They will cover the full 10^{10} years of a globular cluster's history, yet still resolve all individual encounters between singles, binaries and triples (Portegies Zwart et al., 2001). These will be the first ever realistic globular cluster simulations, tailored to individual clusters.

Table 4.1: Current and Future Deep *Chandra* Observations of Globular Clusters

Globular Cluster	Sources Discovered	Sources Classified	*Chandra* Cycle	PI	Archival *Hubble* Data?	Ref.
47 Tuc	108	36	1, 3	Murray, Grindlay	Y	Grindlay et al. (2001a)
NGC 288	—	—	4	Lewin	Y	—
ω Cen*	30–40	5	1	Cool	Y	Cool (2002)
NGC 5904*	13	0†	3	Lewin	Y‡	Pooley et al. (2002d)
NGC 6093*	?	?	2	Murray	Y	—
NGC 6121*	25	0†	1	Lewin	Y‡	Pooley et al. (2002c)
NGC 6266*	35	0†	3	Lewin	Y	Pooley et al. (2002d)
NGC 6341	—	—	4	Lewin	Y	—
NGC 6366*	3	0†	3	Lewin	N	Pooley et al. (2002d)
NGC 6397	20–25	15	1, 3	Murray, Grindlay	Y	Grindlay et al. (2001b)
NGC 6440	23–24	4–5	1, 4	Lewin, Wijnands	N	Pooley et al. (2002b)
NGC 6541	—	—	4	Lewin	Y	—
NGC 6752	15–20	15	1	Lewin	Y	Pooley et al. (2002a) D'Amico et al. (2002)
NGC 7099*	4	0	3	Cohn	Y	Cohn et al. (2002),

* These results have not yet appeared in the literature.
† Work in progess.
‡ Some data exist, but more are needed.
Observations of clusters in *italics* have not yet occured.

4.2.2 Differences in Globular Cluster Age

Most astronomical evolutionary studies have the advantage of studying different epochs by merely looking around in the sky for objects of different ages. Not so with our globular cluster research since the vast majority of the ~150 Galactic globular clusters formed at very nearly the same time. In fact, this is one of the main reasons for our ignorance about globular cluster evolution.

However, it has been suggested that certain dense, massive clusters are, in fact, young globular clusters Mateo (1993). Although no such clusters have been found in the Milky Way (our Galaxy hasn't produced such clusters in over 9 Gyr), there are many such young massive clusters in the neighboring Large Magellanic Cloud (LMC). Observing these with *Chandra* would give us the first picture of the early X-ray binary

population of massive clusters and would test one of the strong predictions of current theory and simulations, namely, that these clusters should be unusually rich in black hole X-ray binaries Portegies Zwart (2002).

According to preliminary calculations, a small number of black holes are retained by a massive cluster after the supernovae explosions in which they are born. After about 100 Myr, the black holes are by far the most massive objects in the cluster, and they sink to the core (mass segregation) where they pair off in binaries. Through super-elastic collisions with other cluster members, the black holes are ultimately ejected from the cluster. After about a billion years, the cluster has lost all its black holes. It is therefore not surprising that no black hole X-ray binaries have been found in Galactic globular clusters. (It should be noted that the neutron stars in Galactic globulars are in the process of following the same route but have not yet reached the point of being completely expelled.)

Along with Simon Portegies Zwart, I have written a successful proposal that was granted time to observe the two LMC clusters NGC 1850A and NGC 1850B with *Chandra* (both have archival *Hubble* data). This pair comprises a globular-like 70 Myr old cluster and a more loosely distributed 5 Myr old cluster . We will propose for observations of more clusters in the future *Chandra* and *Hubble* cycles.

In addition to these young massive clusters, there is a class of true globulars in our own Galaxy that deserves special attention. Nine globular clusters in the Milky Way have been found to be over 3 Gyr younger than the rest van den Bergh (1998). In the next *Chandra* round, I will propose a survey of the most suitable of these clusters for X-ray observation (based on central concentration, mass, distance, and line-of-sight absorption) since none have yet been observed. I will use *Hubble* archival data where available and propose for new observations if necessary. These data would be the first to give a picture of the X-ray source population of Galactic globular clusters at a different age. It is unknown how a 3 Gyr younger population of close binaries would differ from the one we are observing in the oldest globulars, but numerical simulations indicate that the younger population might contain a greater number of neutron star binaries. Old globulars in the Galaxy are in the process of expelling their

neutron stars Portegies Zwart (2002) for the reasons stated above. Therefore, younger globular clusters should contain more neutron stars because they have not yet expelled as many. As with all of the proposed observations mentioned in this proposal, these observations could also be directly compared to GRAPE-6 simulations to broaden and test our understanding of globular cluster evolution.

4.2.3 Differences in Parent Galaxy

I will also propose to systematically study the old globular clusters of the LMC and SMC with *Chandra* and *Hubble* for direct comparison with our knowledge base of Milky Way globulars. Here, the important test is the effect of the environment of the parent galaxy. For example, recent simulations have shown that tightly bound star clusters near the center of the Milky Way are stripped of a sizeable fraction of their stellar members due to the gravitational tidal field Portegies Zwart et al. (2002). The same could happen with less tightly bound globular clusters that are further away, which would result in a significant decrease in the number of primordial binaries that remain in the cluster throughout its evolution. The effects of this on the present population of binaries are unknown, but, since many close binaries are formed from exchange encounters with primordial binaries, this could significantly alter the cluster's evolution. Unlike the Galactic globulars, the LMC and SMC clusters are relatively unaffected by the tidal field of their parent galaxies. Thus, they may harbor significantly more close binaries, and therefore more X-ray sources, than their Galactic counterparts.

None of the LMC or SMC old globular clusters has yet been observed with *Chandra*, and this would be the first systematic X-ray survey of such objects. Combined with the systematic study of the X-ray source populations of the Galactic globulars in which I am currently involved, this work would directly examine the role of the parent galaxy in gobular cluster evolution.

Bibliography

Cohn, H. N., Lugger, P. M., Grindlay, J. E., Edmonds, P. D., Heinke, C. O., Rubenstein, E. P., Cool, A. M. 2002, AAS Mtg 200, 10.02

Cool, A., 2002, APS/HEAD Conf., G1.002

D'Amico, N., Possenti, A., Fici, L., Manchester, R. N., Lyne, A. G., Camilo, F., & Sarkissian, J. 2002, ApJ, 570, L89

Grindlay, J. E., Heinke, C., Edmonds, P. D., & Murray, S. S. 2001, Science, 292, 2290

Grindlay, J. E., Heinke, C. O., Edmonds, P. D., Murray, S. S., & Cool, A. M. 2001, ApJ, 563, L53

Hakala, P. J., Charles, P. A., Johnston, H. M., & Verbunt, F. 1997, MNRAS, 285, 693

Lyne, A. G., Brinklow, A., Middleditch, J., Kulkarni, S. R., & Backer, D. C. 1987, Nature, 328, 399

Margon, B., Downes, R. A., & Gunn, J. E. 1981, ApJ, 247, L89

Mateo, M., 1993, in *The Globular Cluster—Galaxy Connection*, eds. G. H. Smith and J. P. Brodie (ASP, San Francisco), p. 387

Pooley, D., Lewin, W. H. G., Homer, L., Verbunt, F., Anderson, S. F., Gaensler, B. M., Margon, B., Miller, J. M., Fox, D. W., Kaspi, V. M., & van der Klis, M. 2002a, ApJ, 569, 405

Pooley, D., Lewin, W. H. G., Verbunt, F., Homer, L., Margon, B., Gaensler, B. M., Kaspi, V. M., Miller, J. M., Fox, D. W., & van der Klis, M. 2002b, ApJ, 573, 184

Pooley, D., Lewin, W. H. G., Verbunt, F., Homer, L., Anderson, S. F., Gaensler, B. M., Margon, B., Miller, J. M., Fox, D. W., Kaspi, V. M. 2002c, APS/HEAD Conf., 17.065

Pooley, D., et al., 2002d, in preparation

Portegies Zwart, S. F. McMillan, S. L. W., Hut, P., Makino, J. 2001, MNRAS, 321, 199

Portegies Zwart, S., 2002, priv. comm.

Portegies Zwart, S., Makino, J., McMillan, S. L. W., Hut, P. 2002, ApJ, 565, 265

Saito, Y., Kawai, N., Kamae, T., Shibata, S., Dotani, T., & Kulkarni, S. R. 1997, ApJ, 477, L37.

van den Bergh, S., 1998, ApJ, 495, L79

Verbunt, F. 2001, A&A, 368, 137

Part II

X-ray Studies of Core-collapse Supernovae

Chapter 5

Introduction

5.1 What Are Core-collapse Supernovae?

Perhaps the first question to address is, what is a star? A star is a self-gravitating, radiating sphere of gas. It maintains its figure by balancing the gravitational tendancy to collapse by the outward pressure of radiation. The fuel for this radiation comes from nuclear burning deep in the interior of the star; lighter elements are fused into heavier elements, and energy is released in the form of radiation. This is an energetically favorable situation so long as there is a net gain in energy from the fusion process, which translates into a net loss in mass going from the constituent light nuclei to the resultant heavy nuclei. This burning continues throughout the star's life, initially with hydrogen as the main fuel in this process, then with helium, and so on up the periodic table. The mass of the star determines the ultimate fuel that can be used; more massive stars will have denser cores for heavy nuclei burning to occur. If the star is massive enough ($\gtrsim$ 10–20 $M_\odot$), then silicon burning can be reached, the end product of which is iron. Because iron is the most compact atomic nucleus, it would *require* energy to fuse it into a heavier element, which is not in the best interests of the star. The iron core cannot support itself. It therefore contracts, and its temperature rises. At roughly 6×10^9 K, the iron photodisintegrates via $^{56}\mathrm{Fe} + \gamma \rightarrow 13\,^4\mathrm{He} + 4\mathrm{n}$. This process requires about 100 Mev, thus robbing the core of energy, which speeds up the contraction. Once all the iron has disintegrated, the processes $^4\mathrm{He} \rightarrow 2\mathrm{p} + 2\mathrm{n}$

and $p + e^- \rightarrow n + \bar{\nu}$ convert the core into a degenerate neutron gas. The layers above the core fall rapidly inward and heat up, continuing their nucleosynthesis. This goes off explosively, blowing off the outer layers. The resulting shock wave ejects much of the star's envelope into the surrounding circumstellar medium (CSM), which is the result of the stellar wind from the last stages of the star's life.

5.2 Circumstellar Interaction and the Origin of the X-ray Emission

The interaction of a spherically symmetric SN shock and a smooth CSM has been calculated in detail (Chevalier & Fransson, 1994; Suzuki & Nomoto, 1995). As the SN "outgoing" shock emerges from the star, its characteristic velocity is $\sim 10^4$ km s^{-1}, and the density distribution in the outer parts of the ejecta can be approximated by a power-law in radius, $\rho \propto r^{-n}$, with $7 \lesssim n \lesssim 20$. The outgoing shock propagates into a dense CSM formed by the pre-SN stellar wind. This wind is slow ($v_w \sim 10$ km s^{-1}) and was formed by a pre-supernova mass-loss rate of $\dot{M} \sim 10^{-4}$ to 10^{-6} M$_\odot$ yr^{-1}. The CSM density for such a wind decreases as the square of the radius ($\rho = \dot{M}/4\pi r^2 v_w$). The collision between the stellar ejecta and the CSM produces a "reverse" shock, which travels outward at $\sim 10^3$ km s^{-1} slower than the fastest ejecta. Interaction between the outgoing shock and the CSM produces a very hot shell ($\sim 10^9$ K) while the reverse shock/ejecta interaction produces a denser, cooler shell ($\sim 10^7$ K) with much higher emission measure and is where most of the observable X-ray emission arises. If either the CSM density or n is high, the reverse shock is radiative, resulting in a dense, partly-absorbing shell between the two shocks. In reality, and as explosion models show, the ejecta density is more complex. The X-ray temperature and ejecta velocity, as given by, e.g., the Hα line width, are sensitive functions of the density distribution. They therefore together consitute unique probes of the explosion dynamics, as well as nucleosynthesis.

Chevalier (1982) proposed that the outgoing shock from the SN explosion generates the relativistic electrons and enhanced magnetic field necessary for synchrotron radio emission. The ionized CSM initially absorbs most of this emission, except in cases where synchrotron self-absorption dominates, as may have been the case in SN 1993J (Chevalier, 1998; Fransson & Björnsson, 1998). However, as the shock passes rapidly outward through the CSM, progressively less ionized material is left between the shock and the observer, and absorption decreases rapidly. The observed radio flux density rises accordingly. At the same time, emission from the shock region is decreasing slowly as the shock expands so that, when radio absorption has become negligible, the radio light curve follows this decline. Observational evidence also exists at optical wavelengths for this interaction of SN shocks with the winds from pre-supernova mass loss (Filippenko, 1997).

All known radio supernovae appear to share common properties of (i) non-thermal synchrotron emission with a high brightness temperature, (ii) a decrease in absorption with time, resulting in a smooth, rapid turn-on first at shorter wavelengths and later at longer wavelengths, (iii) a power-law decline of the emission flux density with time at each wavelength after maximum flux density (absorption $\tau \approx 1$) is reached at that wavelength, and, (iv) a final, asymptotic approach of the spectral index α to an optically thin, non-thermal, constant negative value (Weiler et al., 1986). These properties are consistent with the Chevalier model.

The signatures of circumstellar interaction in the radio, optical, and X-ray regimes have been found for a number of Type II SNe such as the Type II-L SN 1979C (Fesen & Matonick, 1993; Immler, Pietsch, & Aschenbach, 1998a; Weiler et al., 1986, 1991) and the Type II-L SN 1980K (Canizares, Kriss, & Feigelson, 1982; Fesen & Becker, 1990; Leibundgut et al., 1991; Weiler et al., 1986, 1992). The Type IIn subclass has peculiar optical characteristics: narrow Hα emission superposed on a broad base; lack of P Cygni absorption-line profiles; a strong blue continuum; and slow evolution (Schlegel, 1990; Filippenko, 1997). The narrow optical lines are clear evidence for dense circumstellar gas — they probably arise from the reprocessing of the X-ray emission — and are another significant means by which the shock radiatively cools.

The best recent examples of Type IIn SNe include SNe 1978K, 1986J, 1988Z, 1994W (which may have been a peculiar Type II-P, Sollerman, Cumming, & Lundqvist 1998), 1995N, 1997eg, and 1998S.

5.3 Previous X-ray Observations of Supernovae

To date, 17 supernovae (SNe) have been detected in X-rays in the near aftermath (days to years) of their explosions[1]: SNe 1978K (Petre et al., 1994; Schlegel, 1995; Schlegel, Petre, & Colbert, 1996; Schlegel, 1999a), 1979C (Immler, Pietsch, & Aschenbach, 1998a; Kaaret, 2001; Ray, Petre, & Schlegel, 2001), 1980K (Canizares, Kriss, & Feigelson, 1982; Schlegel, 1994, 1995), 1986J (Houck et al., 1998; Schlegel, 1995; Chugai, 1993; Bregman & Pildis, 1992), 1987A (Burrows et al., 2000; Dennerl et al., 2001; Gorenstein, Hughes, & Tucker, 1994; Hasinger, Aschenbach, & Trüumper, 1996), 1988Z (Fabian & Terlevich, 1996), 1993J (Immler, Aschenbach, & Wang, 2001; Suzuki & Nomoto, 1995; Zimmermann et al., 1994), 1994I (Immler, Pietsch, & Aschenbach, 1998b; Immler, Wilson, & Terashima, 2002), 1994W (Schlegel, 1999b), 1995N (Fox et al., 2000), 1998S (Pooley et al., 2002), 1998bw (aka GRB 980425; Pian et al. 1999; Pian et al. 2000), 1999em (Fox et al., 1999; Schlegel, 2001; Pooley et al., 2002), 1999gi (Schlegel, 2001), 2001ig (Schlegel & Ryder, 2002), 2002ap (Sutaria, Ray, & Chandra, 2002; Rodriguez Pascual et al., 2002), and 2002hh (Pooley & Lewin, 2002).

In general, the high X-ray luminosities of these 17 SNe ($L_{\rm x} \sim 10^{38}$–10^{41} ergs s^{-1}) dominate the total radiative output of the SNe starting at an age of about one year. The X-ray observations have determined many properties of the individual SNe and, because they probe the very hot regions ($T \gtrsim 10^6$ K), can provide information unavailable in other wavelength regimes. In particular, the long-term monitoring of SN 1993J by Immler, Aschenbach, & Wang (2001) has shown the importance of X-ray observations as a tool to probe the CSM interaction and evolution of the progenitor. The

[1]A complete list of X-ray supernovae and references can be found at the website http://www.astro.psu.edu/~immler/supernovae_list.html.

nearly decade-long coverage of this source has uncovered $\sim 10^4$ yr in the progenitor's wind history and produced evidence that the progenitor was making a transition from the red to the blue supergiant phase during the late stages in evolution.

5.4 Instrumentation

The driving force in this work has been the observations made with the *Chandra X-ray Observatory*, described in §1.4.1. All observations discussed in chapters 6 and 7 were taken with the ACIS-S3 chip.

5.5 Investigation

I reduced and analyzed *Chandra* X-ray data of the Type II supernovae 1998S and 1999em. For SN 1999em, the data consisted of seven observations of 30 ksec each, logarithmically spaced from the fourth day after the explosion to the 633$^{\rm rd}$ day, and for SN 1998S, the data consisted of five observations of 20 ksec each, from the 678$^{\rm th}$ to the 1302$^{\rm nd}$ day after explosion.

I reduced each of the observations into a pair of flux measurements in hard and soft X-ray bands and an extracted spectrum, which I modeled to obtain an estimate of the temperature. From this, I constructed both the multicolor X-ray lightcurve and the temperature evolution of each supernovae. These measurements were used to determine the radiative cooling rate, the structure of the supernova ejecta, the structure of the circumstellar material, and the presence or absence of a dense shell of cold gas surrounding the reverse shock region for each of the supernovae. Some details of the stars' evolutions prior to their respective explosions were also able to be discerned. For example, an unexpected increase observed in the soft X-ray flux of SN 1999em could be due to an increase in the density of the circumstellar wind from the pre-supernova star, which signals an episode of mass ejection.

In the case of SN 1998S, I combined the data from all observations to produce a high-count spectrum which I could analyze in more detail using a hot plasma model

with variable elemental abundances (the VMEKAL model in XSPEC). In this summed spectrum, I found emission features from numerous heavy elements (Ne, Al, Si, S, Ar, Fe). This is the first time that such elements (except for Fe) have been seen in the X-ray spectrum of a young supernova. By comparing the observed abundances of these elements with the abundances predicted from numerical simulations, we were able to constrain the mass of the progenitor star. This is the first such analysis that has ever been performed with X-ray data.

Bibliography

Bregman, J. N.,& Pildis, R. A. 1992, ApJ, 398, L107

Burrows, D., Michael, E., Hwang, R., McCray, R., Chevalier, R., Petre, R., Garmire, G., Gordon, P., Holt, S., Nousek, J. 2000, ApJ, 543, L149

Canizares, C. R., Kriss, G. A., & Feigelson, E. D. 1982, ApJ, 253, L17

Chevalier, R. A. 1982, ApJ, 259, 302

Chevalier, R. A., & Fransson, C. 1994, ApJ, 420, 268

Chevalier, R. A. 1998, ApJ, 499, 810

Chugai, N. N. 1993, ApJ, 414, L101

Dennerl, K., et al., 2001, A&A, 365, L202

Fabian, A. C.,& Terlevich, R. 1996, MNRAS, 280, L5

Fesen, R. A., & Becker, R. H. 1990, ApJ, 351, 437

Fesen, R. A., & Matonick, D. M. 1993, ApJ, 407, 110

Filippenko, A. V. 1997, ARA&A, 35, 309

Fox, D. W., & Lewin, W. H. G. 1999, IAU Circ., 7318

Fox, D. W., Lewin, W. H. G., Fabian, A., Iwasawa, K., Terlevich, R., Zimmermann, H. U., Aschenbach, B., Weiler, K., Van Dyk, S., Chevalier, R., Rutledge, R., Inoue, H., & Uno, S. 2000, MNRAS, 319, 1154

Fransson, C., & Björnsson, C.-I. 1998, ApJ, 509, 861

Gorenstein, P., Hughes, J. P., Tucker, W. H., ApJ, 420, L25

Hasinger, G., Aschenbach, B., & Trüumper, J. 1996, A&A, 312, L9

Houck, J. C., Bregman, J. N., Chevalier, R. A., & Tomisaka, K. 1998, ApJ, 493, 431

Immler, S., Pietsch, W., & Aschenbach, B. 1998a, A&A, 331, 601

Immler, S., Pietsch, W., & Aschenbach, B. 1998b, A&A, 336, L1

Chapter 6

Supernova 1999em

This chapter is based on the original paper:

> "X-ray, Optical, and Radio Observations of the Type II Supernovae 1999em and 1998S," Pooley, D., Lewin, W. H. G., Fox, D. W., Miller, J. M., Lacey, C. K., Van Dyk, S. D., Weiler, K. W., Sramek, R. A., Filippenko, A. V., Leonard, D. C., Immler, S., Chevalier, R. A., Fabian, A. C., Fransson, C., & Nomoto, K., 2002, *The Astrophysical Journal*, Vol. 572, p. 932,

with the permission of the publisher, *The Astrophysical Journal.*

6.1 Abstract

Observations of the Type II-P (plateau) Supernova (SN) 1999em have enabled estimation of the profile of the SN ejecta, the structure of the circumstellar medium (CSM) established by the pre-SN stellar wind, and the nature of the shock interaction. SN 1999em is the first Type II-P detected at both X-ray and radio wavelengths. It is the least radio luminous and one of the least X-ray luminous SNe ever detected (except for the unusual and very close SN 1987A). The *Chandra* X-ray data indicate non-radiative interaction of SN ejecta with a power-law density profile ($\rho \propto r^{-n}$ with $n \sim 7$) for a pre-SN wind with a low mass-loss rate of $\sim 2 \times 10^{-6}$ $M_\odot$ yr^{-1} for a wind velocity of 10 km s^{-1}, in agreement with radio mass-loss rate estimates. The *Chandra*

Immler, S., Aschenbach, B., Wang, Q. D. 2001, ApJ, 561, L107

Immler, S., Wilson, A. S., Terashima, Y. 2002, ApJ, 573, L27

Kaaret, P. 2001, ApJ, 560, 715

Leibundgut, B., Kirshner, R. P., Pinto, P. A., Rupen, M. P., Smith, R. C., Gunn, J. E., & Schneider, D. P. 1991, ApJ, 372, 531

Petre, R., Okada, K., Mihara, T., Makishima, K., & Colbert, E. J. M. 1994, PASJ, 46, L115

Pooley, D., Lewin, W. H. G., Fox, D. W., Mill er, J. M., Lacey, C. K., Van Dyk, S. D., Weiler, K. W., Sramek, R. A., Filippenk o, A. V., Leonard, D. C., Immler, S., Chevalier, R. A., Fabian, A. C., Fransson, C., & Nomoto, K. 2002, ApJ, 572, 932

Pooley, D. & Lewin, W. H. G. 2002, IAU Circ., 8024

Ray, A., Petre, R., Schlegel, E. M. 2001, AJ, 122, 966

Rogriguez Pascual, R., Gonzalez Riestra, R., Gonzalez Garcia, B., Santos Lleo, M., Guainazzi, M., & Schartel, N. 2002, IAU Circ., 7821

Schlegel, E. M. 1990, MNRAS, 244, 269

Schlegel, E. M. 1994, AJ, 108, 1893

Schlegel, E. M. 1995, Rep. Prog. Phys., 58, 1375

Schlegel, E. M., Petre, R., Colbert, E. J. M. 1996, ApJ, 456, 187

Schlegel, E. M., Ryder, S., Staveley-Smith, L., Petre, R., Colbert, E., Dopita, M., & Campbell-Wilson, D. 1999a, AJ, 118, 2689

Schlegel, E. M. 1999b, ApJ, 527, L85

Schlegel, E. M. 2001, ApJ, 556, L25

Schlegel, E. M. & Ryder, S. 2002, IAU Circ., 7424

Sollerman, J., Cumming, R. J., & Lundqvist, P. 1998, ApJ, 493, 933

Sutaria, F. K., Ray, A., & Chandra, P. 2002, astro-ph/0210623

Suzuki, T., & Nomoto, K. 1995, ApJ, 455, 658

Weiler, K. W., Sramek, R. A., Panagia, N., van der Hulst, J. M., & Salvati, M. 1986, ApJ, 301, 790

Weiler, K. W., Van Dky, S. D., Panagia, N., Sramek, R. A., & Discenna, J. L. 1991, ApJ, 380, 161

Weiler, K. W., Van Dyk, S. D., Panagia, N., & Sramek, R. A. 1992, ApJ, 398, 248

Zimmermann, U., Lewin, W., Predehl, P., Aschenbach, B., Fabbiano, G., Hasinger, G., Lubin, L., Magnier, E., van Paradijs, J., Petre, R., Pietsch, W., Trümper, J. 1994, Nature, 367, 621

data show an unexpected, temporary rise in the 0.4–2.0 keV X-ray flux at ~100 days after explosion.

6.2 Introduction

SN 1999em was optically discovered on 1999 October 29 in NGC 1637, approximately 15″ west and 17″ south of the galactic nucleus (Li et al., 1999). The spectrum on 1999 October 29 shows a high temperature (Baron et al., 2000), indicating that the supernova was discovered at an early phase. We take 1999 October 28 as the date of the explosion. SN 1999em reached a peak brightness of $m_V \approx 13.8$ mag on about day 4, and remained in the "plateau phase," an enduring period of nearly constant V-band brightness, until about 95 days after discovery (Leonard & Filippenko, 2001). At an estimated distance of 7.8 Mpc (Sohn & Davidge 1998; see also Hamuy et al. 2001 who find a distance of 7.5 Mpc to SN 1999em based on the Expanding Photosphere Method), this is the closest Type II-P supernova yet observed, and it is the only Type II-P observed in both X-rays and radio. Its maximum brightness of $M_V \approx -15.75$ marks it as one of the optically least luminous SNe II-P (cf. Patat et al., 1994). Smartt et al. (2002) recently derived a mass of 12 ± 1 $M_\odot$ for the progenitor of SN 1999em.

6.3 Observations

6.3.1 X-ray

The trigger for our first *Chandra* observation was the optical discovery of a SN within 10 Mpc. The extremely rapid response of the *Chandra* staff allowed us to catch SN 1999em three days after discovery. We observed SN 1999em on 1999 November 1, November 13, December 16, 2000 February 7, October 30, 2001 March 9, and July 22 (days 4, 16, 49, 102, 368, 495, and 630 from reference). A summary of the observations is given in Table 6.1, and Schlegel (2001) also discusses the first three. All observations were performed by the Advanced CCD Imaging Spectrometer (ACIS) with the telescope aimpoint on the back-side illuminated S3 chip, which offers

increased sensitivity to low energy X-rays over the front-side illuminated chips. The first two observations used a 1/2 subarray mode (only half of the CCD was read out), while the rest used the full CCD. The data were taken in timed-exposure (TE) mode using the standard integration time of 3.2 sec per frame and telemetered to the ground in very faint (VF) mode for the first two observations and faint (F) mode for the rest. In VF mode, the telemetered data contain the values of 5 $\times$ 5 pixel islands centered on each event, while in F mode the islands are 3 $\times$ 3 pixels.

6.3.2 Radio

We observed SN 1999em over 30 times with the Very Large Array (VLA)[1] at frequencies ranging from 43.3 GHz to 1.5 GHz and ages from 3 to 454 days after the discovery date of 1999 October 29 (Lacey et al., 2002). Except for six weak but significant ($> 3\sigma$) detections at mid-cm wavelengths (1.5 – 8.4 GHz) at ages of between 33 and 69 days, all measurements yielded only upper limits.

6.3.3 Optical

Extensive optical ground-based observations were made of SN 1999em; these include *UBVRI* photometry, long-term spectroscopy, and spectropolarimetry (Leonard et al., 2001). These data were used to obtain a distance with the Expanding Photosphere Method (Leonard & Filippenko, 2001). Both the photometry and spectroscopy suggest that this was a relatively normal Type II-P event. We note, however, that SN 1999em was about 1 magnitude fainter in the V-band during the plateau than the average of the 8 SNe II-P with published photometry and previously derived EPM distances, and it may have also had a somewhat unusual color evolution (Leonard & Filippenko, 2001).

Spectropolarimetry of SN 1999em was obtained on 1999 November 5, December 8, and December 17 (7, 40, and 49 days after discovery, respectively, while it was still in its plateau phase) with the Kast double spectrograph (Miller & Stone, 1993) with

[1]The VLA is operated by the NRAO of the AUI under a cooperative agreement with the NSF.

polarimeter at the Cassegrain focus of the Shane 3-m telescope at Lick Observatory. Similarly, on 2000 April 5 and 9 (159 and 163 days after discovery, long after the plateau). The Low-Resolution Imaging Spectrometer (Oke et al., 1995) was used in polarimetry mode (LRISp; Cohen, 1996) at the Cassegrain focus of the Keck-I 10-m telescope. Leonard et al. (2001) discuss the details of the polarimetric observations and reductions.

Total flux spectra[2] were obtained at many epochs, primarily with the Nickel 1-m and Shane 3-m reflectors at Lick Observatory. *UBVRI* photometry was conducted with the 0.8-m Katzman Automatic Imaging Telescope (KAIT; Li et al. 2000; Filippenko et al. 2001) at Lick Observatory. These data and their implications are thoroughly discussed by Leonard & Filippenko (2001).

6.4 *Chandra* Data Reduction

For each observation, we followed the data preparation threads provided by the *Chandra* X-ray Center. We used the *Chandra* Interactive Analysis of Observations (CIAO) software (version 2.2) to perform the reductions, along with the CALDB 2.10 calibration files (gain maps, quantum efficiency, quantum efficiency uniformity, effective area). Bad pixels were excluded, and intervals of bad aspect were eliminated.

All data were searched for intervals of background flaring, in which the count rate can increase by factors of up to 100 over the quiescent rate. The light curves of background regions were manually inspected to determine intervals in which the quiescent rate could be reliably calculated. In accordance with the prescription given by the ACIS Calibration Team, we identify flares as having a count rate $\gtrsim$30% of the quiescent rate. Background flares were found in each of the first four and the last observation of SN 1999em, lasting from hundreds of seconds to over 15 ksec. The event lists were filtered to exclude the time intervals during which flares occurred. Effective observation times after filtering are listed in Table 6.1.

[2]These spectra are produced from all available source photons, as opposed to the "polarized flux spectra" which refer only to the net polarization as a function of wavelength.

Table 6.1: *Chandra* Observations of SN 1999em.

Date	Day (From Ref.)	Length (ksec)	Filtered Length (ksec)	Count Rate (cts ksec^{-1})	f_x[2–10 keV]/ f_x[0.4–2 keV]
1999 Nov 1	4	29.0	21.6	3.70	2.1 ± 0.9
1999 Nov 13	16	26.0	10.6	2.46	0.8 ± 0.4
1999 Dec 16	49	35.3	35.1	1.02	0.7 ± 0.5
2000 Feb 7	102	38.5	23.9	1.84	0.2 ± 0.1
2000 Oct 30	368	26.4	26.4	0.46	0.9 ± 0.5
2001 Mar 9	495	26.7	24.6	0.31	0*
2001 Jul 22	630	29.8	25.1	0.19	0*

*No flux detected above 2 keV.

In addition, we have performed a reprocessing of all data so as not to include the pixel randomization that is added during standard processing. This randomization has the effect of removing the artificial substructure (Moiré pattern) that results as a byproduct of spacecraft dither. Since all of our observations contained a substantial number of dither cycles (one dither cycle has a period of ~1000 sec), this substructure is effectively washed out, and there is no need to blur the image with pixel randomization. Removing this randomization slightly improves the point spread function (PSF).

The source spectra were extracted with the CIAO tool *dmextract*. We excluded events with a pulse invariant (PI) of either 0 (underflow bins) or 1024 (overflow bins). The region of extraction was determined from the CIAO tool *wavdetect*, a wavelet-based source detection algorithm which can characterize source location and extent. In each observation, the region determined by *wavdetect* for the SN is consistent with that of a point source. The data were restricted to the energy range of 0.4–8.0 keV for the purposes of spectral analysis since the effective area of ACIS falls off considerably below 0.4 keV and the increased background above 8 keV makes this data unreliable.

Table 6.2: X-ray Temperature Evolution of SN 1999em.

Day (From Ref.)	MEKAL kT (keV)	Brems. kT (keV)	Model kT ($n = 7$) (keV)	Model kT ($n = 9$) (keV)
4	$5.0^{+5.1}_{-2.1}$	$5.2^{+11.5}_{-2.3}$	9.2	4.1
16	$2.5^{+2.7}_{-0.9}$	$2.3^{+5.9}_{-1.1}$	5.4	2.8
49	$2.9^{+2.6}_{-1.1}$	$2.2^{+3.2}_{-0.9}$	3.4	2.0
102	$0.8^{+0.2}_{-0.1}$	$1.1^{+0.7}_{-0.4}$	2.5	1.6
368	$1.0^{+0.7}_{-0.3}$	$1.5^{+6.5}_{-0.8}$	1.5	1.1

Listed uncertainties are 90% confidence intervals.

6.5 Results

6.5.1 X-ray

The source was detected on all occasions, and an overlay of the X-ray contours from the first observation on an optical image of the host galaxy is shown in Fig. 6-1. The *wavdetect* position[3] (based solely on the *Chandra* aspect solution) is $4^{\rm h}41^{\rm m}27\overset{\rm s}{.}16$, $-2°51'45\overset{''}{.}6$, which is within $1''$ (roughly the *Chandra* pointing accuracy) of the radio and optical positions. The low flux ($f_{\rm x} \lesssim 10^{-14}$ ergs cm^{-2} s^{-1}) resulted in few total counts (see Table 1). We have fit both the MEKAL and thermal Bremsstrahlung models to our data. The MEKAL model is a single-temperature, hot diffuse gas (Mewe, Gronenschild, & van den Oord, 1985) with elemental abundances set to the solar values of Anders & Grevesse (1989). We have calculated the column density (Predehl & Schmitt, 1995) to be $N_{\rm H} = 6.1 \times 10^{20}$ cm^{-2} based upon a value of $E_{(B-V)} = 0.05$ (Baron et al., 2000). For both models, only the temperatures and overall normalizations were allowed to vary. In XSPEC (Arnaud, 1996), we performed maximum likelihood fits on the unbinned data using Cash statistics (Cash, 1979). These fits should be insensitive to the number of counts per channel and are thus appropriate for fitting low-count data. The best-fit observed temperatures are shown in Table 6.2. As expected, the uncertainties in fit parameters for such low-count data are large.

We have also used flux ratios to characterize the source. The fluxes were calculated by manually integrating the source spectra, i.e., they are model-independent,

[3]This is the average position of observations 2–6, in which the standard deviations were $\sigma_{\rm RA} = 0\overset{''}{.}03$ and $\sigma_{\rm Dec} = 0\overset{''}{.}4$. Observation 1 had a known aspect error and was off by $\sim 3''$. This offset was corrected for Fig. 6-1.

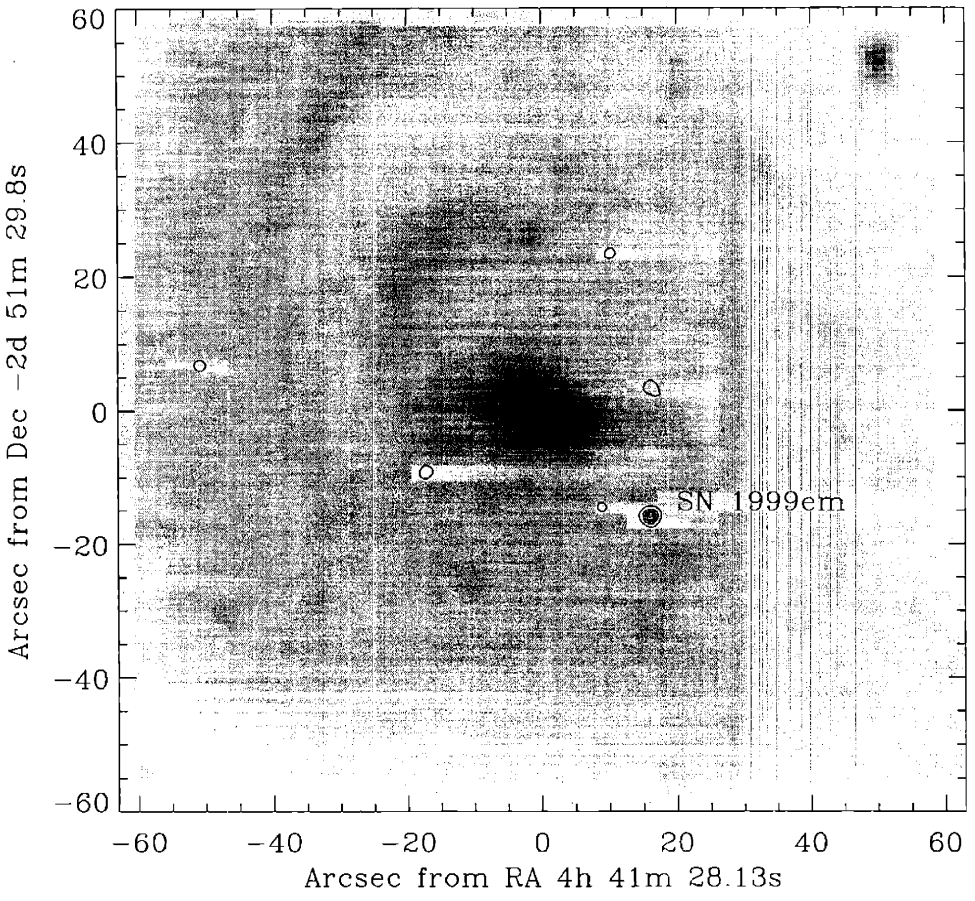

Figure 6-1: NGC 1637 in optical and X-rays. X-ray contours from the first *Chandra* observation of SN 1999em are overlaid on a DSS image of the host galaxy.

absorbed fluxes. The first observation had a flux ratio of $f_{\rm x}$[2–8 keV]/$f_{\rm x}$[0.4–2 keV] $= 2.1 \pm 0.9$, but later observations were softer (Table 6.1). Somewhat surprisingly, the total flux nearly doubled from the third observation to the fourth, despite the continued decline of the high-energy X-rays. The multicolour X-ray lightcurve is shown in Fig. 6-2.

6.5.2 Radio

After 15 unsuccessful VLA observations of SN 1999em at ages 4 to 19 days after the assumed explosion date of 1999 October 28, the SN was finally detected on day 34 with 0.190 mJy flux density at 8.435 GHz. Subsequent observing on days 46, 60, and 70 indicated that SN 1999em remained detectable at a similar flux density, near the sensitivity limit of the VLA, at 8.435, 4.885, and 1.465 GHz. The data are

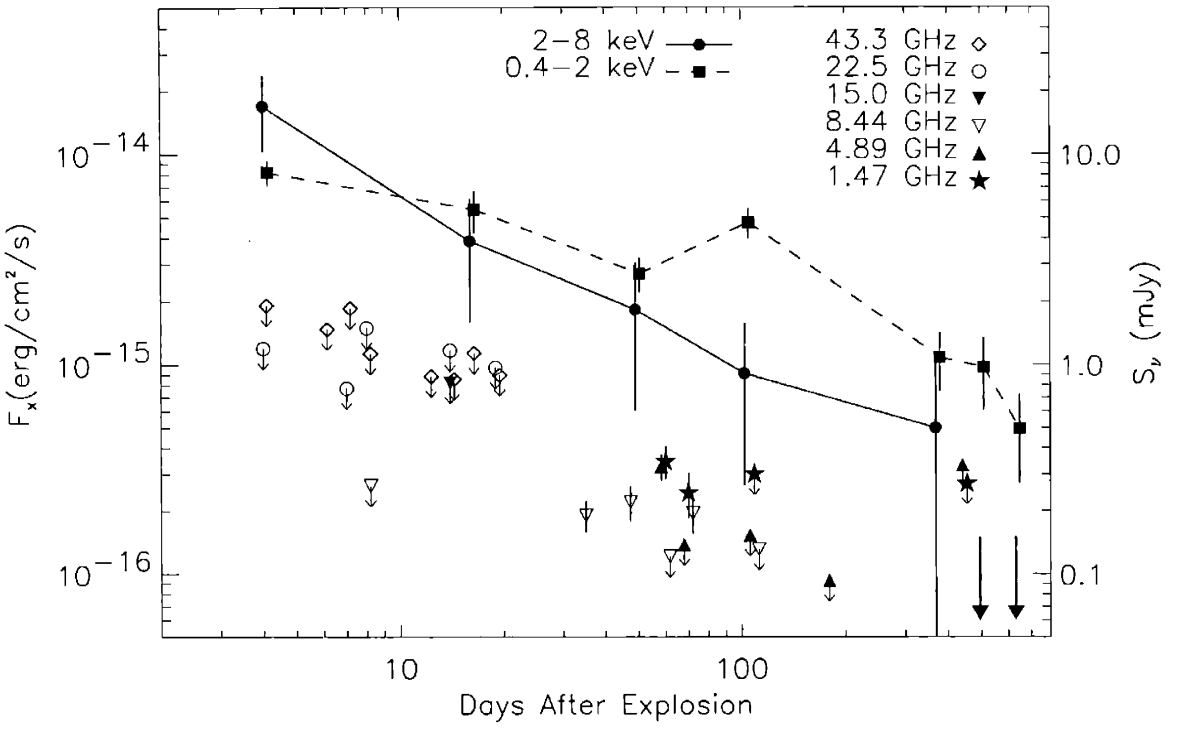

Figure 6-2: X-ray and radio light curves of SN 1999em. The detections are shown with error bars while the upper limits are shown with downward arrows. Radio flux densities are plotted with the appropriate symbols. The absorbed X-ray flux is plotted in both the 2–8 keV (*solid line*) and 0.4–2 keV (*dashed line*) bands. The hard X-rays follow a steady decline, but the soft X-rays double from the third observation to the fourth.

shown, together with the x-ray results, in Fig. 6-2. Since day 70, no radio detection of SN 1999em in any cm wavelength band has been obtained. SN 1999em is among only a few radio detected Type II-P, and its behavior is difficult to compare with other radio observations of the same type SN. An estimated spectral luminosity of SN 1999em at 6 cm peak on day ~34 of $L_{6\mathrm{cm\ peak}} \sim 2.2 \times 10^{25}$ erg s^{-1} Hz^{-1} makes it the least radio luminous RSN known except for the peculiar, and very nearby, SN 1987A. The radio position of the emission from SN 1999em is $4^{\mathrm{h}}41^{\mathrm{m}}27\overset{\mathrm{s}}{.}157$, $-2°51'45\overset{''}{.}83$ (J2000). The details of the observations and analysis will be found in Lacey et al. (2002).

6.5.3 Optical

The spectropolarimetry of SN 1999em provided a rare opportunity to study the geometry of the electron-scattering atmosphere of a "normal" core-collapse event at

multiple epochs (Leonard et al., 2001). A very low but temporally increasing polarization level suggests a substantially spherical geometry at early times that becomes more aspherical at late times as ever-deeper layers of the ejecta are revealed. When modeled in terms of oblate, electron-scattering atmospheres, the observed polarization implies an asphericity of at least 7% during the period studied. We speculate that the thick hydrogen envelope intact at the time of explosion in SNe II-P might serve to dampen the effects of an intrinsically aspherical explosion. The increase in asphericity seen at later times is consistent with a trend recently identified (Wang et al., 2001) among stripped-envelope core-collapse SNe: the deeper we peer, the more evidence we find for asphericity. The natural conclusion that it is an *explosion* asymmetry that is responsible for the polarization has fueled the idea that some core-collapse SNe produce gamma-ray bursts (GRB; e.g., Bloom et al. 1999) through the action of a jet of material aimed fortuitously at the observer, the result of a "bipolar," jet-induced, SN explosion (Khokhlov et al., 1999; Wheeler et al., 2000; Maeda et al., 2002). Additional multi-epoch spectropolarimetry of SNe II-P are clearly needed, however, to determine if the temporal polarization increase seen in SN 1999em is generic to this class.

6.6 Discussion

To interpret the X-ray and radio data on SN 1999em, we use the circumstellar interaction model proposed by Chevalier (1982), and elaborated by Chevalier & Fransson (1994) and Fransson, Lundqvist, & Chevalier (1996; hereafter, FLC96). The outer supernova ejecta are taken to be freely expanding, with a power law density profile

$$\rho_{sn} = At^{-3}(r/t)^{-n}, \tag{6.1}$$

where A and n are constants. SN 1999em was a Type II-P SN, so we expect that the star exploded as a red supergiant with most of its hydrogen envelope. The value of n for such a star is usually taken to be in the range $7 - 12$ (Chevalier, 1982), although

Matzner & McKee (1999) recently found that the explosion of a red supergiant leads to $n = 11.9$ at high velocity. In the case of SN 1999em, we have some additional information from modeling of the optical spectrum. Baron et al. (2000) were able to model spectra on 1999 October 29 and November 4/5 with $n = 7$, 8, or 9. The modeling of the data for the earlier time suggests a relatively flat density profile ($n = 7$). The spectra on 1999 October 29 also show evidence for a secondary absorption feature at 20,000 km s^{-1}, implying the presence of denser material in the cool ejecta. One possible origin for high velocity, dense ejecta is the shell that can form as a result of the diffusion of radiation at the time of shock breakout (Chevalier 1976); if this is the origin, it represents the highest velocity material in the ejecta. We assume that the outer density profile can be approximated as a power law out to this high velocity and take $n = 7$ or 9. The value of A is equivalent to specifying the density in the ejecta at some particular velocity and age. The model by Baron et al. (2000) for 1999 October 29 has $\rho_{sn} = 0.4 \times 10^{-20}$ g cm^{-3} at 10,000 km s^{-1} at an age of 1 year. This value is in approximate accord with the density found in models with a broken power law density profile, mass of 10 M$_\odot$, and energy of 1×10^{51} ergs (Chevalier & Fransson, 1994).

The density in the wind is $\rho_w = \dot{M}/(4\pi r^2 v_w)$, where $\dot{M}$ is the mass-loss rate and v_w is the wind velocity. We take $\dot{M}_{-6} = \dot{M}/10^{-6}$ M$_\odot$ yr^{-1} and $v_{w1} = v_w/10$ km s^{-1} as reference values. The interaction of the supernova with a freely expanding wind leads to a shocked shell with radius $R \propto t^{0.8} (n = 7)$ or $t^{6/7} (n = 9)$. This shell is the source of the X-ray emission. The low observed X-ray luminosity suggests that the shocked gas is not radiative; this can be checked for consistency after a model is produced. Under these conditions, the X-ray luminosity is expected to be dominated by emission from the reverse shock region, which is relatively cool, as observed. The luminosity of the shell can be estimated from eq. (3.10) of FLC96

$$L_{rev} = 2.0 \times 10^{35} \zeta (n-3)(n-4)^2 T_8^{-0.24} e^{-0.116/T_8} \left(\frac{\dot{M}_{-6}}{v_{w1}}\right)^2 V_4^{-1} \left(\frac{t}{10 \text{ days}}\right)^{-1} \text{ ergs s}^{-1} \text{ keV}^{-1}, \tag{6.2}$$

where ζ is 0.86 for solar abundances and 0.60 for $n(\text{He})/n(\text{H}) = 1$, $T_8 = T/10^8$ K, and V_4 is the peak velocity in units of 10^4 km s^{-1}. Baron et al. (2000) find possible evidence for enhanced He in SN 1999em, but this is uncertain and is probably not expected in

a Type II-P SN. We take $\zeta = 0.86$; the uncertainty is small. On 1999 November 1, which we take to be day 4, the observed luminosity (0.4–8 keV) is 2×10^{38} ergs s^{-1} and the temperature is 5.0 keV. With $V_4 = 1.5$, we find that $\dot{M}_{-6}/v_{w1} \approx 1$ ($n = 9$) or 2 ($n = 7$), quite similar to the value of $\dot{M}_{-6}/v_{w1} \sim 2$ obtained above from the radio observations. With this mass-loss rate, the cooling time for the gas, as deduced from eq. (3.7) of FLC96, is 31 days for $n = 9$ and is longer for the $n = 7$ case, which justifies our use of the adiabatic expression for the X-ray luminosity. The cooling time grows more rapidly than the age, so we expect non-radiative evolution through the time of our observations. If cooling were important, a dense shell would form that could absorb X-ray emission from the reverse shock wave, as appeared to occur in the initial evolution of SN 1993J (FLC96; Suzuki & Nomoto 1995). Reradiation of the absorbed emission can give broad optical emission lines, as observed in SN 1993J at ages $\gtrsim 1$ year. Such lines were not observed in SN 1999em, which is consistent with non-radiative evolution.

From eq. (2.2) of FLC96 with $n = 9$, we find that the maximum velocity for $n = 9$ is

$$V = \left(\frac{4\pi \rho_o t_o^3 v_o^9 v_w}{15\dot{M}} \right)^{1/7} t^{-1/7}, \tag{6.3}$$

where ρ_o specifies an ejecta density at a particular time t_o and velocity v_o, as described above. At $t = 4$ days with $\rho_o = 0.4 \times 10^{-20}$ g cm^{-3} at $v_o = 10{,}000$ km s^{-1} and $t_o = 1$ year and $\dot{M}_{-6}/v_{w1} = 1$, we have $V = 13{,}000$ km s^{-1}. For the $n = 7$ case with $\dot{M}_{-6}/v_{w1} = 2$, we have $V = 14{,}000$ km s^{-1} and $V \propto t^{-0.2}$. These velocities are lower than the highest velocities deduced by Baron et al. (2000) on 1999 October 29 (day 1). However, there is some uncertainty in the high velocity, and there may have been rapid evolution at early times.

The shock velocity determines the temperature of the reverse shock region. From eqs. (3.1) and (3.2) of FLC96, we have $T_{\rm rev} = 2.4 V_4^2$ keV for $n = 9$, so that with $V_4 = 1.3$, $T_{\rm rev} = 4.1$ keV. For $n = 7$, we have $T_{\rm rev} = 4.8 V_4^2$ keV so $T_{\rm rev} = 9.4$ keV for $V_4 = 1.4$. The observed temperature on 1999 November 1 falls between these two cases. The predicted evolution of the temperature is $T \propto V^2 \propto t^{-2/(n-2)} \propto t^{-2/7}$

($n = 9$) and $\propto t^{-0.4}$ ($n = 7$). Table 6.2 compares this predicted evolution with that observed. The observations show a clear cooling, as expected. An additional factor could be the lack of electron-ion equilibration at the reverse shock front; if it is not achieved, the electrons are cooler than the above estimate. From eq. (3.6) of FLC96, the expected conditions are such that the equilibration timescale is comparable to the age throughout the evolution, so that no firm conclusion can be drawn. The fact that cooling of the emission is clearly observed argues for a relatively flat density profile for the ejecta, as also found by Baron et al. (2000) from optical spectroscopy.

An estimate of the expected evolution of the total X-ray luminosity, $L_{\rm x}$, is given by Chevalier & Fransson (1994). When free-free emission dominates ($T \geq 4 \times 10^7$ K), $L_{\rm x} \propto t^{-1}$, and when lines dominate ($10^5 \leq T < 4 \times 10^7$ K), $L_{\rm x} \propto t^{-0.69}$ ($n = 9$) or $\propto t^{-0.56}$ ($n = 7$). The observed evolution is less steep than t^{-1} and is closer to the expectation for line emission. The observed temperatures indicate that a transition occurred. Again, the observations are in approximate accord with expectations.

One aspect of the X-ray observations that is not compatible with the simplest wind interaction model is the increase of the soft X-ray flux on 2000 February 2 (day 102, see Fig. 6-2). In our model, the emission is primarily from the reverse shocked ejecta, so the increase could be due to a region of increased density in the ejecta. At this age, the velocity of the ejecta entering the reverse shock front is $\sim 8,000$ km s^{-1}. Alternatively, the emission could be from an inhomogeneity in the circumstellar wind. The smooth wind is shocked to a temperature $\sim 10^9$ K, so that a density contrast of ~ 100 is needed for the inhomogeneity. The inhomogeneity must be large to affect the total luminosity, but a substantial change in stellar mass-loss characteristics at only 10^{16} cm from the star is unlikely. The fact that the change is transitory also argues against a change in mass-loss properties at this point.

Although SN 1999em was detected as a weak radio source, the radio light curves are not well defined because of the very low radio flux density. The early observations were not of sufficient sensitivity to detect the source so the time of light curve peak and the early absorption process are also not well defined. The 8.44 GHz observations are the most useful in this regard. At late times, the observed flux evolution of other

radio supernovae is $\propto t^{-0.7}$, or steeper (Weiler et al., 1986), so that the 8.44 GHz upper limit on day 7 probably indicates that absorption was significant at that time. With this value for the time of peak flux at 8.44 GHz (actually a lower limit), we can place SN 1999em on a diagram of peak radio luminosity vs. time of peak (Fig. 6-3). The diagonal lines show the velocity of the shocked shell if synchrotron self-absorption were the important process for the early absorption (Chevalier, 1998). The position of SN 1999em gives about $10,000$ km s^{-1}, or less, as the shell velocity. Thus, it is just possible that synchrotron self-absorption was important at early times but more likely that another process, probably free-free absorption by the unshocked wind, was dominant. From eq. (2.3) of FLC96, the 8.44 GHz free-free optical depth on day 7 with V_4 and $\dot{M}_{-6}/v_{w1}$ as deduced above is $\tau = 0.2T_5^{-3/2}$ $(n = 9)$ or $0.5T_5^{-3/2}$ $(n = 7)$, where T_5 is the temperature of the unshocked wind in units of 10^5 K. The $n = 7$ case is somewhat more consistent with the observations because of the higher mass-loss rate deduced for this case.

The free-free absorption of the radio emission depends on the circumstellar temperature. Eastman et al. (1994) find from a simulation of a Type II-P explosion an effective temperature at outbreak of $T_{\rm eff} = 1.8\times10^5$ K and luminosity 9×10^{44} ergs s^{-1}. This temperature is similar to that used in one model by Lundqvist & Fransson (1991) for SN 1987A (their Table 1). Their model with $\dot{M}_{-6}/v_{w1} = 0.4$ gives a wind temperature of 1.2×10^5 K for $T_{\rm eff} = 2 \times 10^5$ K. Because of the low wind density, this temperature is not sensitive to the mass-loss rate and is mainly set by the outburst radiation temperature. An approximate temperature in the wind of SN 1999em should therefore be $T_5 \approx 1.2$. The temperature at $\sim$30 days should not be very different because of the low wind density. X-ray heating by the shock has not been included here, but is probably not important because of the low X-ray luminosity.

Overall, the X-ray and radio observations of SN 1999em are consistent with the non-radiative interaction of supernova ejecta with a power law profile ($n \sim 7$) interacting with a pre-supernova wind with $\dot{M}_{-6}/v_{w1} \approx 2$. We estimate the accuracy of this mass-loss density to be a factor of 2. The X-ray emission is primarily from the reversed shocked ejecta, and the model can account for the luminosity, temperature,

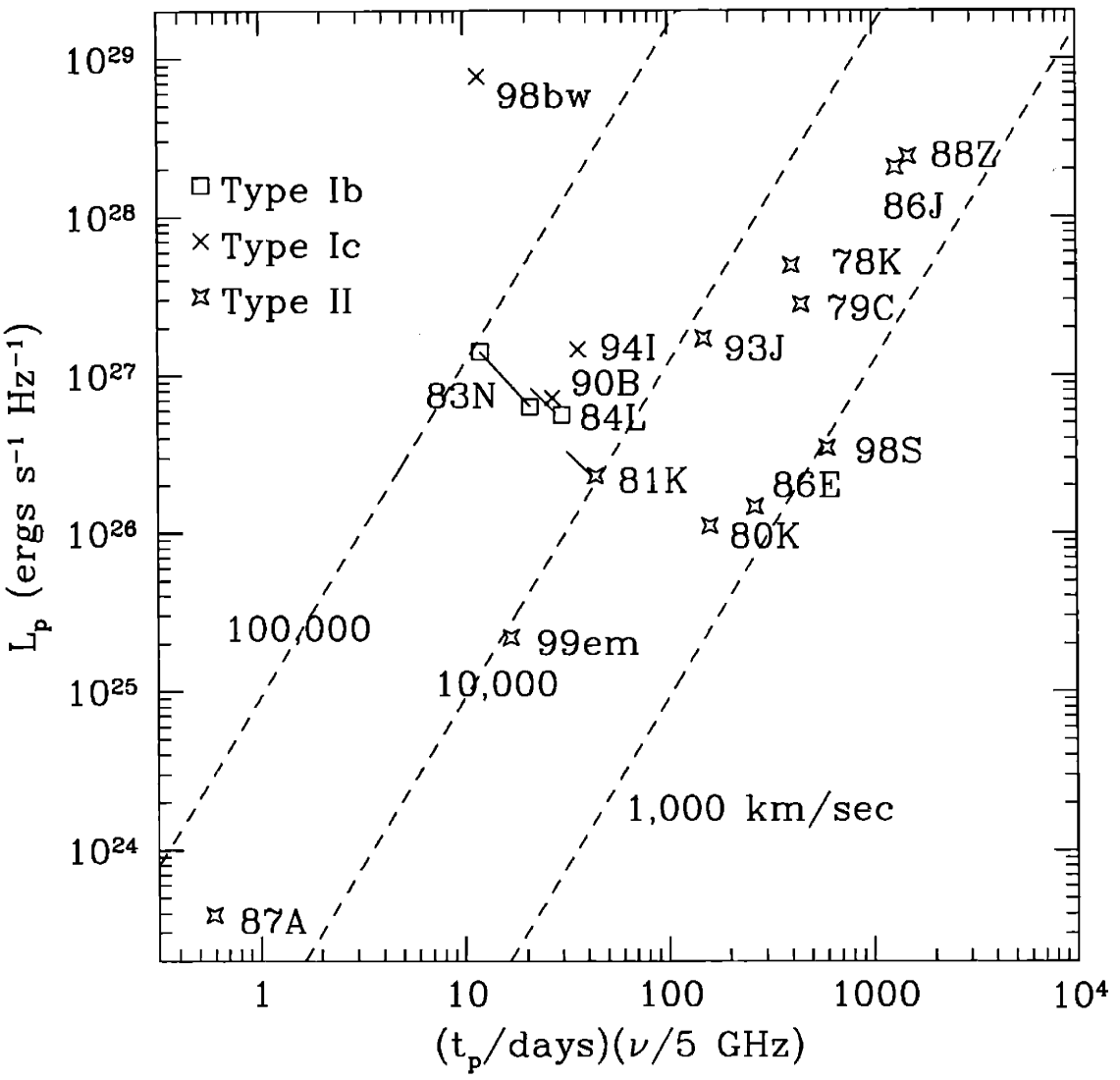

Figure 6-3: The peak spectral radio luminosity vs the product of the time of the peak and the frequency of the measurement, based on Fig. 4 of Chevalier (1998) with the addition of SN 1998bw, SN 1998S, and SN 1999em. The observed supernovae are designated by the last two digits of the year and the letter, and are of Types II (*stars*), Ib (*squares*), and Ic (*crosses*). The dashed lines show the mean velocity of the radio shell if synchrotron self-absorption is responsible for determining the flux density peak; an electron spectrum $N(E) \propto E^{-2.5}$ is assumed.

and temperature evolution of the emission. It does not account for the large soft X-ray flux observed on day 102. The radio observations are compatible with this general picture and suggest a comparable mass-loss rate.

Bibliography

Anders, E., & Grevesse, N. 1989, Geochim. Cosmochim. Acta, 53 197

Arnaud, K. 1996, in Jacoby, G., & Branes, J., eds, ASP Conf. Ser. Vol. 101, Astronomical Data Analysis Software and Systems V, Astron. Soc. Pac., San Francisco

Arnett, W. D., Bahcall, J. N., Kirshner, R., & Woosley, S. E. 1989, ARA&A, 27, 629

Baron, E., Branch, D., Hauschildt, P. H., Filippenko, A. V., Kirshner, R. P., Challis, P. M., Jha, S., Chevalier, R. A., Fransson, C., Lundqvist, P., Garnavich, P., Leibundgut, B., McCray, R., Michael, E., Panagia, N., Phillips, M. M., Pun, C. S. J., Schmidt, B., Sonneborn, G., Suntzeff, N. B., Wang, L., & Wheeler, J. C. 2000, ApJ, 545, 444

Bloom, J. S., Kulkarni, S. R., Djorgovski, S. G., Eichelberger, A. C., Cote, P., Blakeslee, J. P., Odewahn, S. C., Harrison, F. A., Frail, D. A., Filippenko, A. V., Leonard, D. C., Riess, A. G., Spinrad, H., Stern, D., Bunker, A., Dey, A., Grossan, B., Perlmutter, S., Knop, R. A., Hook, I. M., & Feroci, M. 1999, Nature, 401, 453

Branch, D., Falk, S. W., McCall, M. L., Rybski, P., Uomoto, A. K., & Wills, B. J. 1981, ApJ, 244, 780

Cash, W. 1979, ApJ, 228, 939

Chevalier, R. A. 1976, ApJ 207, 872

Chevalier, R. A. 1982, ApJ, 259, 302

Chevalier, R. A., & Fransson, C. 1994, ApJ, 420, 268

Chevalier, R. A. 1998, ApJ, 499, 810

Cohen, M. H. 1996, The LRIS Polarimeter (Keck Obs. Instrument Manual), http://www2.keck.hawaii.edu:3636/

Eastman, R. G., Woosley, S. E., Weaver, T. A., & Pinto, P. A. 1994, ApJ, 430, 300

Ebisuzaki, T., Shigeyama, T., & Nomoto, K. 1989, ApJ, 344, L65

Filippenko, A. V., & Barth, A. J. 1997, IAU Circ., 6794

Fransson, C., Lundqvist, P., & Chevalier, R. A. 1996, ApJ, 461, 993, (FLC96)

Hachisu, I., Matsuda, T., Nomoto, K., & Shigeyama, T. 1992, ApJ, 390, 230

Hamuy, M., Pinto, P. A., Maza, J., Suntzeff, N. B., Phillips, M. M., Eastman, R. G., Smith, R. C., Corbally, C. J., Burstein, D., Li, Y., Ivanov, V., Moro-Martin, A., Strolger, L. G., de Souza, R. E., dos Anjos, S., Green, E. M., Pickering, T. E., González, L., Antezana, R., Wischnjewsky, M., Galaz, G., Roth, M., Persson, S. E., & Schommer, R. A. 2001, ApJ, 558, 615

Immler, S., Wilson, A. S., Terashima, Y. 2002, submitted to ApJ

Khokhlov, A. M., Höflich, P. A., Oren, E. S., Wheeler, J. C., Wang, L., & Chtchelkanova, A. Yu. 1999, ApJ, 524, L107

Lacey, C. K., Weiler, K. W., Van Dyk, S. D., Panagia, N., & Sramek, R. A. 2002, in preparation

Leonard, D. C., Filippenko, A. V., Ardila, D. R., & Brotherton, M. S. 2001, ApJ, 553, 861

Leonard, D. C. & Filippenko, A. V. 2001, PASP, 113, 920

Li, W.-D., et al. 1999, IAU Circ., 7294

Li, W. D., et al. 2000, in Cosmic Explosions, ed. S. S. Holt & W. W. Zhang, (New York: AIP), p. 103

Lundqvist, P., & Fransson, C., 1991, ApJ, 380, 575

Maeda, K., Nakamura, T., Nomoto, K., Mazzali, P. A., Patat, F., & Hachisu, I. 2002, ApJ, 565, 405

Matzner, C. D., & McKee, C. F. 1999, ApJ, 510, 379

Mewe, R., Gronenschild, E. H. B. M., & van den Oord, G. H. J. 1985, A&AS, 62 197

Miller, J. S., & Stone, R. P. S. 1993, Lick Obs. Tech. Rep. 66

Oke, J. B., Cohen, J. G., Carr, M., Cromer, J., Dingizian, A., Harris, F. H., Labrecque, S., Lucinio, R., Schaal, W., Epps, H., & Miller, J. 1995, PASP, 107, 375

Panagia, N., Vettolani, G., Boksenberg, A., Ciatti, F., Ortolani, S., Rafanelli, P., Rosino, L., Gordon, C., Reimers, D., Hempe, K., Benvenuti, P., Clavel, J., Heck, A., Penston, M. V., Macchetto, F., Stickland, D. J., Bergeron, J., Tarenghi, M., Marano, B., Palumbo, G. G. C., Parmar, A. N., Pollard, G. S. W., Sanford, P. W., Sargent, W. L. W., Sramek, R. A., Weiler, K. W., & Matzik, P. 1980, MNRAS 192, 861

Patat, F., Barbon, R., Cappellaro, E., & Turatto, M. 1994, A&A, 282, 731

Pian, E., Amati, L, Antonelli, L., Butler, R, Costa, E., Cusumano, G., Danziger, J., Feroci, M., Fiore, F., Frontera, F., Giommi, P., Masetti, N., Muller, J., Oosterbroek, T., Owens, A., Palazzi, E., Piro, L., Castro-Tirado, A., Coletta, A., dal Fiume, D., del Sordo, S., Heise, J., Nicastro, L., Orlandini, M., Parmar, A., Soffitta, P., Torroni, V., in't Zand, J. 1999, A&AS, 138, 399

Pian, E, et al. 2000, ApJ, 536, 778

Predehl, P., & Schmitt, J. H. M. M. 1995, A&A, 293, 889

Schlegel, E. M. 2001, ApJ, 556, L25

Shigeyama, T., & Nomoto, K. 1990, ApJ, 360, 242

Smartt, S. J., Gilmore, G., F., Tout, C. A., & Hodgkin, S. T. 2002, ApJ, 565, 1089

Sohn, Y.-J., & Davidge, T. J. 1998, AJ, 115, 130

Thielemann, F.-K., Nomoto, K., & Hashimoto, M. 1996, ApJ, 460, 468

Wang, L., Howell, D. A., Höflich, P., & Wheeler, J. C. 2001, ApJ, in press

Weiler, K. W., Sramek, R. A., Panagia, N., van der Hulst, J. M., & Salvati, M. 1986, ApJ, 301, 790

Weiler, K. W., Van Dyk, S. D., Panagia, N., & Sramek, R. A. 1992, ApJ, 398, 248

Wheeler, J. C., Yi, I., Höflich, P., & Wang, L. 2000, ApJ, 537, 810

Chapter 7

Supernova 1998S

This chapter is based on the original paper:

> "X-ray, Optical, and Radio Observations of the Type II Supernovae 1999em and 1998S," Pooley, D., Lewin, W. H. G., Fox, D. W., Miller, J. M., Lacey, C. K., Van Dyk, S. D., Weiler, K. W., Sramek, R. A., Filippenko, A. V., Leonard, D. C., Immler, S., Chevalier, R. A., Fabian, A. C., Fransson, C., & Nomoto, K., 2002, *The Astrophysical Journal*, Vol. 572, p. 932,

with the permission of the publisher, *The Astrophysical Journal*.

7.1 Abstract

Observations of the Type IIn (narrow emission line) Supernova (SN) 1998S have enabled estimation of the profile of the SN ejecta, the structure of the circumstellar medium (CSM) established by the pre-SN stellar wind, and the nature of the shock interaction. SN 1998S, at an age of >3 years, is still bright in X-rays and is increasing in flux density at cm radio wavelengths. Spectral fits to the *Chandra* data show that many heavy elements (Ne, Al, Si, S, Ar, and Fe) are overabundant with respect to solar values. We compare the observed elemental abundances and abundance ratios to theoretical calculations and find that our data are consistent with a progenitor mass of approximately 15–20 $M_\odot$ if the heavy element ejecta are radially mixed out

to a high velocity. If the X-ray emission is from the reverse shock wave region, the supernova density profile must be moderately flat at a velocity $\sim 10^4$ km s^{-1}, the shock front is non-radiative at the time of the observations, and the mass-loss rate is 1–2$\times 10^{-4}$ M$_\odot$ yr^{-1} for a pre-supernova wind velocity of 10 km s^{-1}. This result is also supported by modeling of the radio emission which implies that SN 1998S is surrounded by a clumpy or filamentary CSM established by a high mass-loss rate, $\sim 2 \times 10^{-4}$ M$_\odot$ yr^{-1}, from the pre-supernova star.

7.2 Introduction

On 1998 March 3, SN 1998S was optically discovered 16″ west and 46″ south of the nucleus of NGC 3877 (Li et al., 1998). Its spectrum quickly revealed it to be a peculiar Type IIn, with narrow H and He emission lines superimposed on a blue continuum (Filippenko & Moran, 1998) along with strong N III, C II, C III, and C IV emission (Garnavich, Jha, & Kirshner, 1998a; Liu et al., 2000) similar to the "Wolf-Rayet" features seen in the early observations of SN 1983K (Niemela, Ruiz, & Phillips, 1985). SN 1998S reached a peak brightness of $m_V \approx 12$ (Granslo et al., 1998; Garnavich et al., 1998b). For a distance of 17 Mpc (Tully, 1988), the intrinsic brightness of $M_V \approx -18.8$ marks SN 1998S as one of the optically brightest Type II SNe (cf. Patat et al., 1993).

7.3 Observations

7.3.1 X-ray

Our criterion for *Chandra* observations of SNe beyond 10 Mpc was the detection of radio emission greater than 1 mJy at 6 cm. SN 1998S met this criterion on 1999 October 28 (Van Dyk et al., 1999), and subsequent reanalysis of early radio observations indicated very weak detection at 8.46 GHz as early as 1999 January 07 (Lacey et al., 2002). We observed with *Chandra* on 2000 January 10, March 7, August 1, 2001 January 14, and October 17 (days 678, 735, 882, 1048, and 1324 since optical

discovery). Similar to the observations of SN 1999em, these data were taken with the ACIS-S3 chip at nominal frame time (3.2 sec) in TE mode and telemetered in F mode. A summary of the observations is listed in Table 7.1.

7.3.2 Radio

We observed SN 1998S over 20 times with the VLA at frequencies ranging from 22.48 GHz to 1.46 GHz and ages from 89 to 1059 days after the discovery date of 1998 March 03 (Lacey et al., 2002). All observations yielded only upper limits until 1999 January 07, age 310 days, when a weak detection was obtained. Since that time, monitoring has continued and SN 1998S has increased in flux density at all mid-cm wavelengths.

7.3.3 Optical

On 1998 March 7, just 5 days after the discovery of SN 1998S, optical spectropolarimetry was obtained of the supernova with LRISp on the Keck-II 10-m telescope (Leonard et al., 2001a). Total flux spectra were obtained over the first 494 days after discovery, as follows: (a) at Keck using LRIS on 1998 March 5, 6, and 27, and on 1999 January 6, and (b) at the Lick 3-m Shane reflector using the Kast double spectrograph on 1998 June 18, July 17 and 23, and November 25, and on 1999 January 10, March 12, and July 7. See Leonard et al. (2000) for details of the optical observations and reductions.

7.4 *Chandra* Data Reduction

The data for SN 1998S were reduced in exactly the same manner as for SN 1999em (see Sect. 6.4). The second and fifth observations of SN 1998S contained background flares, lasting $\sim$300 sec and $\sim$14 ksec, respectively. The event lists were filtered to exclude the time intervals during which flares occurred. Effective observation times after filtering are listed in Table 7.1.

Table 7.1: *Chandra* Observations of SN 1998S.

Date	Day (From Ref.)	Length (ksec)	Length After Filtering (ksec)	Count Rate (cts ksec^{-1})
2000 Jan 10	678	18.9	18.9	34.4
2000 Mar 7	735	23.4	23.1	30.3
2000 Aug 1	882	19.8	19.8	25.8
2001 Jan 14	1048	29.2	29.2	19.5
2001 Oct 17	1324	28.7	14.8	12.4

7.5 Results

7.5.1 X-ray

The source was detected on all occasions, and an overlay of the X-ray contours from the first observation on an optical image of the host galaxy is shown in Fig. 7-1. The *wavdetect* position[1] (based solely on the *Chandra* aspect solution) is $11^{h}46^{m}06\overset{s}{.}14$, $47°28'55\overset{''}{.}1$ (J2000), which is within $0\overset{''}{.}5$ of the radio and optical positions. In addition to constructing multicolour X-ray lightcurves (Fig. 7-4), the high luminosity of SN 1998S ($L_{\rm x} \approx 10^{40}$ ergs s^{-1}) allowed for basic spectral fitting to be done for each of the first four observations; in the fifth, there were too few counts for a similar type of analysis. We performed this in XSPEC with the VMEKAL model, which is identical to the MEKAL model but allows individual elemental abundances to vary. Using the reddening $E_{(B-V)} = 0.23$ (Leonard et al., 2000), we calculated the hydrogen column density to be $N_{\rm H} = 1.36 \times 10^{21}$ cm^{-2} (Predehl & Schmitt, 1995). We used a redshift of $z = 0.003$ (Willick et al., 1997).

Although there were sufficient counts (>500 per observation) in each of the first four observations for spectral modeling, there were few counts per energy channel. To mitigate the problems associated with fitting such data, we grouped the data to contain a minimum number of counts per bin. Because there were virtually no counts above $\sim$ 7 keV in any of the observations, we would "smear" the Fe line at 6.7 keV if we required more than $\sim$ 7 counts per bin. Therefore, we set the minimum number of counts per bin to the highest possible value which would still retain the integrity

[1]This is the average position of all observations. The standard deviations about the means were $\sigma_{\rm RA} = 0\overset{''}{.}03$ and $\sigma_{\rm Dec} = 0\overset{''}{.}17$.

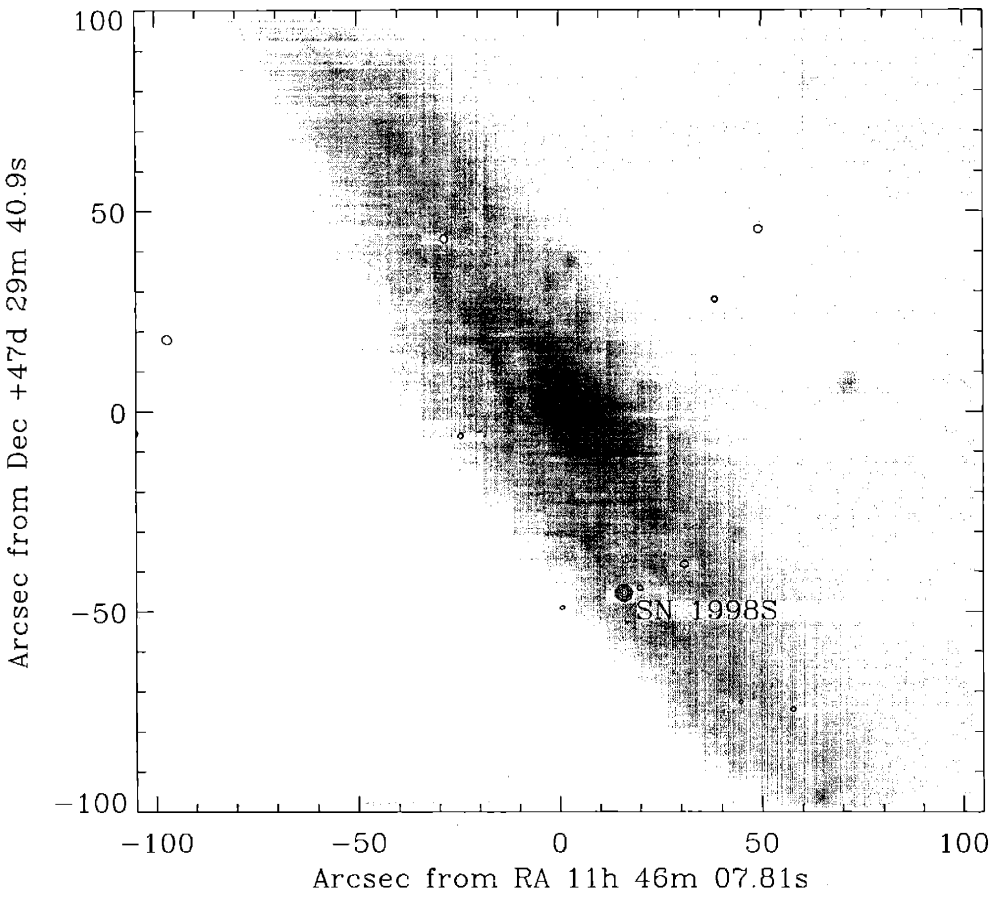

Figure 7-1: NGC 3877 in optical and X-rays. X-ray contours from the first *Chandra* observation of SN 1998S are overlaid on a DSS image of the host galaxy.

of the Fe line. This turned out to be 5 counts per bin for the first observation, 7 for the second, 5 for the third, and 7 for the fourth.

To reduce the number of free parameters in our fits, we froze the abundance of He to its solar value. We also linked the abundances of N, Na, Al, Ar, and Ca to vary with C. The remaining elemental abundances (O, Ne, Mg, Si, S, Fe, and Ni) were allowed to vary independently. We first allowed the column density to vary in our fits. Since the best-fit results were all consistent with the $N_{\rm H}$ obtained from the optical reddening, we fixed this parameter at the calculated value.

We then performed χ^2 fitting using Gehrels weighting for the statistical error (Gehrels, 1986), which is appropriate for low count data. We also performed maximum likelihood fits to the unbinned data using Cash statistics (Cash, 1979). The maximum likelihood fits were in good agreement with the χ^2 fits, and we report the χ^2 results

Table 7.2: VMEKAL Fits to the Spectra of SN 1998S.

Day (From Ref.)	kT (keV)	Fe Abund. (w.r.t. solar)	χ^2/d.o.f.	L_x[2–10 keV][a] (ergs s^{-1})
678	$10.4^{+81.9}_{-2.2}$	$6.5^{+63}_{-6.5}$	82.7/96	9.3×10^{39}
735	$9.6^{+5.5}_{-2.2}$	$4.2^{+7.3}_{-2.6}$	71.7/71	8.8×10^{39}
882	$10.4^{+14.1}_{-4.2}$	$2.8^{+15.8}_{-2.8}$	65.8/75	6.1×10^{39}
1048	$8.0^{+3.7}_{-2.1}$	$5.4^{+14.5}_{-3.5}$	57.0/59	5.3×10^{39}

Listed uncertainties are 90% confidence intervals.

[a]for $z = 0.003$ and $H_0 = 50$

in Table 7.2. We note, however, that fitting with so few counts per bin may give misleading χ^2 values. For ease of viewing, we have plotted the best fit models against evenly binned data (Fig. 7-2).

In order to bring out the line features, we have summed the individual spectra. We feel justified in doing this because the best-fit model parameters from the four individual observations with enough counts for individual modeling are consistent with each other, indicating that the spectral shape is not changing much, only the overall normalization (luminosity). We grouped the summed spectrum to $\geq$15 counts per bin for spectral fitting. Grouping to more counts per bin than that would have washed out some of the weaker line features. The individual response functions for each observations were combined in a weighted average based on exposure times.

We fit four models to this summed spectrum: a single MEKAL plasma with solar abundances (1-T MEKAL); two MEKAL plasmas with solar abundances (2-T MEKAL); a single MEKAL plasma with variable abundances (all elements allowed to vary except He; 1-T VMEKAL); and a single MEKAL with solar abundances plus a single MEKAL with variable abundances (2-T VMEKAL). The 1-T MEKAL model did not fit the data well, with a χ^2 of 181 for 124 degrees of freedom (dof). Tests of the other three model fits against this one using the F-statistic indicate that only the 1-T VMEKAL fit was a significant improvement (required at the 3.8 σ level). Most of the abundances in this model are not well constrained (especially those of C, N, Na, and Ni). The uncertainty in each abundance was determined in the following way. The abundance was changed from the best-fit value, the model was refit (with all other parameters allowed to vary), and the resultant χ^2 was compared to the best-

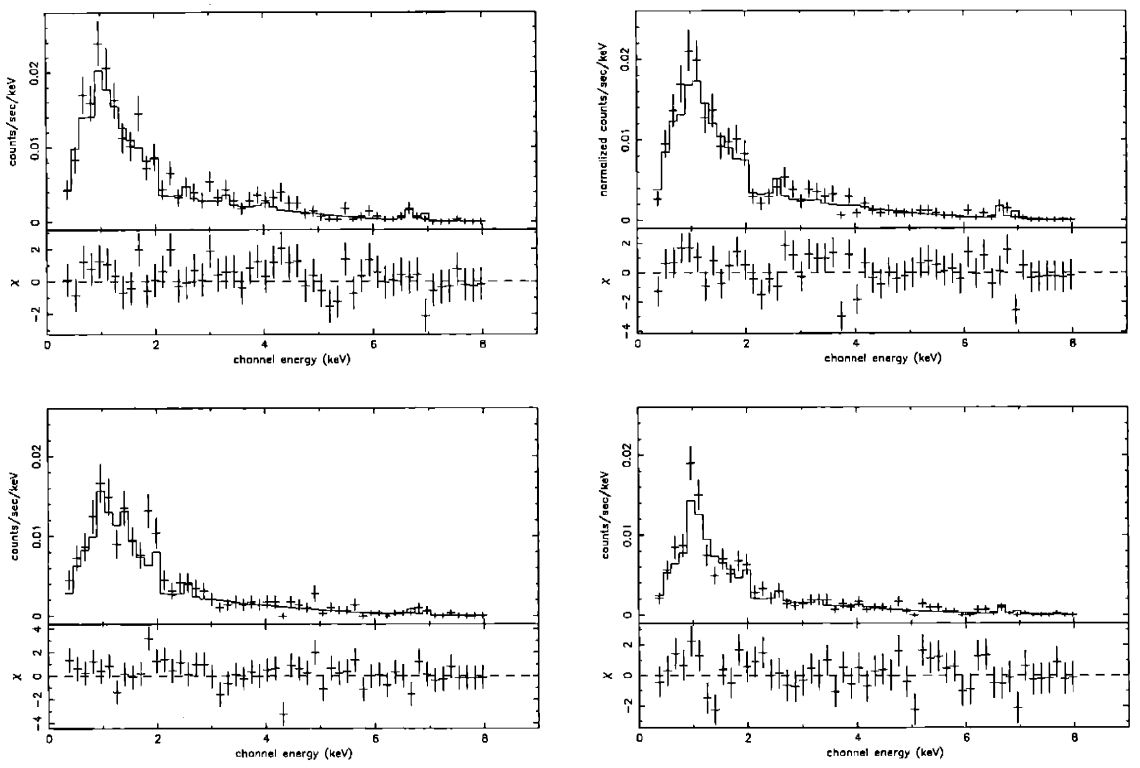

Figure 7-2: Spectra of SN 1998S. The first observation is in the upper left, the second in the lower left, the third in the upper right, and the fourth in the lower right. Best-fit VMEKAL models are overplotted on evenly binned data.

fit χ^2. This was repeated until the difference in χ^2 was 2.706, which gave the 90% confidence interval for the given parameter. Table 7.3 lists the results. The best-fit temperature was $kT = 9.8^{+2.2}_{-1.8}$ keV, and the fit statistic was $\chi^2 = 139$ for 116 degrees of freedom. Fig. 7-3 shows the summed spectrum and best-fit VMEKAL model with labels indicating the rough positions of elemental lines.

7.5.2 Radio

Since its initial radio detection at 8.46 GHz on 1999 January 07 (310 days after optical discovery), SN 1998S has increased at all mid-cm wavelengths. Modeling indicates that it should reach its 6 cm flux density peak at age ~1000 days, at roughly the epoch of the most recent observations on 2001 January 25. Assuming that is the case, SN 1998S is behaving like other radio-detected Type IIn (SNe 1986J and 1988Z both peaked at 6 cm wavelength at age ~1000 days) although it will be the least radio luminous at 6 cm peak ($L_{6\mathrm{cm\ peak}} \sim 3.6 \times 10^{26}$ erg s^{-1} Hz^{-1}) of the six Type IIn RSNe

Table 7.3: Elemental Abundances from VMEKAL Fit to Summed Spectrum of SN 1998S.

Element	Best-fit Abund.	90% Confidence Interval
O	0.7	0–2.9
Ne	15	8.7–35
Mg	0	0–1.6
Al	33	0–135
Si	5.7	2.4–15
S	8.7	3.0–24
Ar	18	3.4–52
Ca	0.8	0–13
Fe	3.0	1.8–6.8
C	1.0	0–200
N	0	0–18
Na	0	0–36
Ni	0	0–14

These abundances are actually the ratio of a given element to H normalized to the similar solar ratio. For example, "Ne" is actually $[(\mathrm{Ne/H})_{98S}]/[(\mathrm{Ne/H})_{\odot}]$.

known (SNe 1978K, 1986J, 1988Z, 1995N, 1997eg, and 1998S). The radio data are shown together with the X-ray results in Fig. 7-4.

Under the Chevalier model of a dense CSM established by a slow pre-supernova stellar wind ($v_w = 10$ km s^{-1}, $v_{\rm shock} = 10^4$ km s^{-1}, $T = 2 \times 10^4$ K; see, e.g., Weiler et al. 1986), such a radio luminosity is interpreted as indicative of a mass-loss rate of $\sim 2{\times}10^{-4}$ M$_\odot$ yr^{-1}. The radio position of the emission from SN 1998S is $11^{\rm h}46^{\rm m}6\overset{\rm s}{.}140$, $47°28'55\overset{''}{.}45$. The details of the observations and analysis will be found in Lacey et al. (2002). It should be noted that the best fit to the radio data requires significant clumping or filamentation in the CSM, as was also found for the Type IIn SNe 1986J and 1988Z (Weiler et al., 1990; Van Dyk et al., 1993).

7.5.3 Optical

SN 1998S exhibits a high degree of linear polarization, implying significant asphericity for its continuum-scattering environment (Leonard et al., 2000). Prior to removal of the interstellar polarization, the polarization spectrum is characterized by a flat continuum (at $p \approx 2\%$) with distinct changes in polarization associated with both the broad (symmetric, half width near zero intensity $\gtrsim 10,000$ km s^{-1}) and narrow

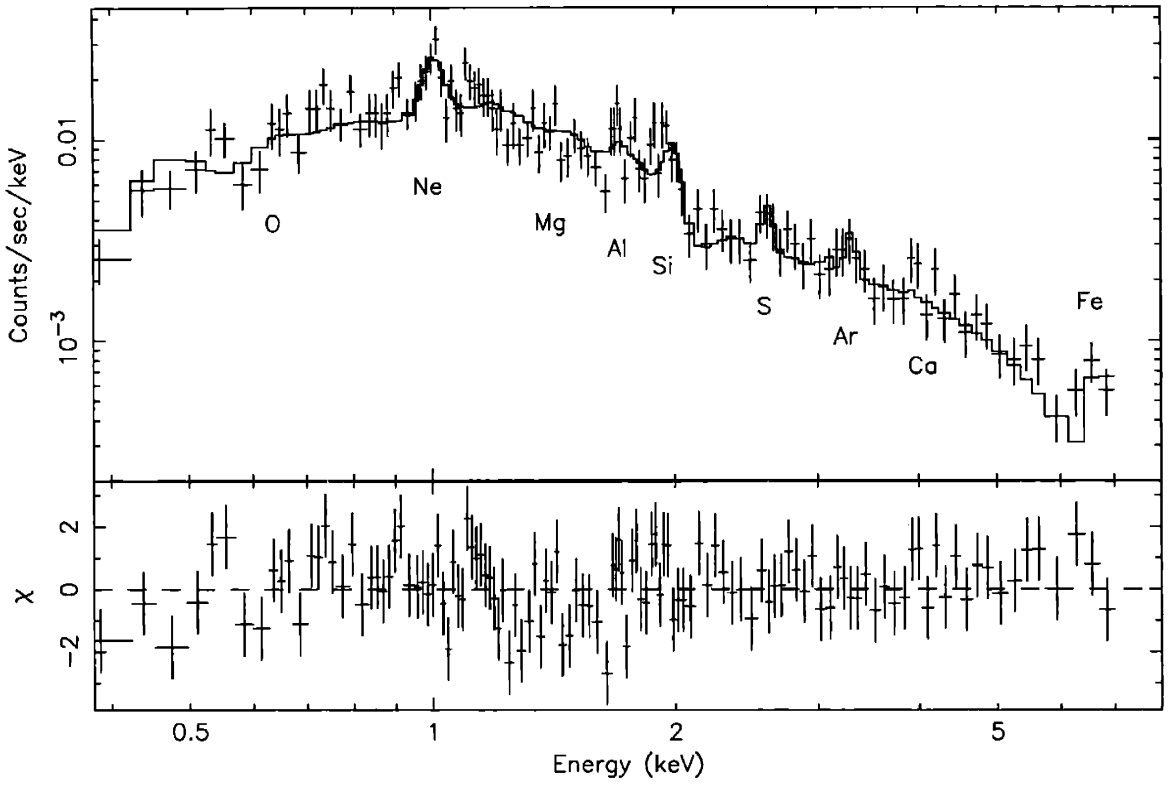

Figure 7-3: VMEKAL fit to the summed spectrum of SN 1998S. Labels indicate approximately where emission lines for each element would be observed.

(unresolved, full width at half maximum < 300 km s^{-1}) line emission seen in the total flux spectrum. When analyzed in terms of a polarized continuum with unpolarized broad-line recombination emission, an intrinsic continuum polarization of $p \approx 3\%$ results, suggesting a global asphericity of $\gtrsim 45\%$ from the oblate, electron-scattering dominated models of Höflich (1991). The smooth, blue continuum evident at early times is inconsistent with a reddened, single-temperature blackbody, instead having a color temperature that increases with decreasing wavelength. Broad emission-line profiles with distinct blue and red peaks are seen in the total flux spectra at later times, suggesting a disk-like or ring-like morphology for the dense ($n_e \approx 10^7$ cm^{-3}) circumstellar medium, generically similar to what is seen directly in SN 1987A, although much denser and closer to the progenitor in SN 1998S. Such a disk/ring-like circumstellar medium may have formed from a merging of a binary-companion star that ejects the common-envelope material in the direction of the orbital plane of the binary system (Nomoto, Iwamoto, & Suzuki, 1995).

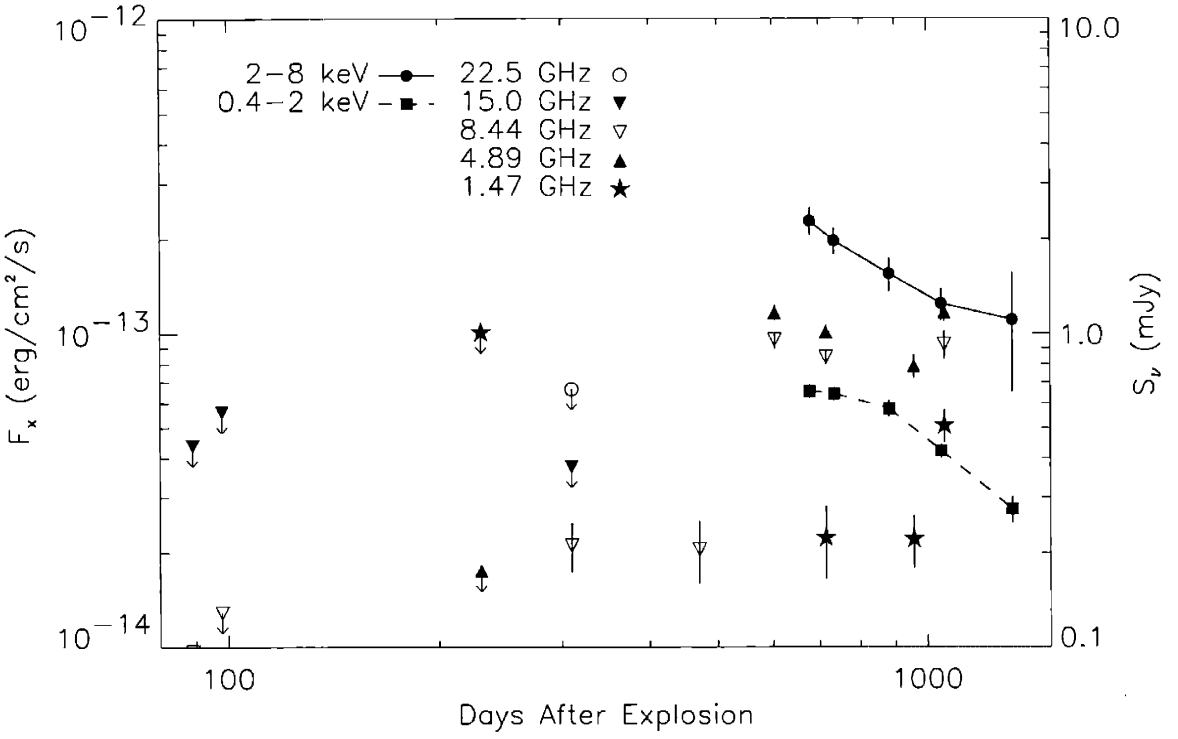

Figure 7-4: X-ray and radio light curves of SN 1998S. The detections are shown with error bars while the upper limits are shown with downward arrows. The absorbed X-ray flux declines in both the hard (*solid lines*) and soft (*dashed lines*) bands.

7.6 Discussion

7.6.1 The Individual Observations

The high X-ray luminosity of SN 1998S places it in the same class as the X-ray bright Type IIn SNe 1978K, 1986J, 1988Z, and 1995N. Fox et al. (2000) discussed X-ray observations of SN 1995N and summarized the results on the other SNe. SN 1995N had an X-ray luminosity of 1.5×10^{41} ergs s^{-1} at an age of 2.0 years. SN 1998S is at the low end of the X-ray luminosities spanned by these sources

The optical emission from SN 1998S shows both narrow and broad lines that can be attributed to circumstellar interaction (Fassia et al., 2000; Leonard et al., 2000; Chugai, 2001). The narrow lines are presumably from dense circumstellar gas that is heated and ionized by the supernova radiation. Although high velocities ($V_4 \approx 1$) are observed in the early evolution of SN 1998S, by day 494 the maximum observed velocities were $V_4 = 0.5 - 0.6$ (Leonard et al., 2000). These velocities are much higher

than the estimated velocity of gas at the photosphere, indicating that the emission is from circumstellar interaction.

The interpretation of the X-ray emission from Type IIn supernovae is not straightforward because of the possibility that the emission is from shocked circumstellar clumps (see, e.g., Weiler et al. 1990 and Chugai 1993 on SN 1986J and Van Dyk et al. 1993 on SN 1988Z). The radio results for SN 1998S indicate that the CSM is likely clumpy or filamentary (Lacey et al., 2002). However, if our finding of heavy element overabundances is correct, the X-ray emission is expected to be from shocked SN ejecta. If the interaction can be approximately described by smooth ejecta running into a smooth circumstellar wind, the temperature behind the reverse shock front is $T_{\rm rev} = 2.4 V_4^2$ keV ($n = 9$), $5.4 V_4^2$ keV ($n = 7$), or $9.6 V_4^2$ keV ($n = 6$). It is difficult to produce the high observed temperature ($T \approx 10$ keV) unless there is unseen high velocity gas and the ejecta density profile is relatively flat. The observations do not show the cooling that is expected as the shock interaction region decelerates, but the range in time is not large enough for the effect to be clearly visible.

The X-ray luminosity shows a clear decline with time, approximately $\propto t^{-1.3}$. This is in reasonable agreement with what is expected for free-free emission from a non-radiative shock region (t^{-1} dependence as discussed above), so we can again use eq. (2) to estimate the mass-loss rate. The result is $\dot{M}_{-4}/v_{w1} = (1-2)$, where $\dot{M}_{-4} = \dot{M}/10^{-4}$ M$_\odot$ yr^{-1}, if $n = 6$ and $V_4 = 1$ (these estimates are implied by the high observed temperature of $\sim$10 keV) on day 665, again comparable to that determined from radio modeling of $\dot{M}_{-4}/v_{w1} \sim 2$. A high mass-loss rate is required to produce the X-ray luminosity, but the cooling time is still longer than the age. The assumption of a non-radiative reverse shock region is justified. In this model, the X-ray luminosity of the forward shock region is comparable to that from the reverse shock. However, the higher temperature of the forward shock region implies that the reverse shock dominates the emission in the energy band that we observed.

The radio luminosity of SN 1998S is low for a RSN with a late turn-on time (see Fig. 6-3). This implies that synchrotron self-absorption was not important for the early absorption. This accounts for the basic features of the X-ray emission. The flat

supernova density profile implies that much of the supernova energy is in high velocity ejecta. A similar deduction was made by Chugai & Danziger (1994) for SN 1988Z. The heavy element overabundances require that these elements be mixed out to a high velocity in the ejecta, which has been shown to occur in Cas A (Hughes et al., 2000). In theoretical models of aspherical explosions, heavy-element-rich matter is naturally ejected at high velocities, which well explains the peculiar late spectral features of SN 1998bw (Maeda et al., 2002). The polarization and spectral line profiles observed in SN 1998S (Leonard et al., 2000) show that the explosion was complex, i.e. that the spherically symmetric model described here must be an oversimplification.

7.6.2 The Summed Spectrum

We turn now to the observed elemental abundance ratios in the summed *Chandra* spectrum (Table 7.3), which are enhanced by a factor of $\sim$ 3 - 30 over solar. These heavy elements must have been synthesized in the core evolution and explosion.

In core-collapse supernovae, a strong shock wave forms and propagates outward through the star (e.g., Shigeyama & Nomoto 1990). Behind the shock, materials are explosively burned into heavy elements and accelerated to $\sim$5000 km s^{-1}. At the composition interface, the expanding materials are decelerated by the collision with the outer layers, which induces the Rayleigh-Taylor instability (e.g., Ebisuzaki, Nomoto, & Nomoto 1988; Arnett et al. 1989). Heavy elements are then mixed into outer layers. Such a mixing induced at the Si/O, C/He, and He/H interfaces brings Fe-peak elements, as well as Si, Mg, Ne, O, and C, into the H-rich envelope. These heavy elements in many Rayleigh-Taylor fingers are rather well-mixed through the interaction between the fingers (e.g., Hachisu et al. 1992). We thus assume that, although the heavy elements mixed into the H-rich envelope consists of only a fraction of the core materials, the abundance ratios among the mixed heavy elements are the same as in the integrated core materials. The mixing associated with the Rayleigh-Taylor instabilities continues until the shock wave reaches the surface and the expansion becomes homologous.

When the ejecta collides with the circumstellar matter, forward and reverse shock

waves form and the latter propagates back into the H-rich envelope. The mass of the reverse-shocked H-rich envelope $\delta M_{\rm H}$ at the time of the observations depends on the strength of the circumstellar interaction and the density structure of the H-rich envelope (e.g., Chevalier & Fransson 1994; Suzuki & Nomoto 1995). We denote by $\delta M_{\rm Z}$ the mass of heavy elements mixed into the reverse-shocked H-rich envelope. The observed mass fraction of heavy elements is then $\delta M_{\rm Z}/X\delta M_{\rm H}$, where X denotes the H mass fraction.

We briefly summarize here the three types of heavy elements ejected from core-collapse SNe (e.g., Thielemann, Nomoto, & Hashimoto 1996):

O, Ne, and Mg: These elements are synthesized mostly before collapse during core- and shell-C burning; some Ne is processed into Mg and O during Ne burning. In the explosion, these elements are partially produced by explosive C burning, Ne is partially burned into Mg and Si, and O and Mg are partially burned into Si. The masses of these elements are sensitive to the progenitor mass, M, increasing with M. However, the degree of dependence on M varies across elements. For example, the Ne/Mg ratio depends on the conditions of C and Ne burning, thus depending on M.

Si, S, and Ar: These elements are produced by explosive O burning during the explosion. Their masses do not much depend on M since the pre-collapse core structure is not very sensitive to M.

Fe: The mass of ejected Fe is very sensitive to the mass cut that divides the compact remnant and the ejecta, or the amount of fall-back matter. Theoretically, it is not possible to make a good estimate of the Fe mass because of the uncertainties in the explosion mechanism.

In our comparisons, we use Si for normalization because it is the least dependent on M. We do not use Fe for comparison because of the large theoretical uncertainties. We now compare the O/Si, Ne/Si, and Mg/Si ratios (relative to the solar abundance ratios) with the theoretical calculations of Nomoto et al. (1997). These models are summarized in Table 7.4.

Table 7.4: Elemental Abundance Ratios Relative to Solar for SN 1998S and Theoretical Models.

Abund. ratio	SN 1998S	13 $M_\odot$	15 $M_\odot$	18 $M_\odot$	20 $M_\odot$	25 $M_\odot$	40 $M_\odot$
Ne/Si	0.6–14	0.14	0.17	0.86	1.1	2.2	0.56
Mg/Si	0–0.7	0.18	0.49	0.58	1.09	2.1	1.1
O/Si	0–1.2	0.20	0.43	0.80	1.4	2.4	1.6

The observed O/Si value of 0–1.2 seems to indicate that the mass of the progenitor was $\lesssim$20 $M_\odot$. The Mg/Si value of 0–0.7 also points to a progenitor mass of $<$20 $M_\odot$. The observed Ne/Si ratio of 0.6–14 excludes progenitor masses of $\lesssim$15 $M_\odot$. According to these models, the mass of the proginitor must have been between 15 $M_\odot$ and 20 $M_\odot$.

We note that the supernova yields are determined by the helium core mass $M_{\rm He}$ of the progenitor rather than the zero-age main-sequence mass M. Thus the Mg/Si and Ne/Si results actually provide the constraint $M_{\rm He} = 5 \pm 1$ $M_\odot$ (Nomoto et al., 1997). The M-$M_{\rm He}$ relation depends on the mass loss. If we adopt the spiral-in binary scenario for the origin of Type IIn SN (Nomoto, Iwamoto, & Suzuki, 1995), a large amount of mass-loss in the early phase of the progenitor's expansion leads to a smaller $M_{\rm He}$ compared with the case of no mass loss. In this case, the progenitor of SN 1998S could be initially more massive.

Bibliography

Cash, W. 1979, ApJ, 228, 939

Chugai, N. N. 1993, ApJ, 414, L101

Chugai, N. N. 2001, MNRAS, 326, 1448

Chugai, N. N., & Danziger, I. J. 1994, MNRAS, 268, 173

Fassia, A., Meikle, W. P. S., Vacca, W. D., Kemp, S. N., Walton, N. A., Pollacco, D. L., Smartt, S., Oscoz, A., Aragón-Salamanca, A., Bennett, S., Hawarden, T. G., Alonso, A., Alcalde, D., Pedrosa, A., Telting, J., Arevalo, M. J., Deeg, H. J., Garzón, F., Gómez-Roldán, A., Gómez, G., Gutiérrez, C., López, S., Rozas, M., Serra-Ricart, M., & Zapatero-Osorio, M. R. 2000, MNRAS, 318, 1093

Filippenko, A. V., & Moran, E. C. 1998, IAU Circ., 6830

Fox, D. W., Lewin, W. H. G., Fabian, A., Iwasawa, K., Terlevich, R., Zimmermann, H. U., Aschenbach, B., Weiler, K., Van Dyk, S., Chevalier, R., Rutledge, R., Inoue, H., & Uno, S. 2000, MNRAS, 319, 1154

Garnavich, P., Jha, S., & Kirshner, R. 1998a, IAU Circ., 6832

Garnavich, P., Kirshner, R., Challis, P., Koranyi, D., & Culkins, M. 1998b, IAU Circ., 6845

Gehrels, N. 1986, ApJ, 303, 336

Granslo, B. H., Shanklin, J., Carvajal, J., & Hornoch, K. 1998, IAU Circ., 6846

Höflich, P. 1991, A&A, 246, 418

Hughes, J. P., Rakowski, C. E., Burrows, D. N., & Slane, P. O. 2000, ApJ, 528, L109

Lacey, C. K., Weiler, K. W., Van Dyk, S. D., Panagia, N., & Sramek, R. A. 2002, in preparation

Leonard, D. C., Filippenko, A. V., Barth, A. J., & Matheson, T. 2000, ApJ, 536, 239

Leonard, D. C., Filippenko, A. V., Ardila, D. R., & Brotherton, M. S. 2001a, ApJ, 553, 861

Li, W.-D., Li, C., Filippenko, A. V., & Moran, E. C. 1998, IAU Circ. 6829

Liu, Q.-Z., Hu, J.-Y., Hang, H.-R., Qiu, Y.-L., Zhu, Z.-X., & Qiao, Q.-Y. 2000, A&AS, 144, 219

Maeda, K., Nakamura, T., Nomoto, K., Mazzali, P. A., Patat, F., & Hachisu, I. 2002, ApJ, 565, 405

Niemela, V. S., Ruiz, M. T., & Phillips, M. M. 1985, ApJ, 289, 52

Nomoto, K., Iwamoto, K., & Suzuki, T. 1995, Phys. Rep., 256, 173

Nomoto, K., Hashimoto, M., Tsujimoto, T., Thielemann, F.-K., Kishimoto, N., Kubo, Y., & Nakasato, N. 1997, Nucl. Phys. A, 616, 79

Patat, F., Barbon, R., Cappellaro, E., & Turatto, M. 1993, A&A, 98, 443

Predehl, P., & Schmitt, J. H. M. M. 1995, A&A, 293, 889

Tully, R. B. 1988, *Nearby Galaxies Catalog*, Cambridge University Press

Van Dyk, S. D., Weiler, K. W., Sramek, R. A., & Panagia, N. 1993, ApJ, 419, L69

Van Dyk, S. D., Lacey, C. K., Sramek, R. A., & Weiler, K. W. 1999, IAU Circ., 7322

Weiler, K. W., Sramek, R. A., Panagia, N., van der Hulst, J. M., & Salvati, M. 1986, ApJ, 301, 790

Weiler, K. W., Panagia, N., & Sramek, R. A. 1990, ApJ, 364, 611

Willick, J. A., Courteau, S., Faber, S. M., Burstein, D., Dekel, A., & Strauss, M. A. 1997, ApJ, 109, 333

Chapter 8

Conclusions

8.1 The Impact of This Work

Observations at radio, optical, and X-ray wavelengths have allowed the estimation of the physical parameters of two quite different Type II SN examples, Type II-P SN 1999em and Type IIn SN 1998S. From these results, it is possible to study, over a broad wavelength range, the physical parameters of the explosions and the structure and density of the CSM established by the pre-SN wind. Such results are of importance for estimation of the properties of the pre-SN star and its last stages of evolution before explosion (e.g., Nomoto, Iwamoto, & Suzuki 1995). In addition, the *Chandra* data have revealed the presence of many heavy elements in the spectrum of SN 1998S, which is the first time this has been seen in the X-ray spectrum of a young SN. We have shown the kind of analysis that can be done by comparing the observed X-ray determined abundance ratios to the model predictions, and we were able to show that the mass of the progenitor was $\sim$15–20 $M_{\odot}$. We do caution, however, that our model assumptions on mixing are approximate and that there are uncertainties in both the interpretation of the X-ray data and the model calculations. However, we have shown the promise of this type of analysis, and, as both the observational and theoretical sides mature, this could become an extremely powerful tool.

8.2 Progressing Further

With the detection of a plethora of heavy elements in SN 1998S and Fe in other SNe, e.g., SN 1993J (Kohmura et al., 1994) and SN 1986J (Houck et al., 1998)), we expect several future SNe spectra to also contain line emission. In addition to providing an estimate of the progenitor's mass (via comparison of observed abundance ratios to theoretically calculated ones), emission lines of sufficient strength may allow for a direct test of emission models (neither SN 1999em's nor SN 1998S's spectra contained such lines). According to the Chevalier model (Chevalier & Fransson, 1994), the X-ray line emission arises from the reverse shock region and would thus have a Doppler-broadened width of $\sim$10,000 km s^{-1}. According to an alternative model of Chugai (1993), the soft X-ray emission and any corresponding X-ray emission lines emanate from small collapsing clumps of the stellar wind, giving them a width of $\lesssim$1000 km s^{-1}. Measurements of a line width with roughly this precision should allow us to distinguish between the two models. These measurements are possible with the CCDs aboard the current X-ray telescopes (*Chandra* and *XMM-Newton*). Use of the gratings on these satellites would give much more detailed spectral information, but would require an extremely bright SN or an unjustifiably long exposure to obtain statistically meaningful results.

The Japanese *Astro-E* mission featured an X-ray calorimeter, which offered an unprecedented spectral resolution of $\Delta E = 10$ eV across the entire 0.4–10 keV range. We had an approved proposal to observe a nearby (within 10 Mpc) SN for 100 ksec, but, unfortunately, the mission was lost during launch on 2000 Feb 10. However, the Japanese Institute of Space and Astronautical Science is planning to launch an identical satellite, *Astro-E2*, in early 2005. We hope to again receive time to observe a nearby SN with the X-ray calorimeter. It is not known what the $\Delta E = 10$ eV spectrum of a $\sim$weeks-old SN will look like. However, given that the X-ray emission is thermal and arises in shocked plasmas (perhaps of anomalous abundances) on either side of a radiatively cooled and absorbing region, we can be confident that it will contain interesting features.

However, even without line emission, the X-ray data are vital in determining the nature of the SN ejecta and CSM, which are directly related to the final evolutionary stages of the progenitor stars (Nomoto, Iwamoto, & Suzuki, 1995). With only 17 SNe observed in X-rays to date, we need to continue to build up the sample using *Chandra* and *XMM-Newton*, and ultimately a picture will emerge that will substantially deepen our knowledge. Because of the great diversity of Type II (and related Type Ib/c) SNe, only the multiwavelength study of additional examples can yield a comprehensive understanding of the last stages of massive star evolution.

Bibliography

Chevalier, R. A., & Fransson, C. 1994, ApJ, 420, 268

Chugai, N. N. 1993, ApJ, 414, L101

Houck, J. C., Bregman, J. N., Chevalier, R. A., & Tomisaka, K. 1998, ApJ, 493, 431

Kohmura, Y., Inoue, H., Aoki, T., Ishida, M., Itoh, M., Kotani, T., Tanaka, Y., Ishisaki, Y., Makishima, K., Matsushita, K., Gotthelf, E., Ricker, G., & Tsusaka, Y. 1994, PASJ, 46, L157

Nomoto, K., Iwamoto, K., & Suzuki, T. 1995, Phys. Rep., 256, 173